Doktori értekezés

Magnetic phase and domain evolution of antiferromagnetically coupled multilayers

Major Márton

Eötvös Loránd Tudományegyetem Természettudományi Kar
Fizika Doktori Iskola
Anyagtudomány és szilárdtestfizika program

Témavezető:
Dr. Nagy Dénes Lajos, a fizikai tudomány doktora, egyetemi tanár

Doktori iskola vezetője: Dr. Horváth Zalán
Doktori program vezetője: Dr. Lendvai János

MTA KFKI Részecske és Magfizikai Kutatóintézet

2006.

Contents

List of abbreviations

AF	antiferromagnetic, antiferromagnetically
APD	avalanche photodiode
BB	bilinear-biquadratic (model)
BSF	bulk spin flop
EFFI	environment for fitting
FM	ferromagnetic
FWHM	full width at half maximum
GMR	giant magnetoresistance
MBE	molecular beam epitaxy
ML	multilayer
MOKE	magneto-optic Kerr effect
MR	Mössbauer reflectometry
NRS	nuclear resonant scattering
PDS	position sensitive detector
PIXE	particle induced x-ray emission (spectrometry)
PNR	polarized neutron reflectometry
RBS	Ruhterford backscattering spectrometry
RHEED	reflection high energy electron diffraction
SDW	spin-density wave
SMR	synchrotron Mössbauer reflectometry
SQUID	superconducting quantum interference device
SR	synchrotron radiation
TDSMR	time differential synchrotron Mössbauer reflectometry
TER	total external reflection
TISMR	time integral synchrotron Mössbauer reflectometry
TOF	time of flight
UHV	ultra high vacuum
VSM	vibrating sample magnetometry

Chapter 1

Introduction

Nanotechnology is one of the research priorities of present-day industrial societies. The vast amount of emerging applications of possible miniaturization was predicted by Richard Feynmann already in 1959 in his famous lecture, "There's Plenty of Room at the Bottom". In our days, the potential benefits of nanotechnology in information technology, advanced manufacturing, medicine and health, transportation, environment and energy industry, etc. are enormous.

Giant Magnetoresistance (GMR) [1] is also based on nanotechnology, in particular on thin magnetic films. GMR has made its way to applications [2] like magnetic sensors, spin valves, spin-tunneling junctions and the magnetic random access memory (MRAM). The underlying effect, viz. the antiferromagnetic (AF) coupling of magnetic layers was discovered in 1986 by Grünberg et al [3]. The trilayer consisted of ferromagnetic Fe layers sandwiched by Cr spacers. Despite the fact that AF coupling was found in many multilayer (ML) systems, Fe/Cr MLs certainly belong to the most investigated ones. This is partly due to the still not fully understood coupling behaviour of this system.

Another aspect of the AF-coupled MLs is their domain structure. In contrast to ferromagnetic films and structures in a strongly AF-coupled ML, the stray field of the domains is in large compensated thus other forces may influence the appearance of the domains. This is also obvious from the comparison of the patch-like AF domains to the characteristic ripple domains of ferromagnetic thin films. Formation of patch domains is mainly governed by fluctuations of the AF coupling resulting in a lateral distribution of the saturation field. The seemingly small effect of external field believed to prohibit the manipulation of the AF domains [4]. However, one may wish to control the domain size, a parameter profoundly influencing the noise of magnetoresistive devices.

The phase diagram of AF-coupled MLs with different phenomenological (mainly biquadratic) coupling terms and magnetic anisotropies still holds new phenomena in store to describe. For example, in a very recent article [5] J. Meersschaut et al. reported on experimental evidences

of the hard-axis spin-reorientation transition, a phenomenon also discussed in the present work (2.6). This transition may exist in AF-coupled Fe/Cr MLs with fourfold in-plane anisotropy.

Not too many papers have been published so far on the morphology of AF domains, due to the difficulties in direct visualization of these compensated objects. Therefore indirect methods, first of all those based on photon and neutron scattering, play an indispensable role in studying domains in AF-coupled multilayers. Scattering techniques often deliver valuable information about AF domains. For example, the first experimental evidence of the rapid growth of the AF domains during the bulk spin flop transition was discovered by our group using Synchrotron Mössbauer Reflectometry (SMR) and Polarized Neutron Reflectometry (PNR) [6].

In the first part of this work an introduction is given to the phenomenological models of AF-coupled MLs. The effects of finite stacking, anisotropies and different coupling terms are discussed. Phase diagrams are calculated for MLs with fourfold anisotropy. After the theoretical introduction, the Fe/Cr ML is presented. The structure and the magnetization of the sample are fitted with various experimental techniques. An extended bilinear-biquadratic (BB) model was developed to fit the magnetization loops. The main aim of the work was to coherently describe the phase and domain transitions of the AF-coupled ML. For this purpose a short introduction to the momentum space and the applied methods (SMR and PNR) is given. Two first-approximation theories for domain ripening are also presented. Direct evidence of the bulk spin flop transition is given and, in the final part of this thesis, the domain measurements are discussed.

Acknowledgements

It is almost impossible to thank all people, who helped this work during the past seven years. The author would like first to thank Dénes Lajos Nagy for supervising the PhD work, for pointing out the problems to attack and for the critical review of the manuscript. The author is also grateful to László Bottyán for the inspiring discussions during the PhD period. Thank goes to the colleagues in the institute (László Deák, András Kocsonya, Ferenc Tanczikó and Edit Szilágyi) for measurements and academic discussion. The half-year-long stay at the IKS Leuven, Belgium under the supervision of Johan Meersschaut gave the opportunity to learn thin film growth and characterization techniques. The Fe/Cr sample investigated in this work was also produced in Leuven. Important magnetic characterization was done by László Kiss (SQUID, MTA SZFKI) and by Johan Swerts (MOKE, IKS Leuven) on the above-mentioned sample. We are grateful for the immense help in the ESRF experiments for the members of the Nuclear Resonance Group, in the first place to Rudolf Rüffer and Olaf Leupold. No neutron experiments at JINR Dubna would have been possible without A. V. Petrenko's help. The friendly atmosphere in the Dubna neutron reflectometry group and discussion with Yu. V. Nikitenko also contributed to the success of this work.

This work was partly supported by the European Community under the Specific Tar-

geted Research Project Contract No. NMP4-CT-2003-001516 (DYNASYNC). Support by the Flemish-Hungarian bilateral Project No. BIL98/20 and Projects No. T 029409 and T 047094 of the Hungarian Scientific Research Fund (OTKA) are gratefully acknowledged. The author is thankful to ESRF and JINR for the allocated beam time. Support of the Hungarian Academy of Science trough the HAS-JINR Cooperation Fund for neutron measurements is appreciated. The financial help of the Hungarian Synchrotron Committee is also acknowledged.

Finally the author would like to thank his lowing wife for her infinite patience and would like to dedicate this book, and his future spare time to her and her son.

Chapter 2

Energy terms and phase diagrams

2.1 Introduction

The building block of the described magnetic MLs (Fig. 2.1) is the *layer*, which is infinite in the $x-y$ plane of the sample and a few monolayers thick in the perpendicular z direction. The phenomenological description of the coupled MLs involves 'classical magnetic moments' associated to each magnetic building block. The investigated physical behavior of such a ML is mainly due to the so-called 'spacer layers', which may cause an interlayer coupling between the magnetic layers.

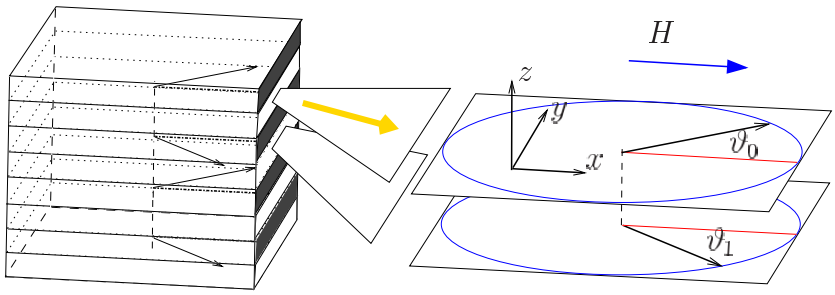

Figure 2.1: Sketch of a ML. The individual layers are a few atoms thick in the z direction, while macroscopic in the $x-y$ plane. On the right the coordinate system of the two-sublattice model (see later) is shown.

The energy of such a model system per surface unit area is [7, 8]:

$$\varrho_E = \sum_{i=0}^{n-2} J_{i,i+1}\widehat{\mathbf{M}}_i\widehat{\mathbf{M}}_{i+1} + \sum_{i=0}^{n-2} B_{i,i+1}\left(\widehat{\mathbf{M}}_i\widehat{\mathbf{M}}_{i+1}\right)^2 + \sum_{i=0}^{n-1} A_i\left(\widehat{\mathbf{M}}_i\right) - \mu_0\mathbf{H}\sum_{i=0}^{n-1}\mathbf{M}_i d_i \qquad (2.1)$$

where the magnetic layers (total of n) are numbered starting with 0, $\mathbf{M}_i$ is the magnetization of the given layer i (the spacer layers being taken into account only by the J coupling constant), $\widehat{\mathbf{M}}_i = \mathbf{M}_i/M_i$, d_i are the layer thicknesses, $J_{i,i+1}$ ($J_{i,i+1} > 0$, $\forall\, i$) are the AF coupling constants,

$B_{i,i+1}$ ($B_{i,i+1} > 0, \forall\, i$) are the biquadratic coupling constants, A_i are the in-plane anisotropy terms being function of the magnetization direction, H is the external field and $\mu_0 = 4\pi \cdot 10^{-7}$ Vs/Am is the permeability of free space. All magnetization vectors are assumed to lie in the plane of the sample (the $x - y$ plane), thus the unit vector $\widehat{\mathbf{M}}_i$ can be written as

$$\widehat{\mathbf{M}}_i = \begin{pmatrix} \cos\vartheta_i \\ \sin\vartheta_i \end{pmatrix} \tag{2.2}$$

where ϑ_i is the angle between the x-axis and the i-th layer magnetization vector.

Equation (2.1) conforms to the SI units. From now on, we will use a slightly modified-SI system in the sense that the quantity $\mu_0\mathbf{H}$ will be called external field, will be denoted by $\mathbf{H}$, but will be nevertheless measured in tesla. Furthermore, except when noted, all calculations will be performed in the lab system[1] and with the external field pointing along the x-axis ($\vartheta_H = 0$). Finally we introduce $\tilde{\mathbf{M}}_i = \mathbf{M}_i d_i$. With the above comments we can write:

$$\varrho_E = \sum_{i=0}^{n-2} J_{i,i+1}\cos\left(\vartheta_{i+1} - \vartheta_i\right) + \sum_{i=0}^{n-2} B_{i,i+1}\cos^2\left(\vartheta_{i+1} - \vartheta_i\right) + \sum_{i=0}^{n-1} A_i\left(\vartheta_i, \vartheta_i^{\mathrm{S}}, \vartheta^{\mathrm{S}}\right) - H\sum_{i=0}^{n-1}\tilde{M}_i\cos\left(\vartheta_i - \vartheta_H\right). \tag{2.3}$$

Note that in the following for shorthand we omit the tilde from $\tilde{M}$, but still mean layer magnetization times layer thickness.[2] The above model function is a 'single domain' approximation, in-plane domain formation and thus hysteresis of this kind is not described by the model.

In a typical measurement the material parameters (coupling and anisotropy terms) are fixed and a derived quantity of ϱ_E is measured. Mostly the net magnetic moment M_{net} is measured as a function of the magnetic field H. To reproduce the hysteresis curves we minimize (2.3) for each H numerically, then calculate the simulated result of the measurement from the equilibrium values. In the following the discussion of the energy terms will be developed starting from the simplest model.

2.2 Pure antiferromagnetic coupling

In case of pure bilinear AF coupling with no additional anisotropy terms,[3] the trilayer (or two magnetic layer) model and the infinite layer model can be treated analytically. Due to symmetry considerations (the bilinear term depends only on the angle differences), we may

[1] This implies that the anisotropy term may depend on the orientation of the sample ϑ^{S}. ϑ_i^{S} in (2.3) notes the possible misalignment of a layer's anisotropy compared to ϑ^{S}.

[2] Or equivalently layer magnetic moment per unit area.

[3] In the trivial case of uncoupled layers with no anisotropy the magnetization will be always parallel to the applied external field.

align the external field arbitrarily. For the ease of description we choose $\vartheta_H = 0°$. Also we introduce a scalar H field allowing for $H < 0$ values which is equivalent with $\vartheta_H = 180°$ in the vector picture.

2.2.1 Two magnetic layers

Magnetic films on both side of a non magnetic layer makes the simplest ML, the trilayer. Our focus is on compensated AF coupled MLs, thus we will set equal magnetic moments for the two layers ($M_0 = M_1 = M$):

$$\varrho_E(H) = J\cos(\vartheta_1 - \vartheta_0) - HM(\cos\vartheta_0 + \cos\vartheta_1). \tag{2.4}$$

In (2.4) the coupling term depends only on angles between the layers, thus the net magnetic moment should be parallel with the external field. This condition implies that $\vartheta_0 = -\vartheta_1$. We will call the independent angle $\vartheta = \vartheta_0$ in (2.4):

$$\varrho_E(H) = J\cos 2\vartheta - 2HM\cos\vartheta. \tag{2.5}$$

To get the energy minimum of (2.5), the zero derivatives of angles with positive second derivative should be found. Calculating the derivative will lead to:

$$\frac{\partial\varrho_E}{\partial\vartheta} = -2J\sin 2\vartheta + 2HM\sin\vartheta = 0 \quad \Rightarrow \tag{2.6}$$

$$-4J\sin\vartheta\cos\vartheta + 2HM\sin\vartheta = 0 \Rightarrow \begin{cases} \sin\vartheta = 0 & \to \vartheta = 0° \\ -4J\cos\vartheta + 2HM = 0 & \to \cos\vartheta = \frac{HM}{2J} \end{cases} \tag{2.7}$$

It is easy to verify that above the saturation field $H_\mathrm{s} = \frac{2J}{M}$, the $\vartheta = 0°$ solution will be energetically favourable, while below saturation the net magnetic moment per unit area of the trilayer depends linearly from the external field in the range $-H_\mathrm{s} \le H \le H_\mathrm{s}$:

$$M_\mathrm{net}(H) = 2M\cos\vartheta = \frac{HM^2}{J}. \tag{2.8}$$

In the saturation regions, $M_\mathrm{net} = \pm 2M$.

The energy of the system is parabolic in the unsaturated region and linear, when saturated (see Fig. 2.2):

$$\varrho_E(H) = -J\left(1 + \frac{1}{2}\left(\frac{HM}{J}\right)^2\right), \text{ if } |H| \le H_\mathrm{s} \tag{2.9}$$

$$\varrho_E(H) = J - 2|H|M, \text{ if } |H| > H_\mathrm{s} \tag{2.10}$$

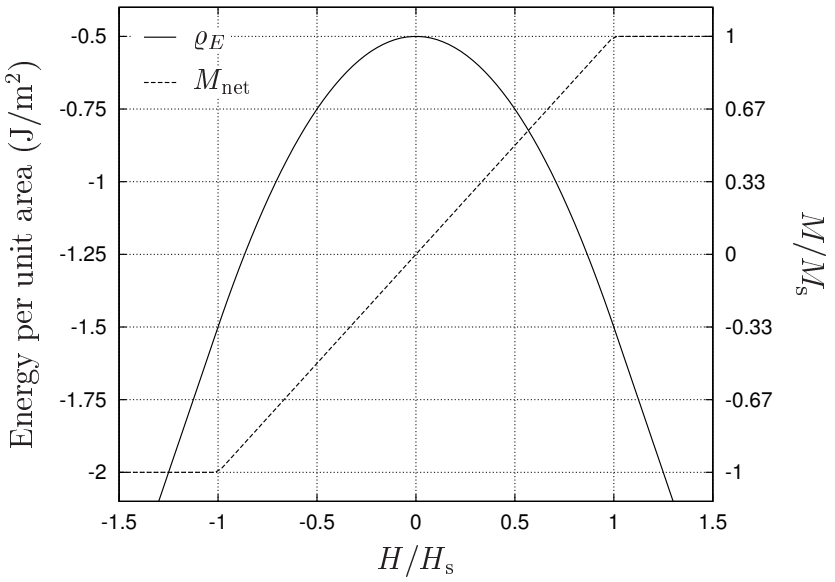

Figure 2.2: Energy per unit area (left side) and normalized net magnetic moment (right side) of an AF coupled model trilayer ($J = 1/2$ J/m^2 and $\tilde{M} = 1$ A) as a function of reduced external field.

Finally, it is worth noting that the number of independent parameters in the above model is one. The direction of the layer magnetizations as well as the energy and the net magnetic moment depend only on $h' = HM/J$. The modification of M and J rescales the magnetization loop, but the independent parameter is the normalized external field h'.

2.2.2 Two-sublattice model

The trilayer was the smallest representation of the magnetic MLs, while a ML with infinite number of layers is located on the opposite end of the spectrum. The usually used model of the infinite stack is a finite ML with periodic boundary conditions (i.e. the first layer is assumed to be identical with the last one). The simplest of those models is the two-sublattice model. Care should be taken when mapping the two-sublattice model to the trilayer as due to the periodic boundary condition the coupling terms will double. We note the quantities of the two-sublattice model with $^\infty$, for example the saturation field will be $H_{\rm s}^\infty$.

2.2.3 Finite number of layers

The majority of MLs are neither trilayers nor infinitely stacked but belong to the class of MLs with 'finite stacking'. For this arbitrary magnetic layer number (2.3) can be minimized numerically. The freedom of the 'dangling' end layers due to their asymmetric coupling results in often neglected effects that we call 'finite stacking' effects. The consequences on the net magnetization (Fig. 2.3) are minute, but may well be seen by depth-selective methods (Fig. 2.4) as the deviation from the bulk is strongest in the first few layers.[4] A comprehensive theoretical

[4] Anisotropy and biquadratic coupling may suppress finite-stacking effects.

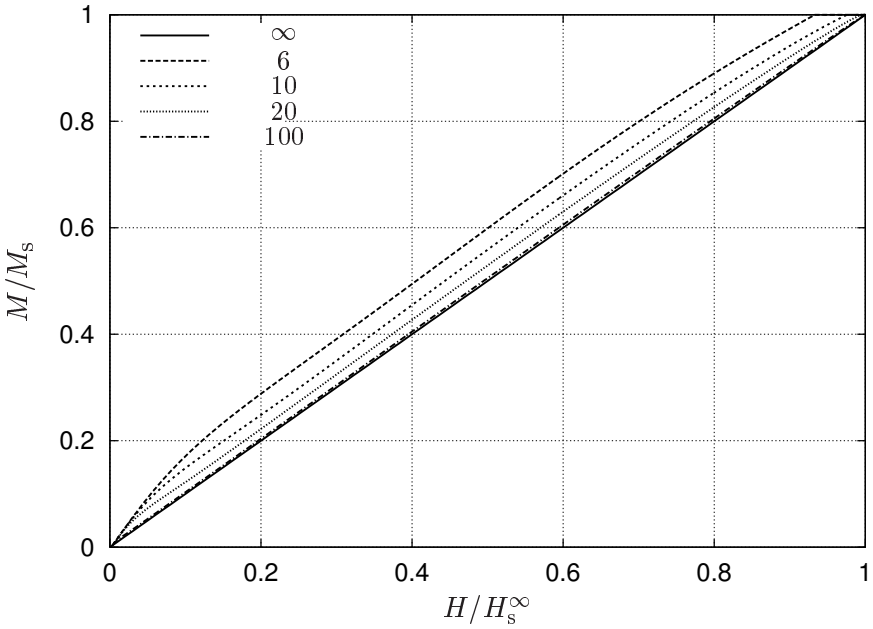

Figure 2.3: The effect of finite stacking on the magnetization of AF coupled MLs. The relative freedom of the end layers due to missing neighbors results in excess magnetization and an earlier saturation compared to the infinite case. The excess magnetization rapidly diminishes with increasing number of layers.

review on finite stacking effects[5] was published by U. K. Rößler and A. N. Bogdanov recently [8].

For numerical simulations of finite stacked MLs we use conjugate gradient minimization based on Numerical Recipes optimization subroutines [9] and coded by the author. The code can search for local and global minimum energy paths with flexible and easily expandable model library.

The effect of finite stacking is most pronounced in the low-field region for even number of layers.[6] If we map the two-sublattice model to the finite stack, then $\vartheta_0 = -\vartheta_1 = \vartheta_2 = \cdots - \vartheta_{n-1}$. However if we do not force the outermost layers to follow the strictly alternating order, then states with a new symmetry and lower energy may appear. At arbitrarily low fields a 'global' twisted state appears, which involves the whole sample [10]. The deviation from the two-sublattice model localizes at the ends as the field is increased. On Fig. 2.5 the result of the numerical simulation is shown. In zero field (a) all first neighbors are antiparallel. In the small field region ($b-d$) a global 'linear' phase emerges with a very small asymmetry towards the x-axis giving the net moment of the ML. At plot (e) the second layers from outside ($n = 1$ and 98) reach their maximal negative angle and from this point on all moments are rotating towards the external field. Increasing the field further ($f-h$) the second layers are retarded compared to the average while in the high field region (k) they are rotated before the 'bulk'. On the boundary of the two phase (i) all moments except the outermost ones are in their bulk

[5] Or as they refer to it in [8], finite-size effects.

[6] We are interested only in compensated MLs. In Refs. [10,11] odd numbers of layers were also treated.

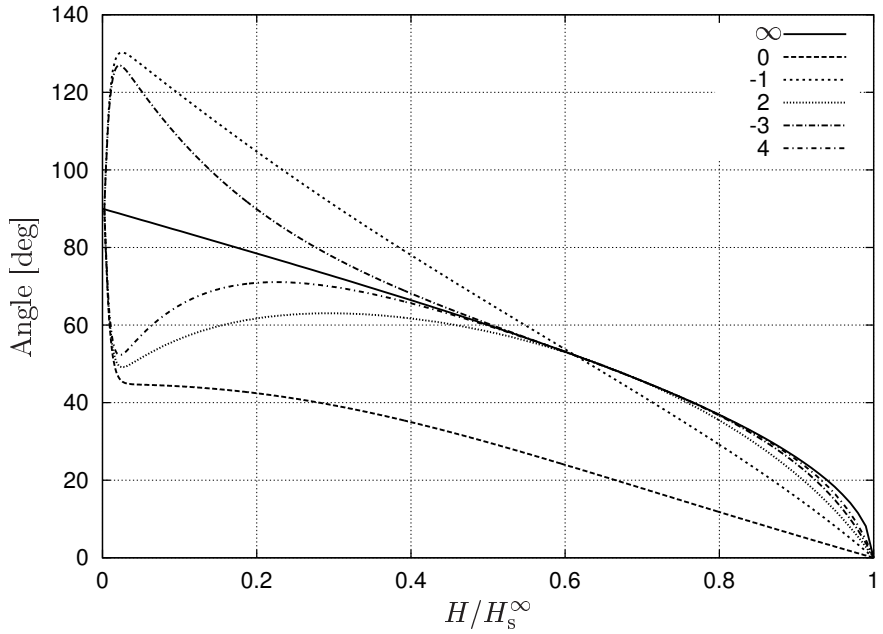

Figure 2.4: The effect of finite stacking on the layer magnetization angles (ϑ_i) in an AF coupled ML with $n = 100$ magnetic layers. The outermost layer ($i = 0$) is always closer to the x-axis as the 'bulk' (denoted by ∞). The next layer ('1') is retarded first, then it is also comes before the others. To make comparison easier the odd-numbered angles were negated (i.e. mirrored to the x-axis).

position. An analytical solution exist for this boundary field.[7] A second field was found (j) where the number of deviating layers has local minima (see also Fig. 2.7). Increasing the field further the ML is reaching saturation (k) and finally saturates (l).

If the number of layers is small, then even the central layers cannot reach their equivalent two-sublattice value, thus the system cannot be separated to bulk and surface regions. On Fig. 2.6 the regions where at least the central layers are in the bulk position are shown. Note that the selection of the region depends on the value of the difference threshold.

When the ML can be decomposed to bulk and surface regions one may ask how many layers are deviating from the two-sublattice solution. Fig. 2.7 also highlights the fact that, due to the first-neighbor coupling, if one layer reached the bulk angle then all the layers towards the center are also in that position. Thus the number of deviating layers L is independent of the total number of layers n for $L < n$. On Fig. 2.8 L is shown as a function of external field. To compare our results with the work of Nörtemann *et al.* [10], one should divide our numbers by two, as we used stacks with two free ends, while Nörtemann assumed a semi-infinite stacking [10].

The effect of finite stacking on global magnetization is 'minute'. Even for a stack with $n = 4$ the saturation is 85% of the infinite stacking and 93% for $n = 6$, which is much smaller deviation than that suggested by Parkin *et al.* [12]. They assumed a reduction in the saturation field H_s

[7] If any spin is in the 'bulk' angle then all spins inwards are also in the 'bulk state'. This is due to the first neighbor coupling. The critical bulk angle ϑ_c of the 'knot' point [8] is determined from $\cos\vartheta_c = \sqrt{3/8}$. Thus $\vartheta_0 = -23.28°$ and $\vartheta_1 = \vartheta_c = 52.24°$.

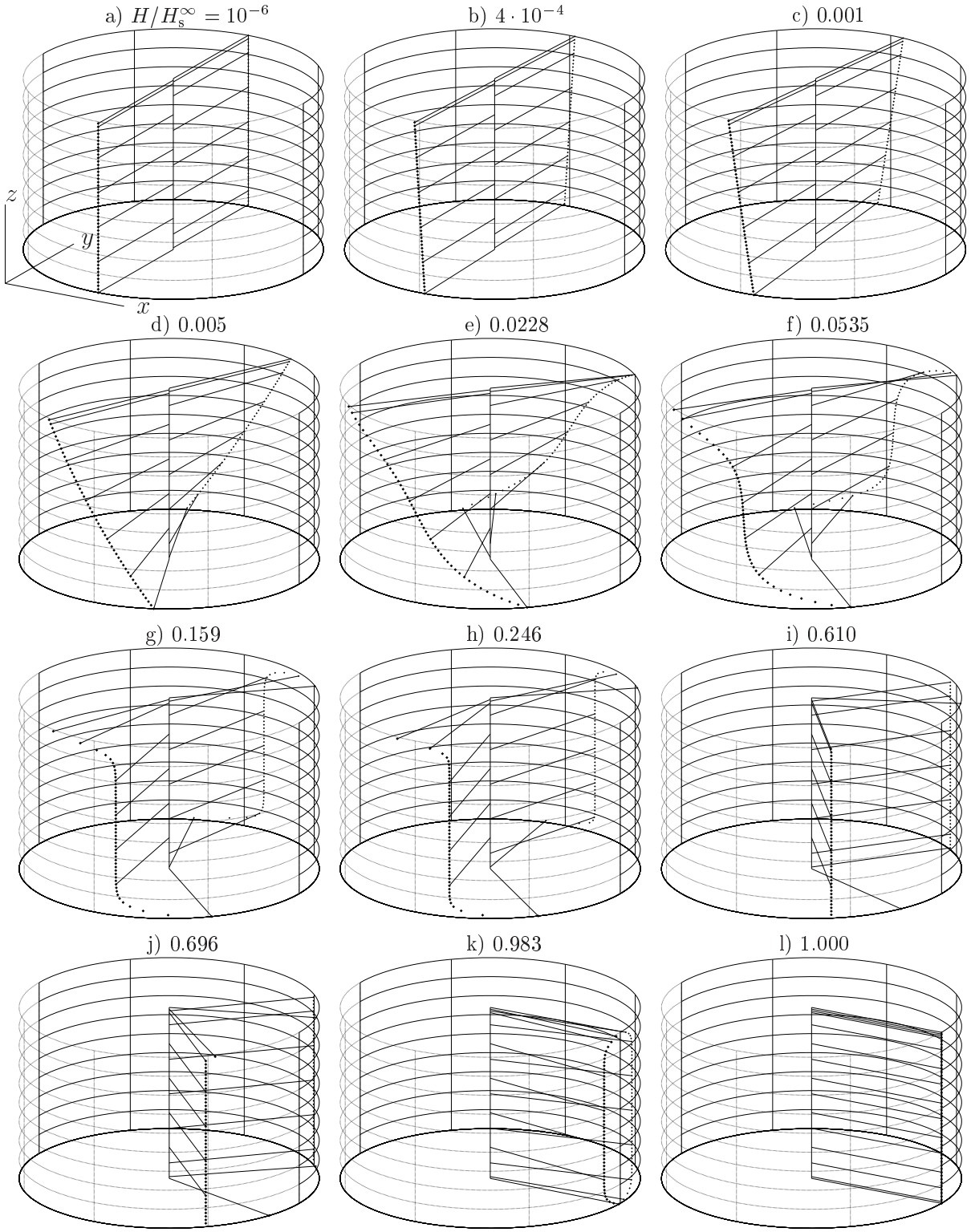

Figure 2.5: Field dependence of an $n = 100$ layer AF-coupled ML. The dots are showing the direction of the layer moments, the rods and circles are guides to the eye. For better viewing layers $n = 0 - 3$ (on top), 10, 20, 30... and $n = 98, 99$ are marked by rods. The field value is normalized to the $n = \infty$ two-sublayer saturation field. The external field was applied along the x-axis.

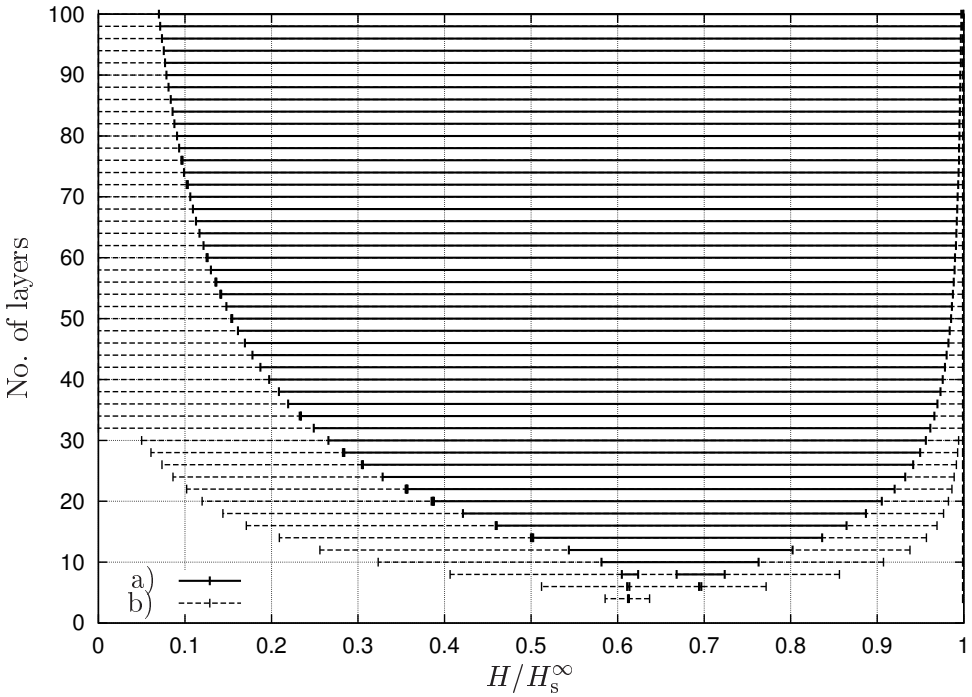

Figure 2.6: The region where the central layers ($i = n/2$) are in the bulk position. Line type a represents the regions where the angle difference of the central layer compared to the bulk value is less than 1° while in the b case the threshold is 10^{-4} rad ($6 \cdot 10^{-3}$ deg). Note that for a short region even $n = 4$ (bottom line) the central layers ($i = 1, 2$ in this case) are in bulk position. From the experimental point of view (line type a) for $n > 30$ the central layer is always in the 'bulk position'.

proportional to $1 - 1/n$. This would give 75% and 83% for $n = 4$ and $n = 6$, respectively. The difference still exists for larger stacks. For example in the case of $n = 20$ numerical calculation yields 99.3%, while Parkin's formula gives 95%.

As mentioned in the beginning of this subsection, the effects of finite stacking are often neglected when evaluating measurements on MLs. To our knowledge the first *direct* experimental evidence for a non-homogenous canting angle due to finite stacking was published in 2002 by Lauter-Pasyuk *et al.* [13]. They utilized polarized neutron reflectometry on AF coupled Fe/Cr MLs and took into account the specular and diffuse scattering to estimate the magnetic configuration (both plane-perpendicular and plane-parallel).

2.2.4 Distribution of the parameters

In an ideal ML all layer magnetizations and couplings are equal to each other ($\forall\, i\, M_i = M$, $J_i = J$). When describing real MLs, differences can occur in the plane of the sample ($x - y$) and perpendicularly (along the z-axis). The plane-parallel variation in layer thickness[8] gives rise to fluctuations in $J_i = J_i(x, y)$ and $M_i = M_i(x, y)$ a possible cause for domain formation (see latter). Even if J_i does not depend on (x, y) due to the growth process the global parameters

[8] Caused by roughness for example.

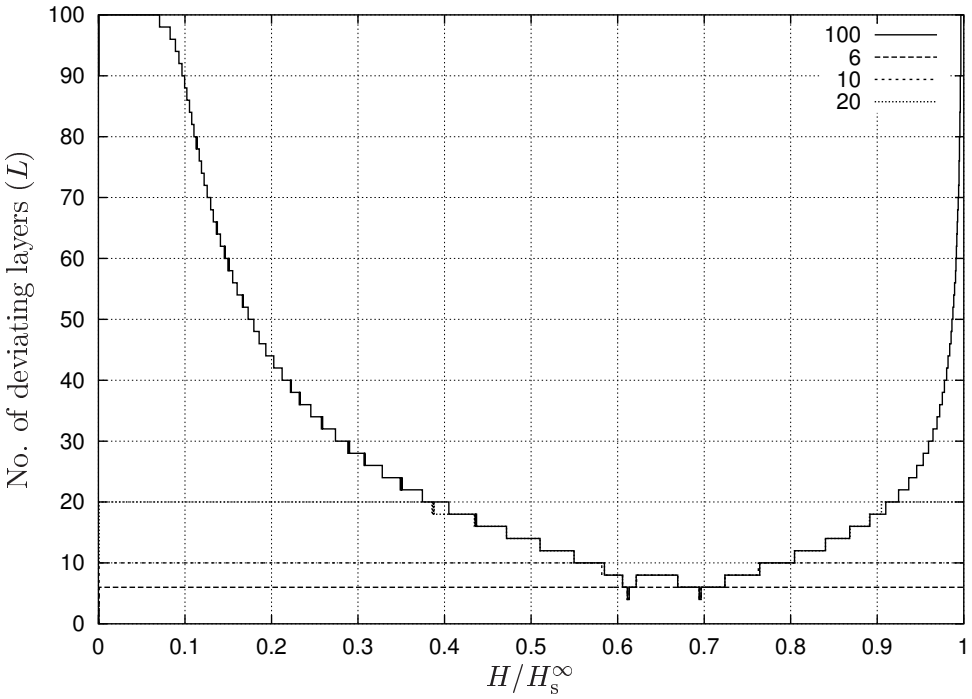

Figure 2.7: Number of deviating layers (L) from the two-sublattice model for different magnetic layer numbers n. The condition was: $\vartheta_i - \vartheta^\infty \leq 10^{-4}$ rad.

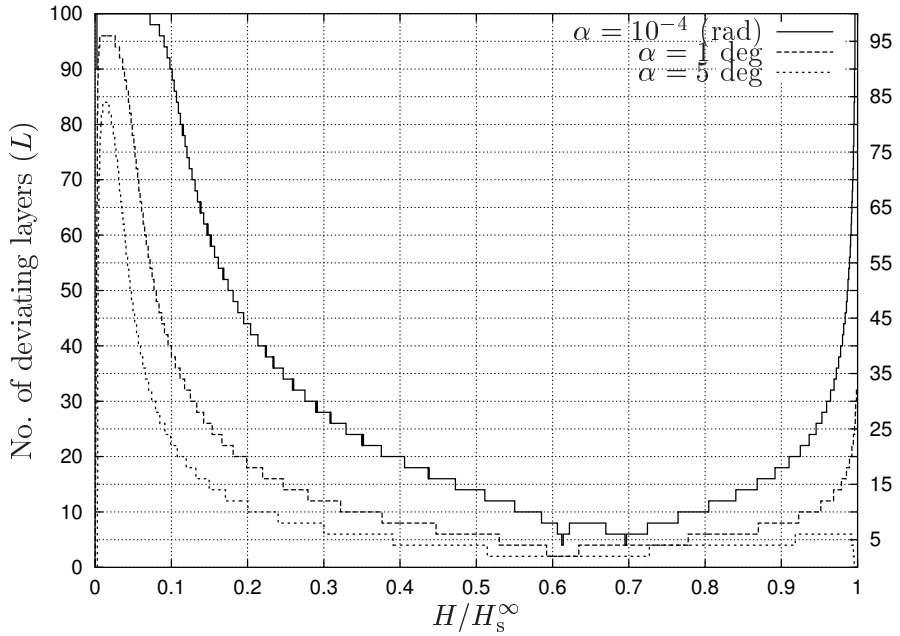

Figure 2.8: Number of deviating layers (L) from the two-sublattice model of a ML with $n = 100$ layers with different threshold values ($|\vartheta_i - \vartheta^\infty| \leq \alpha$).

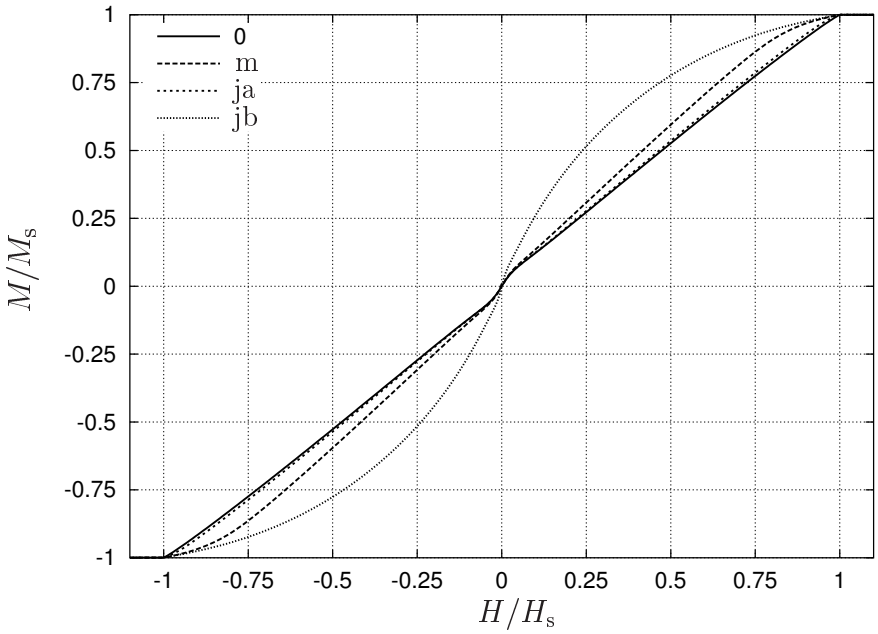

Figure 2.9: Distribution of J_i and M_i in an $n = 20$ ML. Curve (0) is the case where $\forall i\, J_i = J$, $M_i = M$, on (m) the layer magnetizations are $M_0 = 1.2M, \ldots, M_{i-1} = 0.8M$ (the $\pm 20\%$ deviation from the average is linearly distributed in z), on (ja) — which is almost identical to (0) — $J_{0,1} = J$, $J_{9,10} = 0.95J$, $J_{18,19} = 0.9J$ (10% deviation from top to bottom) and on graph (jb) $J_{0,1} = J$, $J_{9,10} = 0.5J$, $J_{18,19} = 0.1J$ (a factor of 10 linearly distributed from top to bottom).

(J_i and M_i) can change with i. In particular cases even full decoupling ($J_i = 0$) of given layers can occur [11].

On Fig. 2.9 we show a few examples of possible effects of J_i and M_i distribution.[9] We assume that the magnetic moment of a given layer grows linearly with layer thickness. As can be seen on curve (m) of the figure the distribution of M_i is not very pronounced. A small change in the AF coupling constant is even less noticeable (curve (ja)) and only a drastic change (which signals a badly prepared ML) shows up significantly (curve (jb)). Note that our main interest are Fe/Cr MLs where the coupling oscillates strongly with the layer thickness [7, 14–16] thus even a small shift in the interlayer thickness can lead to drastic coupling strength change.

[9]The AF coupling is 'linear', thus even with the J_i and M_i distribution the saturation field is well defined.

2.3 Additional coupling terms

Soon after the discovery of AF coupling in Fe/Cr MLs a magnetic configuration caused by biquadratic coupling[10] was found by M. Rührig*et al.* [17]. The possible cause and phenomenological description of the canted coupling is still an open field of research. According to J. C. Slonczewski [18], the origin of the biquadratic coupling is *extrinsic*, i.e. it is related to the actual parameters (thickness fluctuations of the spacer, step density etc.) of the ML. In contrary, J. Barnaś attributes the biquadratic coupling to *intrinsic* mechanisms [19, 20]. The main difference between the two argumentation is that in the first case the AF coupling with the thickness fluctuation produces the biquadratic coupling, while in the second case the biquadratic coupling is present for atomically flat interfaces too. The controversial origin [21] does not affect the 'everyday' use of the bilinear biquadratic formalism for magnetization fitting. For the case of weak AF coupling other phenomenological models were also proposed (see latter).

2.3.1 Biquadratic model

The experimental observations of M. Rührig*et al.* [17] could be described by a biquadratic coupling, which aligns the neighbouring moments perpendicularly to each other. It can be observed best, when the bilinear coupling is small or vanishing but it can affect the global magnetization even in the case of strong AF coupling. The microscopical origin of the biquadratic coupling is still much debated. It is related to different mechanisms in different systems, at different temperatures and different spacer thicknesses (see for example [18–27] and references in [19, 25]). The energy per unit area of a trilayer with pure biquadratic coupling is:

$$\varrho_E(\vartheta) = B\cos^2 2\vartheta - 2HM\cos\vartheta, \tag{2.11}$$

Where ϑ is the angle from the direction of the external field (the x-axis) and $B > 0$ is the biquadratic coupling constant.[11] The first derivative of the (2.11):

$$\frac{\partial \varrho_E}{\partial \vartheta} = -2B\sin 4\vartheta + 2HM\sin\vartheta = 0 \tag{2.12}$$

From this follows:

$$-8B\sin\vartheta\cos\vartheta\cos 2\vartheta + 2HM\sin\vartheta = 0. \tag{2.13}$$

There are two cases. Either $\sin\vartheta = 0 \rightarrow \vartheta = 0°$ or

$$-4B\cos\vartheta\cos 2\vartheta + HM = 0 \rightarrow 2x^3 - x - \frac{HM}{4B} = 0. \tag{2.14}$$

[10] The coupling angle was found to be 90°in remanence.

[11] The two moments should align symmetrically to the external field to minimize the energy. The coupling depends on angle difference that is the source of 2ϑ, while both moments couple equally to the external field.

We used $x = \cos\vartheta$ for shorthand.

Following the derivation of the bilinear case, here again should be an external field value H_s above which the $\vartheta = 0$ is the energy minimum, the forced parallel order. Let us examine the second derivative at $\vartheta = 0$!

$$\frac{\partial^2 \varrho_E}{\partial \vartheta^2} = -8B + 2HM > 0 \tag{2.15}$$

Thus at all $H > H_\mathrm{s}$ $\vartheta = 0$ is stable were $H_\mathrm{s} = \frac{4B}{M}$. Below saturation one could solve the third degree polynomial in $\cos\vartheta$, but it is easier to use numerical minimization.[12] The two-sublattice or infinite model can be derived from the trilayer by setting $B' = 2B$ similarly to the bilinear case. For infinite number of layers

$$H_\mathrm{s} = \frac{8B}{M}. \tag{2.16}$$

At zero external field ($H = 0$) the system prefers the 90°alignment, which means $\vartheta = 45°$. The canted state in remanence causes a jump in the magnetization when the sign of the external field is changed. The further analysis of the pure biquadratic coupling could be done similarly to the bilinear case, but our interest is strongly AF coupled MLs[13] with a possible small biquadratic coupling, thus we skip this analysis.

Bilinear and biquadratic coupling

In the following we will shortly analyze the result of a small biquadratic term added to the bilinear one. Due to symmetry considerations the $\vartheta_0 = -\vartheta_1$ case is taken.[14] The energy per unit area to be minimized will be:

$$\varrho_E = J\cos 2\vartheta - B\cos^2 2\vartheta - 2HM\cos\vartheta. \tag{2.17}$$

The derivative:

$$\frac{\partial \varrho_E}{\partial \vartheta} = -2J\sin 2\vartheta - 2B\sin 4\vartheta + 2HM\sin\vartheta = 0. \tag{2.18}$$

It is easy to see that $\vartheta = 0$ is a solution of (2.18). The stability condition is:

$$\frac{\partial^2 \varrho_E}{\partial \vartheta^2}|_{\vartheta=0} = -2J\cos 2\vartheta - 4B\cos 4\vartheta + HM\cos\vartheta = -2J - 4B + HM > 0. \tag{2.19}$$

Thus the saturation filed is equal to $H_\mathrm{s} = (2J + 4B)/M$. The $H(M)$ curve is again a solution of a third-degree polynomial. In case of strong bilinear coupling ($J > 2B$) the behaviour of the trilayer is similar to that of the pure bilinear case, as we will demonstrate in the following.

[12] In a more general case J is also present leading to difficult — but still analytical — results.

[13] Strong compared to the crystal anisotropies.

[14] In case of crystal anisotropies, the symmetry can break-down, allowing for non symmetric 'L-shaped' configurations.

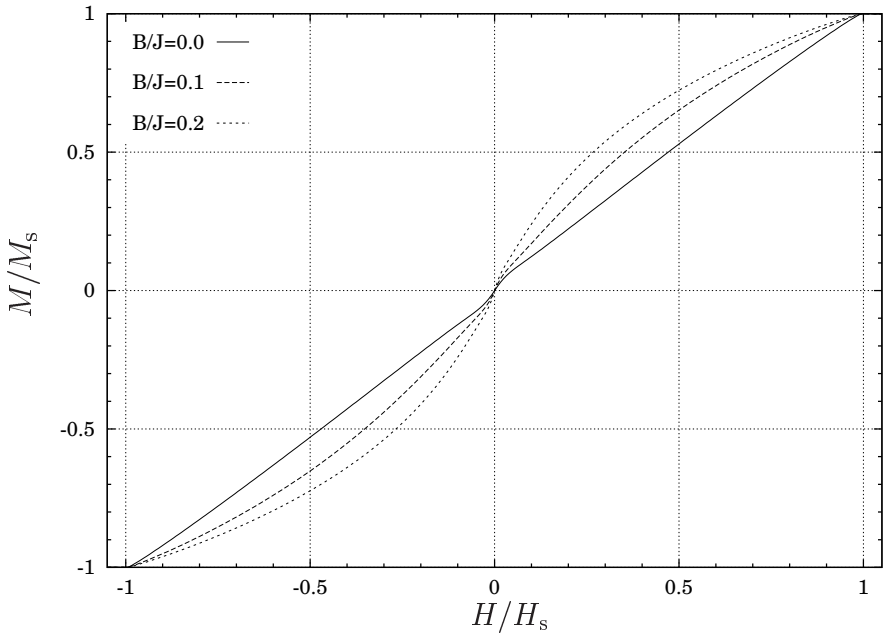

Figure 2.10: The effect of biquadratic coupling on the global magnetization of a ML with $n = 20$ layers.

If $\vartheta \neq 0$ then

$$\frac{\frac{\partial \varrho_E}{\partial \vartheta}}{\sin \vartheta} = -2J \cos \vartheta - 4B \cos \vartheta \cos 2\vartheta + HM = 0 \tag{2.20}$$

If $\cos \vartheta = 0 \rightarrow \vartheta = 90^\circ$ then $H = 0$. We only have to check that at $H = 0$ this is a minimum:

$$\frac{\partial^2 \varrho_E}{\partial \vartheta^2}|_{\vartheta=90^\circ} = -2J \cos 2\vartheta - 4B \cos 4\vartheta = 2J - 4B > 0 \rightarrow J > 2B \tag{2.21}$$

Thus if $J > 2B$ then the behaviour is bilinear-like. In the following we will only focus on this parameter region.

In the case of MLs, the usual $J' = 2J$ and $B' = 2B$ substitution should be used. A demonstration of the biquadratic term on the global magnetization for an $n = 20$ layer is shown in Fig. 2.10.

In conclusion, the presence of a small biquadratic coupling does not change the 'type' of the magnetization loop, but can slightly modify the saturation field and the shape of the curves.

2.3.2 Pinhole coupling

The phenomenological biquadratic coupling was attributed to different origins (see Sec. 2.3.1) but only a few authors considered explicitly the effect of direct ferromagnetic coupling via magnetic pinholes [28]. Magnetic pinholes are direct 'bridges' between the consecutive ferromagnetic layers. Depending on the growth mode it is possible that in spite of the best efforts, atomically flat surfaces cannot be achieved prohibiting the production of MLs with ideally flat layers. In case of uncorrelated roughness the spacer thickness could vanish as the sublayers of the MLs are generally only a few monolayers thick.

We will follow the argumentation of Demokritov *et al.* [29] to show that for the ML we investigated the pinholes could not play a major role. In our particular case the ≈ 13 Å of Cr spacer corresponds to 9 ML of Cr. The interface roughness was found by low angle X-ray reflection to be around 1 ML (see Table 5.2). For this roughness value according to Demokritov *et al.* [29] with a Gaussian fit no pinholes should be present (the probability of pinhole forming is $\approx 2 \cdot 10^{-10}$. If we assume a symmetric roughness of 2 MLs, the pinhole formation probability will be $\approx 2 \cdot 10^{-4}$. The formation mechanism of pinholes is, of course not so trivial thus we can give only approximations for the pinhole density based on magnetization measurements. In conclusion, pinhole formation is possible, but in our particular case the pinhole density is very small.

The effects of the surface roughness and pinhole formation on Fe/Cr MLs were investigated by ion irradiation [29–33]. As a general conclusion the decrease of AF coupling with increasing dose was found. Small doses, however, enhanced the AF coupling [29]. Interestingly the bombardment had almost no effect on the X-ray reflectivity curves of the MLs [30]. Also enhancement of the biquadratic contribution was found in some cases [32].

2.3.3 Proximity model

J.C. Slonczewski proposed a simple heuristic model [18], which is in some sense a generalization of the biquadratic model. The coupling energy term of the proximity magnetism model is

$$E_c = C_+ \{\Delta\vartheta\}_\phi^2 + C_- \{\Delta\vartheta - \pi\}_\phi^2 \tag{2.22}$$

where $\Delta\vartheta = \vartheta_i - \vartheta_{i+1}$ the angle difference between neighbouring magnetic layers, $C_\pm$ (≥ 0) are the coupling coefficients and $\{\varphi\}_\phi$ is the "normalized angle difference", which means adding of multiples of 2π to φ while $|\varphi + n \cdot 2\pi| \leq \pi$ is satisfied ($n \in \mathbb{Z}$). This new $\varphi + n \cdot 2\pi$ value is $\{\varphi\}_\phi$.

The coupling coefficients C_+ and C_- in eq. (2.22) are the ferromagnetic and AF coupling strengths, respectively. In a general case, when both coefficients coexist, the coupling favours a non-collinear alignment. In the special case of $C_+ = C_-$ we get back the perpendicular magnetization alignment.

The simple model of eq. (2.22) is based on the assumption that the AF spacer is polarized by the neighbouring ferromagnetic layers and only a small angle deviation occurs between consecutive atomic planes in the AF spacer thus the description including the first (quadratic) energy term is adequate. The main advantage of the proximity model the prediction of an asymptotic saturation behaviour often observed in Fe/Cr MLs.[15]

[15]Models with biquadratic coupling predict a well-defined saturation field.

2.3.4 Spin-Density Wave (SDW) model

The role of the spin-density wave (SDW) within the Cr spacer of Fe/Cr tri- and MLs has been the subject of controversy since the first discoveries of AF coupling and giant magnetoresistance. For a critical review see [25]. Recently, based on a self-consistent model taking into account the SDW of Cr a theoretical model function was given by V. N. Men'shov and V. V. Tugushev [34, 35].

$$E_c \propto -\left(\Lambda \cos\frac{\Delta\vartheta}{2} + (1-\Lambda)\sin\frac{\Delta\vartheta}{2}\right) \tag{2.23}$$

where $\Delta\vartheta = \vartheta_i - \vartheta_{i+1}$ is the angle difference of neighbouring magnetic layers, Λ is the fraction of the spacer fragments containing an odd number of Cr monolayers. The above result is valid in the limit of low density of steps,[16] while in the high density of steps and $\Lambda = 1/2$ the previously introduced bilinear-biquadratic formalism is regained. The coupling described by (2.23) is also called half angle coupling [37]. Equation 2.23 is valid only at $H = 0$, as the applied external field can change the type of the SDWs [38], which was not investigated. The other limiting parameters are the Cr layer thickness, which should be at least $30 - 40$ Å and the temperature of the measurement, which should be higher than $300 - 350$ K [38].

The SDW model in the low step density limit also gives non-collinear coupling in remanence with a non-trivial angle depending on Λ.

2.3.5 Conclusions

As could be seen from the previous part, the interpretation of magnetization measurements on Fe/Cr MLs is not a trivial task. The growing number of theoretical models show the difficulties of the phenomena. We have to note, however that only the bilinear-biquadratic formalism with strong bilinear coupling gives a collinear AF alignment in zero external field, while in the general cases the other models would predict canted states for remanence. The previously described models give a different magnetization field history, which can be checked for comparison with experimental results.[17] Finally we would like to note that other coupling effects are still possible, see for example the effect of the dipole coupling [39].[18]

[16] Even for smooth interfaces further energy corrections may occur [36], which will not be treated in this work.

[17] According to N. M. Kreines *et al.* [37] the proximity-magnetism model and the half-angle-coupling model describe equally well a given set of Fe/Cr MLs. This is related to the fact that the energy functions of the two models are numerically very close to each other. We think that this could be true for special cases.

[18] In [39] numerical calculations were made on two magnetic layers separated by a nonmagnetic spacer. Depending on the correlated roughness (corrugation) ferromagnetic or AF like coupling was obtained.

2.4 Global versus local energy minimization

Another aspect of our investigations is the 'local' nature of energy minimization. The numerical models used in the literature are 'single-domain' models, rendering one vector to each magnetic layer thus the effects of domain formation (for example hysteresis connected with domain wall motion) cannot be taken into account. By using the single domain energy function the equilibrium state of a coupled ML can be found. Changing the external field, the evolution of the system along local minima can be traced. In some cases more than one stable state with local energy minimum exists, in this case the global minimum is the one with the lowest energy. As was noted by Dieny *et al.* [40, 41] the local and global minima are the borders, which envelope the real behaviour of the ML.

The energy minimum of the purely AF coupled ML is unique, thus always global (see Section 2.2). Not counting the geometrical degeneracy, there is only one configuration for each external field, which one can calculate analytically for trilayers, or numerically for MLs. By introducing crystal anisotropies to the system, the situation will change. In the following we will take a short glimpse on the effects of anisotropies,[19] mainly in the view of the local/global minimum approximation. To have an even simpler picture for demonstration purposes, we are investigating a single magnetic layer.

2.4.1 Uniaxial anisotropy

Magnetic anisotropies in the case of ferromagnetic layers may have various forms depending on the orientation of crystal planes and the epitaxy of growth. For demonstration, we take the uniaxial anisotropy, which can be described with the following energy function:

$$\varrho_E = -U \cos 2\left(\vartheta - \vartheta^{\mathrm{S}}\right) - HM \cos \vartheta \tag{2.24}$$

The uniaxial anisotropy has one easy axis set by ϑ^{S}, while the perpendicular axis is the hard axis ($U > 0$). To understand the above-described system better, let us take some special cases.

Easy direction

Now $\vartheta^{\mathrm{S}} = 0$ thus in this case:

$$\varrho_E = -HM \cos \vartheta - U \cos 2\vartheta \tag{2.25}$$

[19] The anisotropies affect the behaviour of the coupled ML system. If the coupling is strong compared to the anisotropies, we will still have a behaviour resembling the one described in the previous section. If the anisotropies are strong, then the magnetic moments are forced in the easy directions of the anisotropy, resulting in discontinuous jumps [8].

The first derivative should be zero:

$$\frac{d\varrho_E}{d\vartheta} = HM\sin\vartheta + 4U\sin\vartheta\cos\vartheta = 0 \tag{2.26}$$

Case *a)*: $\sin\vartheta = 0 \Rightarrow \vartheta = 0°$ or $180°$. First we examine $\vartheta = 0°$. Let us see if this is a stable minimum:

$$\frac{d^2\varrho_E}{d\vartheta^2} > 0 \Rightarrow HM\cos\vartheta + 4U\cos 2\vartheta > 0 \tag{2.27}$$

$$\text{and } \vartheta = 0 \Rightarrow HM + 4U > 0 \Rightarrow H > -\frac{4U}{M} \tag{2.28}$$

For $\vartheta = 180°$ the same applies:

$$-HM + 4U > 0 \Rightarrow H < \frac{4U}{M}. \tag{2.29}$$

Case *b)*: $\vartheta \neq 0$.

$$HM + 4U\cos\vartheta = 0 \Rightarrow \cos\vartheta = -\frac{HM}{4U} \tag{2.30}$$

But is (2.30) a local minimum? Calculating the second differential of (2.27):

$$HM\cos\vartheta + 4U\cos 2\vartheta = 4U\left(\frac{HM}{4U}\cos\vartheta + \left(\cos^2\vartheta - \sin^2\vartheta\right)\right) = \tag{2.31}$$

(substituting $\cos\vartheta$ from (2.30))

$$= 4U\left((-\cos\vartheta)\cos\vartheta + 2\cos^2\vartheta - 1\right) = 4U\left(\cos^2 - 1\right). \tag{2.32}$$

Because $\cos^2 < 1$ for $\vartheta \neq 0$ and $U > 0$, case *b)* defines a maximum. In other words, in the case of uniaxial anisotropy and easy direction magnetization the layer magnetization can be parallel or antiparallel to the external field, but not canted. In zero external field we have two equilibrium positions ($0°$ and $180°$), while in increasing external field the two minima are shifted relative to each other. The parallel minimum gets deeper, while the antiparallel minimum shifts up in energy (by the $-HM\cos\vartheta$ term) to the border point defined by (2.29) and then ceases to be a minimum. In consequence, in the local-minimum approximation we will have a hysteresis loop, while in the global-energy approximation there appears a jump at zero external field (Fig 2.11). The magnetization of a real system will be always between those two extrema. For a thorough description of trilayers with different anisotropies we refer to the work of Dieny *et al.*, where the authors compared the local [40] and global [41] energy paths for AF coupled trilayers and MLs with cubic (fourfold) and uniaxial anisotropy.

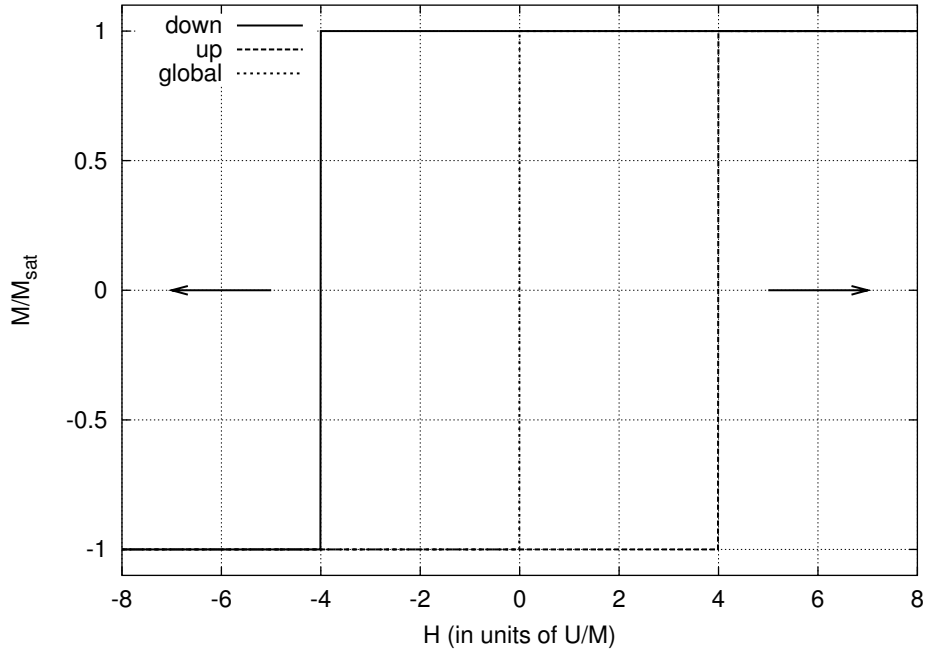

Figure 2.11: Magnetic layer with uniaxial anisotropy, easy direction. Global and local energy minimization. The arrows are representing the magnetic moment of the layer.

Hard direction

Now $\vartheta^{\mathrm{S}} = 90°$ thus the energy will be: $\varrho_E = U\cos 2\vartheta - HM\cos\vartheta$. We can repeat the above discussion with $-U$ instead of U ($U > 0$). Now in case *a)* $H > 4U/M$ for $\vartheta = 0°$ and $\vartheta = 180°$ is stable for $H < -4U/M$, while for the external fields between case *b* is the stable minimum with $\cos\vartheta = HM/4U$, which is the global minimum. If we take the parallel component of the magnetization versus the external field then we have the 'well-known' linear behaviour. The role of the uniaxial anisotropy in the hard direction is similar to the bilinear coupling of a trilayer, as the energy function is similar. In conclusion, in hard direction we have only one energy minimum (no hysteresis) and a well-defined saturation magnetization value.

45° alignment

Finally we investigate a third case, when $\vartheta^{\mathrm{S}} = 45°$. Substituting this value to (2.24):

$$\varrho_E = -U\sin 2\vartheta - HM\cos\vartheta \tag{2.33}$$

$$\frac{d\varrho_E}{d\vartheta} = -2U\cos\vartheta + HM\sin\vartheta \tag{2.34}$$

Equation 2.34 can be solved for $\sin\vartheta$, and the investigation of the minima/maxima can be done as previously. The resulting local and global magnetization curves are shown on Fig 2.13. Here we would like to comment on the asymptotical nature of saturation. From (2.34) it is easy to see that only for $H \to \infty$ will be $\vartheta = 0°$ because for $\vartheta = 0°$ $d\varrho_E/d\vartheta = 2U$ and not 0!

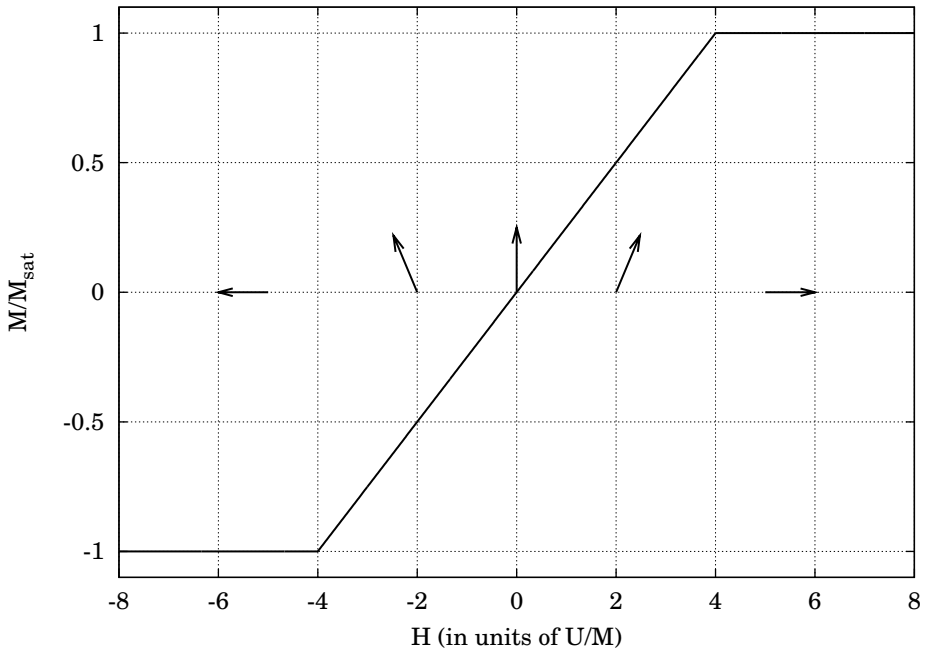

Figure 2.12: Uniaxial anisotropy of a single layer in hard direction. The arrows are representing the canting of the magnetic moment.

The anisotropy term has no extremum at $\vartheta = 0°$ but a maximal slope thus the place of the energy minimum (parabolic + 'slope' as a first approximation) will depend from the field H, resulting in asymptotic saturation.

From the above short section we have learned the difference between local and global energy minimum traces. From the intermediate orientation (45°) we have concluded that the 'normal' behaviour of the systems is the asymptotic saturation, and only exact alignment along special directions (maxima and minima of the anisotropy) gives well-defined saturation field values. The hysteresis in local minimum approximation is also typical for the anisotropy term, missing only in special cases.

2.4.2 Fourfold anisotropy

In this thesis we are focusing on MLs of fourfold anisotropy. We shortly summarize the analytical results for this case based on the calculations presented in the previous section. The energy function in this case:

$$\varrho_E = -H\,M\cos\vartheta - \frac{K}{8}\cos 4\left(\vartheta - \vartheta^{\mathrm{S}}\right). \tag{2.35}$$

Easy direction

The fourfold anisotropy has four easy directions located along two perpendicular easy axes. In global energy minimum the easy magnetization is a 'saturation-to-saturation' anhysteretic

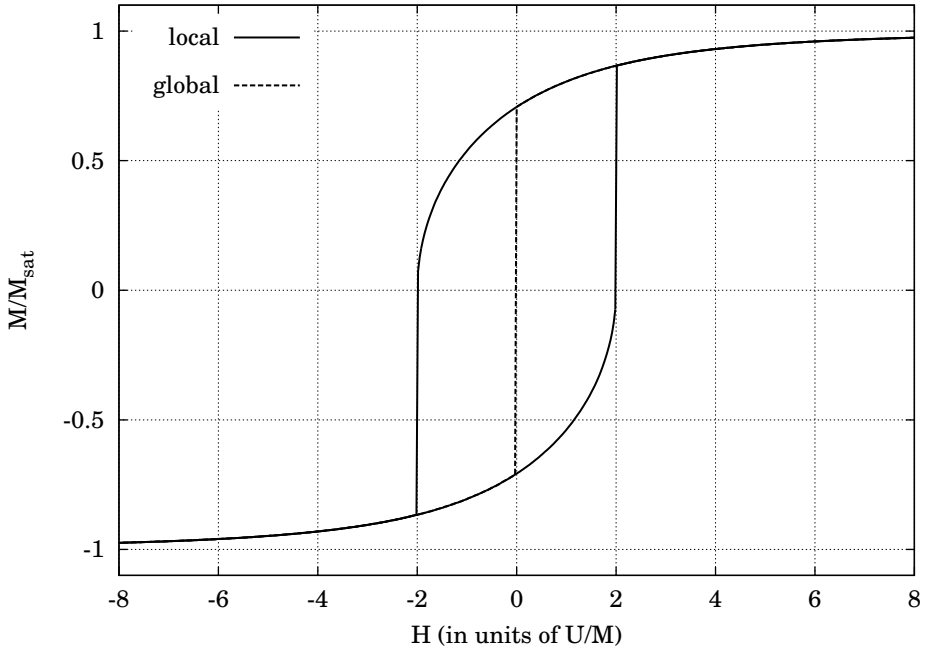

Figure 2.13: Uniaxial anisotropy of a single layer in the 45° direction.

loop. In local energy minima, depending on the starting conditions, different configurations may exist. In the traditional magnetization loop (positive saturation to negative saturation) the obtained hysteresis loop will be very similar to the uniaxial case. The magnetization parallel to the external field in saturation will flip only when the local minimum ceases to be a minimum. It is easy to show that the saturation field is equal to $H_s = -(2K)/M$.

If we prepare the magnetization in remanence for example by rotating the sample, then different scenarios may occur. For example, by turning the sample by 180° we can get back the 'global' loop but more importantly, by turning 90° the magnetization starts from a perpendicular axis.[20] Now the magnetization will be dragged by the external field resulting in continuous rotation towards the hard direction and a sudden jump to 0°, when the Zeeman term competes with the anisotropy barrier. The jump will occur when

$$H M \sin\vartheta + \frac{K}{2}\sin 4\vartheta = 0 \tag{2.36}$$

$$H M \cos\vartheta + 2K \cos 4\vartheta = 0 \tag{2.37}$$

Equation 2.36 sets the local extremum (or inflection point), while (2.37) shows the end of the local minima. Substituting $\sin 4\vartheta = 4\cos 2\vartheta \cos\vartheta \sin\vartheta$ and assuming $\vartheta \neq 0$ we get the following equation: $\cos 2\vartheta \cos^2\vartheta = cos4\vartheta$. Solving this equation graphically and taking into account the position of the minima we get $\vartheta_{\text{crit}} = 65.9°$ and $H_{\text{crit}} = 0.544\frac{K}{M}$. In H/H_s units $H_{\text{crit}} = 0.272$. The resulting magnetization loop is displayed in Fig. 2.14.

[20] This configuration will get practical importance when we combine the anisotropy with the AF coupling, as the AF coupling prefers the perpendicular-to-field axis in remanence.

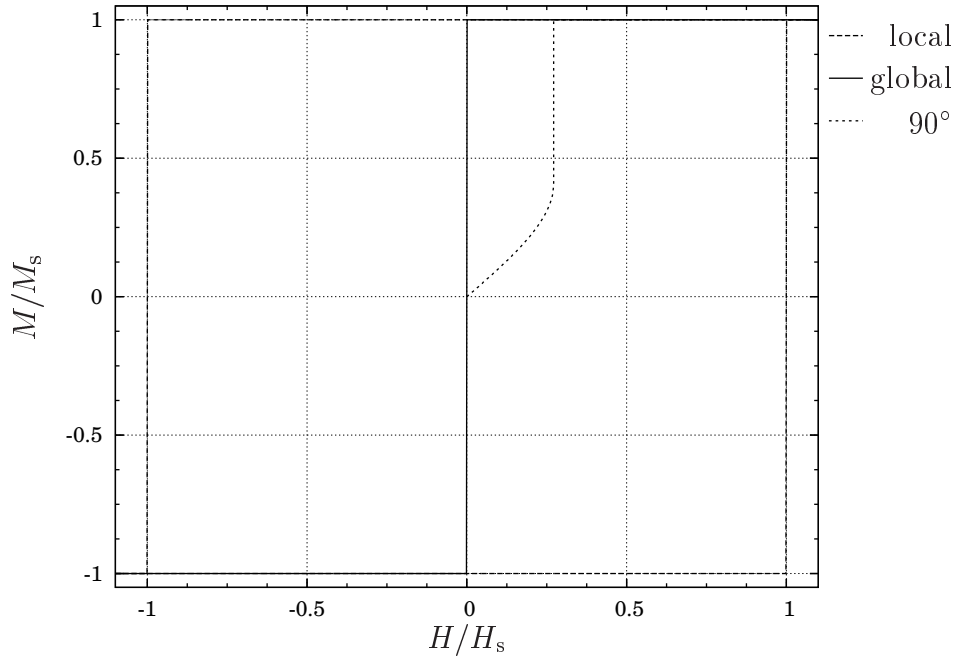

Figure 2.14: Theoretical magnetization loops of a single layer with fourfold anisotropy in the easy axis.

Hard direction

The global-minimum loop in this case will start from an easy direction in remanence and saturating at the hard axis parallel to the external field. The loop goes smoothly as the moment 'climbs' the top of the anisotropy-energy barrier. The only jump will occur at remanence, when the spin flips by 90°. If we take a local-minimum loop then a small hysteresis will occur in the middle due to the fact that the moment cannot jump to the 'towards-the-field' preferred minimum. The magnetization loops are presented in Fig. 2.15. The critical field and angle is the same as for the easy 90° alignment as the same equations have to be solved.[21]

Finally we would like to note that the fourfold anisotropy case is similar to the uniaxaial in the sense that if we are not pointing exactly along an extremum of the crystalline anisotropy, then the magnetization will saturate asymptotically.

2.5 Bulk-spin-flop transition

As already noted, the measured magnetization of a real ML will be between the global and local energy limit. The global energy minimum curve corresponds to the an-hysteretic magnetization process involving no dissipative energy terms. In local minimum approximation, the system can only jump to a new minimum if the actual one cancels to be a minimum, no energy barrier crossing is permitted. The transition called 'bulk spin flop' (BSF) is a typical example of the global *vs.* local behaviour of a real ML.

[21] Equations (2.36) and (2.37) only the sign of K is changing ($+K \rightarrow -K$).

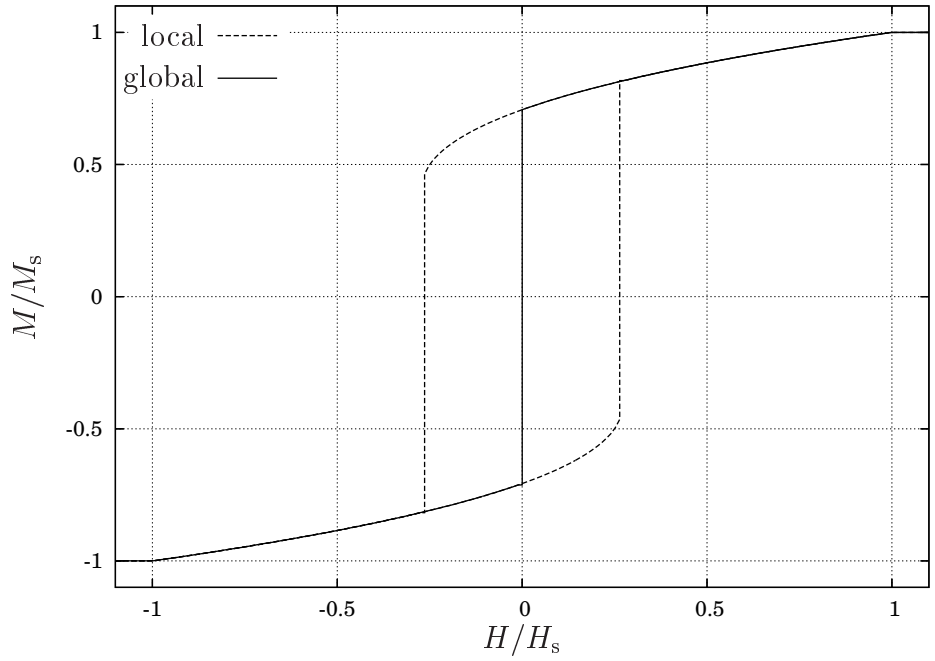

Figure 2.15: Theoretical magnetization loops of a single layer with fourfold anisotropy along a hard axis.

In two-sublattice bulk antiferromagnets with uniaxial anisotropy two stable spin configurations exist. At low external field the anisotropy forces the spins into the easy axis (parallel and antiparallel alignment), while at high fields the moments are perpendicular to the field, forming a <-like shape. In global energy minimization a first order transition (spin flop) occurs when the field is increased trough the critical field value H_{sf} predicted by Néel (see for example page 388 in [42]).

In case of fourfold crystalline anisotropy[22] the parallel/antiparallel and perpendicular AF configurations have the same energy in zero external field. Applying the field along an easy axis, the perpendicular AF state has a lower energy, thus in global energy calculation the parallel/antiparallel state is unstable. In local energy calculation, however the latter state will be an energy minimum for a while, setting an upper limit to the H_{sf} value. For AF-coupled MLs the BSF transition was observed by polarized neutrons by K. Temst *et al.* [43].

The history of the spin-flop phase in thin films starts with the discovery of the Fe/Cr AF coupling. In the famous paper of Grünberg *et al.* [3] the authors show that *"..not only [...] the magnetization of the two Fe films is antiparallel but also that it is perpendicular to the small external field. This is in complete analogy to the spin-flop phase of an antiferromagnet"*. They used single crystal (epitaxial) Fe/Cr trilayer with fourfold in-plane anisotropy. Later Parkin *et al.* [12] showed on polycrystalline Fe/Cr MLs by polarized neutron reflectometry that the initially randomly oriented domains turn to arrangement of $\pm 90°$ from the applied field.

In this work we will use the term 'bulk spin flop' (BSF) to refer to the transition of magnetic

[22]This is the case for Fe/Cr(100) as a result of the projection of the cubic anisotropy to the (100) plane.

moments ('spins') from one easy direction to the perpendicular one of the fourfold in-plane anisotropy. We will use the following energy density per surface area for the system:

$$\varrho_E = \sum_{i=0}^{n-2} J_{i,i+1} \cos\left(\vartheta_{i+1} - \vartheta_i\right) + \sum_{i=0}^{n-2} B_{i,i+1} \cos^2\left(\vartheta_{i+1} - \vartheta_i\right) + \sum_{i=0}^{n-1} \tilde{K}_i^1 \cos^2\left(\vartheta_i - \vartheta_K\right) \sin^2\left(\vartheta_i - \vartheta_K\right) - H \sum_{i=0}^{n-1} \tilde{M}_i \cos\left(\vartheta_i - \vartheta_H\right). \quad (2.38)$$

Where $\tilde{K}_i^1 = K_i^1 d_i$ and $\tilde{M}_i = M_i d_i$ (d_i is the thickness of layer i). The notation of the anisotropy goes according to [44] (p. 130):

$$F_a = K_0 + K_1 \left(\alpha_1^2\alpha_2^2 + \alpha_2^2\alpha_3^2 + \alpha_3^2\alpha_1^2\right) + \ldots \quad (2.39)$$

Where the αs are the direction cosines. In our notation $K_0 = 0$ (a constant will not change the behaviour of the system — it gives vanishing term in the derivatives). For the investigated models magnetizations are in plane, thus only $\alpha_1^2\alpha_2^2$ is nonzero. We will use both notations ($K_1 = K^1$) whichever is more convenient. If not confusing then the tilde will be omitted from $\tilde{K}$ and $\tilde{M}$ in the following. Note that the anisotropy term in (2.38) can be re-written using

$$\cos^2\vartheta \sin^2\vartheta = \frac{1}{4}\sin^2 2\vartheta = \frac{1}{8}\left(1 - \cos 4\vartheta\right). \quad (2.40)$$

This transformation speeds up the computations, because no square computing is necessary. In this notation $J > 0$ for AF coupling, $B > 0$ for the biquadratic coupling. We use ϑ_K to describe the angle of the easy axis and $K_1 > 0$ for the anisotropy term.[23]

2.5.1 BSF in a real ML

As mentioned above, the BSF transition is nonexistent in the global energy picture. In a real system the layer parameters may vary; here we investigate shortly the possible effects.

Numerical calculations show that the slight variation of the coupling constants will cause no dramatic effect. The magnetization curve will have a somewhat different shape but due to the still compensated AF stack, the perpendicular alignment is energetically still more favorable.

In the case of net magnetic moment (caused by the variation of the layer thickness), the situation is a bit different. In the global-energy picture the net moment will force the system in the parallel/antiparallel alignment at arbitrarily low external fields. Then, depending on the net moment, a global spin flop would occur.[24] This flop should be always observable, independent

[23] From here on we stick to the bilinear-biquadratic formalism. In the experimental part we will return to the question of model selection.

[24] In the case of compensated ML the parallel/antiparallel alignment results in a constant energy curve, while

of the field history, which was not the case in our measurements. In local-energy approximation a slight variation in the layer magnetizations will not change the already discussed BSF scenario, as the perpendicular alignment is favored by the anisotropy energy barrier. In the following we will return to the ideal compensated MLs.

2.5.2 Two magnetic layers

Equation (2.38) is valid for *finite* number of layers. If we choose $n = 2$ then we describe a trilayer. To get the infinite (two-sublattice) model $J' = 2J$ should be set.

First we calculate the critical fields for the trilayer, then with the introduction of the new coupling constant (J') the two-sublattice case. From now on all layers are equivalent, thus $K_i^1 = K_1$, $M_i = M$ etc. Also we will examine the easy direction ($\vartheta_K = 0$).

The requirements of a minimum if two variables are present:

$$0. \quad f'_{x_0}(P_0) = 0, \quad f'_{x_1}(P_0) = 0, \tag{2.41a}$$

$$1. \quad f''_{x_0x_0}(P_0) > 0, \tag{2.41b}$$

$$2. \quad \det\left(D^2\right) > 0. \tag{2.41c}$$

The derivatives:

$$\frac{\partial \varrho_E}{\partial \vartheta_0} = J\sin(\vartheta_1 - \vartheta_0) + B\sin 2(\vartheta_1 - \vartheta_0) + \frac{1}{2}K_1 \sin 4\vartheta_0 + HM\sin\vartheta_0, \tag{2.42}$$

$$\frac{\partial \varrho_E}{\partial \vartheta_1} = -J\sin(\vartheta_1 - \vartheta_0) - B\sin 2(\vartheta_1 - \vartheta_0) + \frac{1}{2}K_1 \sin 4\vartheta_1 + HM\sin\vartheta_1. \tag{2.43}$$

The four second derivatives:

$$\frac{\partial^2 \varrho_E}{\partial \vartheta_0^2} = -J\cos(\vartheta_1 - \vartheta_0) - 2B\cos 2(\vartheta_1 - \vartheta_0) + 2K_1\cos(4\vartheta_0) + HM\cos\vartheta_0, \tag{2.44}$$

$$\frac{\partial^2 \varrho_E}{\partial \vartheta_1^2} = -J\cos(\vartheta_1 - \vartheta_0) - 2B\cos 2(\vartheta_1 - \vartheta_0) + 2K_1\cos(4\vartheta_1) + HM\cos\vartheta_1, \tag{2.45}$$

$$\frac{\partial^2 \varrho_E}{\partial \vartheta_0 \vartheta_1} = \frac{\partial^2 \varrho_E}{\partial \vartheta_1 \vartheta_0} = J\cos(\vartheta_1 - \vartheta_0) + 2B\cos 2(\vartheta_1 - \vartheta_0). \tag{2.46}$$

In our case, we are interested in the [0;180] minimum[25] i.e. $\vartheta_0 = 0, \vartheta_1 = \pi/2$:

$$D^2\varrho_E[0;180] = \begin{pmatrix} J - 2B + 2K_1 + HM & -J + 2B \\ -J + 2B & J - 2B + 2K_1 - HM \end{pmatrix} \tag{2.47}$$

---

the perpendicular (<-shape) starts as a parabola looking downwards. In the case of net moment the energy of the parallel/antiparallel alignment is linear, thus there is a region where this latter alignment is the global energy minimum.

[25] $[a;b] := [\vartheta_{2n} = a^\circ,\ \vartheta_{2n+1} = b^\circ]$

The determinant should be positive: $4K_1^2 + 4K_1(J - 2B) - H^2M^2 > 0$. Thus

$$H_{\text{bsf}}^{\text{tri}} = \frac{2\sqrt{K_1(K_1 + J - 2B)}}{M}. \tag{2.48}$$

Condition (2.41b): $\varrho_E''\vartheta_0\vartheta_0 > 0$ is fulfilled at field $H_{\text{bsf}}^{\text{tri}}$. Note that we are interested in strongly AF-coupled systems, thus $J > 2B$. In this case $J - 2B + 2K_1 + HM > 0$ if $H > 0$ (we start from zero external field and apply a positive field to get the spin flop).

At saturation $\vartheta_0 = 0; \vartheta_1 = 0$. Now the second derivative matrix:

$$D^2\varrho_E[0;0] = \begin{pmatrix} -J - 2B + 2K_1 + HM & J + 2B \\ J + 2B & -J - 2B + 2K_1 + HM \end{pmatrix} \tag{2.49}$$

the determinant: $(2K_1 + HM)(2K_1 + HM - 2J - 4B) > 0$, thus

$$H_{\text{s}}^{\text{tri}} = 2\frac{J + 2B - K_1}{M}. \tag{2.50}$$

It is easy to verify that condition (2.41b) is also fulfilled at $H_{\text{s}}^{\text{tri}}$.

2.5.3 Finite number of layers

The trilayer model can be mapped to the two-sublattice model by introducing $J' = 2J$, $B' = 2B$:

$$H_{\text{bsf}}^{\infty} = \frac{2\sqrt{K_1(K_1 + 2J - 4B)}}{M}, \quad H_{\text{s}}^{\infty} = 2\frac{2J + 4B - K_1}{M} \tag{2.51}$$

In a ML of *finite* number of layers the saturation field will be close to the H_{sat}^{∞} value, however the spin-flop field will be the same as for the trilayer model as it will be shown below.

First, let us examine the saturation field. Here the first and the last spins are only 'half-coupled' relative to the inner ones, thus they are closing more easily. The computer simulations show that the difference from the infinite model is decreasing rapidly with increasing number of layers.

The spin-flop field is the same as for the two-sublattice model and can be calculated analytically. This can be shown identically to the proof of A. L. Dantas and A. S. Carrico [45]. In their article they used the second differential matrix ($D^2\varrho_E$) to show their lemma.

For two layers it is easy to see from the derivative matrix

$$M_2 = \begin{pmatrix} a & b \\ b & c \end{pmatrix} \tag{2.52}$$

that the instability occurs when $ac = b^2$. The elements of the matrix are (in our case):

$a = J - 2B + 2K_1 - HM$, $b = -J + 2B$, $c = J - 2B + 2K_1 + HM$. They prove in their article that for any even number of layers $n > 2$ the instability will occur at an external magnetic field where $ac = b^2$. To do this they quote the matrix for four layers:

$$M_4 = \begin{pmatrix} a & b & 0 & 0 \\ b & c-b & b & 0 \\ 0 & b & a-b & b \\ 0 & 0 & b & c \end{pmatrix}. \tag{2.53}$$

Then by transforming the above matrix to an upper triangular form they show that the last element of the product is the smallest and it will vanish in a field where $ac = b^2$. Then they show by mathematical induction that this is valid for the last element of the product for a matrix with two more layers. Thus the spin-flop always starts at the same external field value independently of the number of even layers. Also the values of the other terms were calculated. The even-numbered terms (except the last one) converge to $-b$, while the odd-numbered ones all converge to a. Thus the lemma is valid only for $a > 0$ and $b < 0$. The actual development of the spin-flop is of course dependent on the number of layers. In their derivation they used uniaxaial anisotropy and no biquadratic coupling. By changing the symmetry of the anisotropy only a constant changes in the derivatives in a given point and the introduction of the biquadratic coupling is equal of the change of the AF coupling. The only constraint is that $J > 2B$ otherwise $b < 0$ will not hold. We are interested in strongly AF-coupled MLs, so we will investigate the region of $J > 2B$. It is trivial that the a term is also positive at H_{bsf},[26] which in our case equals to

$$H_{\mathrm{bsf}}^{\mathrm{tri}} = \frac{2\sqrt{K_1\left(K_1 + J - 2B\right)}}{M}. \tag{2.54}$$

In conclusion, the critical fields of the $2n$ finite system ($2n$ is the even number of magnetic layers) are:

$$H_{\mathrm{bsf}}^{2n} = \frac{2\sqrt{K_1\left(K_1 + J - 2B\right)}}{M}, \tag{2.55}$$

$$H_{\mathrm{s}}^{2n} = 2\frac{2J + 4B - K_1}{M}. \tag{2.56}$$

For $K \ll J$

$$H_{\mathrm{bsf}}^{2n} \approx \frac{2\sqrt{K_1\left(J - 2B\right)}}{M}. \tag{2.57}$$

[26] At H_{bsf} $ac = b^2$ and $c > 0$ thus $a > 0$.

2.6 Hard axis spin reorientation

If we magnetize the AF coupled sample along the hard direction, a new reorientation transition ('flop') will occur [8]. The AF coupling prefers a perpendicular-to-field state near remanence, while the anisotropy forces the spins to easy axes $\pm 45°$ off the external field. Depending on the K/J ratio the behaviour will follow more the AF or the anisotropy-driven case. The spin-flop field may depend on the type of minima we follow. In the global minimum picture it is always lower, than in the local minimum case, and in the former case the central AF state always spans a symmetric field range and shows a symmetric hysteresis loop, while the latter could produce asymmetric range and hysteresis loop. The finite stacking effects are also important in this case.

2.6.1 Trilayers

When the system is a simple trilayer then we have only two moments ('spins') and thus the resulting phase diagram is also 'easy' (Fig. 2.16). The limits of behaviour for an AF-coupled ML are set by the global and local minima paths. When performing a magnetization measurement, usually the loop is done by scanning the field from positive saturation to negative saturation and back. When calculating local minimum for such a loop, the middle AF type state might be not reached. The resulting phase diagram is show in Fig. 2.17. The different regions can be separated as follows:

1. **Small-anisotropy region** ($K/J < 0.1$): The local and global minima paths coincide. This is the AF-coupling dominated region where the crystalline anisotropy turns continuously the spins to the 45° easy axis close to remanence. No anisotropy-induced hysteresis is present.

2. **Middle region** ($0.1 \leq K/J < 2$): The anisotropy and coupling term are of the same order of magnitude. The maximal spin-flop field is located at $H/H_s = 0.222$, $K/J = 0.258$. As the anisotropy increases, the spin-flop field decreases, both in local and global path. In the local minima case (Fig 2.17) the spin-flop reaches $H_{\text{crit.}} = 0$ at $K/J = 1.4$, and decreases further. The asymmetry in the local magnetization loops is anisotropy-induced.

3. **High-anisotropy region** ($K/J \geq 2$): Anisotropy dominates. In the local picture the two spins move uncoupled.[27] In the region $K/J > 2.5$ parallel alignment of the spins is possible after the flop, and the '<' phase can jump to '>' phase with no middle AF phase. The global minimum path shows the still existent but diminishing effect of the AF coupling. Detailed investigation of this part could help the understanding of weakly coupled AF MLs.

[27] The consequence of independent alignment is the constant spin-flop field of $H_{\text{crit}} = 0.272$.

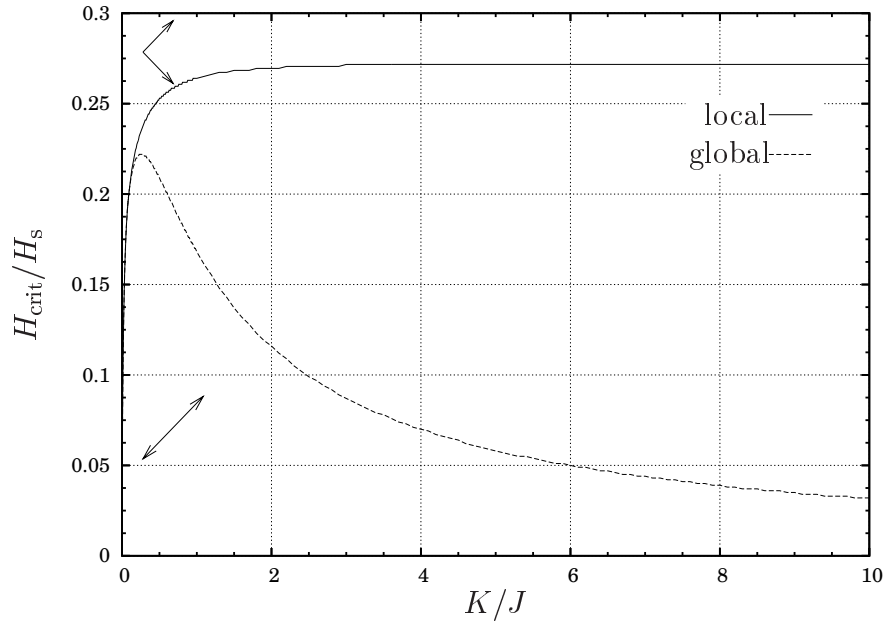

Figure 2.16: Local and global phase diagram of AF-coupled (J) trilayer of fourfold anisotropy (K) magnetized along a hard axis. In remanence the two spins are antiparallel (AF alignment) along one easy axis (see the bottom arrows). As the field is increased (along the x-axis of the graph) the phase transition to the $<$ shape occurs (see top arrows). Taking the local energy path the layer opposite to the external field flops towards the field independently of the AF coupling at large K values, while on the global energy path the diminishing effect of the coupling can be still seen.

In conclusion, from the trilayer model ($n = 2$) we learned that, as expected, there is a smooth transition between the AF-coupling dominated and the anisotropy-ruled regions. The spin-flop has a critical point at $R_c \approx 0.1\,K/J$. Below R_c the transition is continuous (rotation of the spins), above R_c a first order phase transition (spin flop) occurs. For the two-sublattice model[28] we may conclude that the maximal spin-flop field will be at $K/J \approx 0.5$.

2.6.2 Multilayers

The configurational freedom arising from the finite stacking lowers the equilibrium energy by the introduction of new phases. Depending on the minimization used, different loops are possible. The detailed analysis of the 'preliminary' phase diagram[29] (Fig 2.18) yields the following major ranges in the function of the external field:

1. **AF alignment** along an easy axis, with small canting. Here the external field acts as perturbation, driving the system to a state with the net magnetization close to the perp. easy axis (and 45° from the external field). This is the region from zero field up to the *global (b)* line and in the local minimum scenario up to the first line of dots.

[28] To get the parameters of the two-sublattice model, one should substitute $J' = 2J$.

[29] Preliminary in the sense that we have tried to find the easiest measures for the description of the complex phase diagram. To analyze all flops and phase transitions a more thorough study is needed. The situation becomes even more difficult with the addition of further coupling terms.

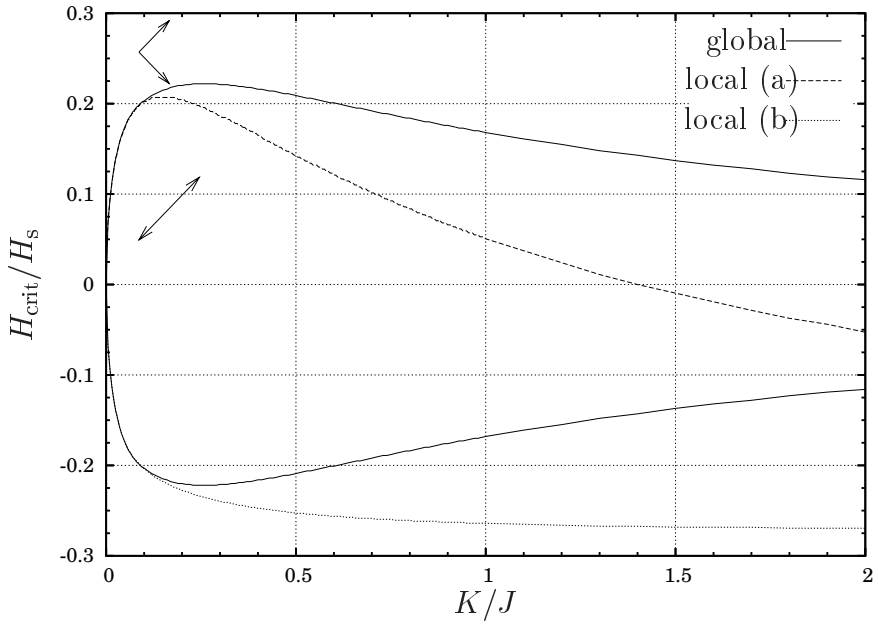

Figure 2.17: Local and global phase diagram of AF coupled (J) trilayer with fourfold anisotropy (K) magnetized along a hard axis. The external field was 'scanned' from positive to negative saturation. The AF coupling forces the phase transition from the '<' phase to the AF one near to remanence. The global path is symmetric while, due to the anisotropy barrier, the local loop gets asymmetric at $K/J > 0.1$. The anisotropy delays the first phase transition (*local (a)*), shifting it to the negative region, while the second phase shift (back to the '>' state, *local (b)*) has an anisotropy-set lower limit (see Fig. 2.16).

2. **'SSF' phase**. In this region very similar phases [5] exist to the surface spin-flop (SSF) transition[30] [46]. In the global minimum approximation the ML is separated to two orthogonal regions by the four middle layers forming a 'vertical domain wall'. This phase is stable up to the field denoted by the *global (a)* line, where the ML switches to the next phase ('<' phase). In the local energy path discrete jumps (marked by black dots) and continuous rotation can be seen. The last spin flops are located in the region, where the infinite two-sublattice system would have the transition (∞ *local*) which is a property of the SSF transition.[31]

3. **'<' phase.** In this region the anisotropy acts as perturbation and the layers are forming the well known '<' phase (the external field is oriented along the x-axis). The total magnetization is parallel with the field and the spins are rotating smoothly up to saturation.

[30]The SSF phase occurs when an AF coupled ML with finite number of layers is magnetized along the easy direction of the uniaxial in-plane anisotropy.

[31]The deeper analysis of the SSF-like phase was not amongst our goals thus it is possible that the phase diagram is not complete. We used the threshold of $\delta\phi > 0.01$ to find discrete jumps in the local graph, where ϕ was the angle of the net magnetization (measured from the x-axis). For the distinction of global phases $\phi > 0.01$ and $\phi > 0.45$ limits were set for phase *global (b)* and *global (a)*, respectively.

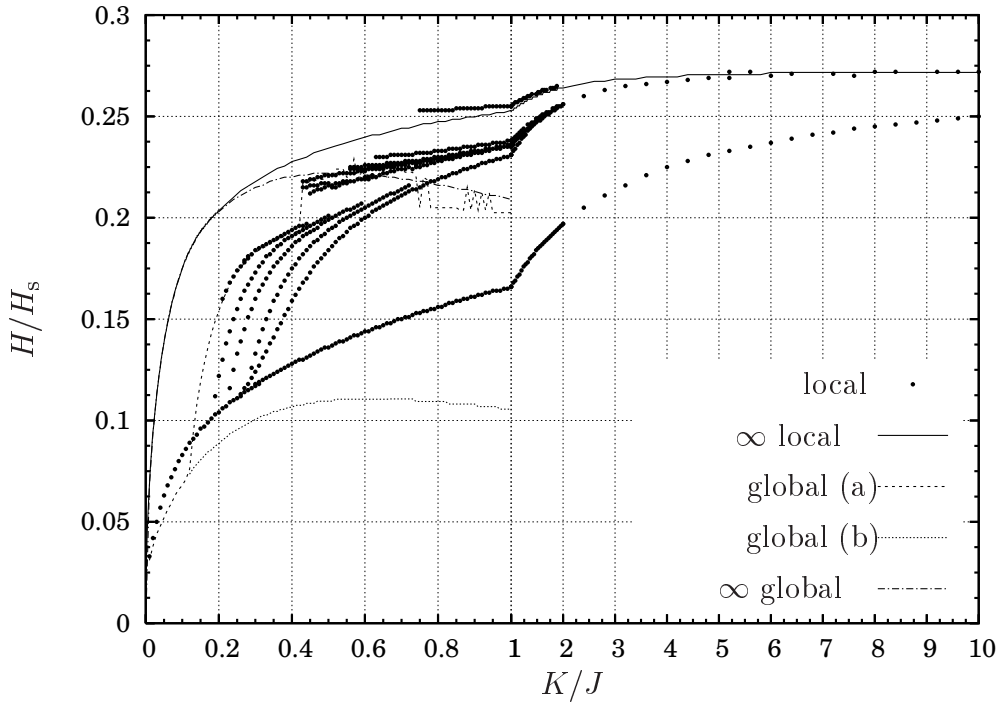

Figure 2.18: Phase diagram of an $n = 20$ ML. The magnetization was swept from zero field to saturation along a hard axis. The local paths were started with a global minimum (AF state along easy direction in remanence). The low anisotropy region $K/J \leq 1$ is zoomed, while for the rest $1 < K/J \leq 10$ only the local minima jumps and the infinite two sublayer model results are shown. For description of the curves see text.

After the analysis of the phase diagram along the magnetization axis we investigate the different anisotropy regions. Three parts can be distinguished:

1. **Small-anisotropy region** ($K/J < 0.1$): The spins from the AF alignment along the easy axis rotate to the canted AF phase ('<') symmetric to the external field. The SSF phase is absent.

2. **Intermediate-anisotropy region** ($0.1 \leq K/J < 2$): The SSF region dominates the transition. The *global (a)* line approaches the ∞ *global* line showing the diminishing effect of finite coupling as the anisotropy gets higher.

3. **High-anisotropy region** ($K/J \geq 2$): The spins are moving 'quasi independently', however, due to the finite stacking, the topmost layer pointing 'in the wrong direction' will flop earlier than the rest (which will flop together) producing the lower dotted line in this region. The final jump occurs at the critical field of the infinite two-sublayer model. Global minimization was not calculated for this region.

Finally the magnetization loop from positive to negative saturation is simulated in local energy approximation. Now the details of the spin-flop are not shown, only the two phase-border lines (Fig. 2.19). Starting from saturation the symmetric-to-field <-phase transforms

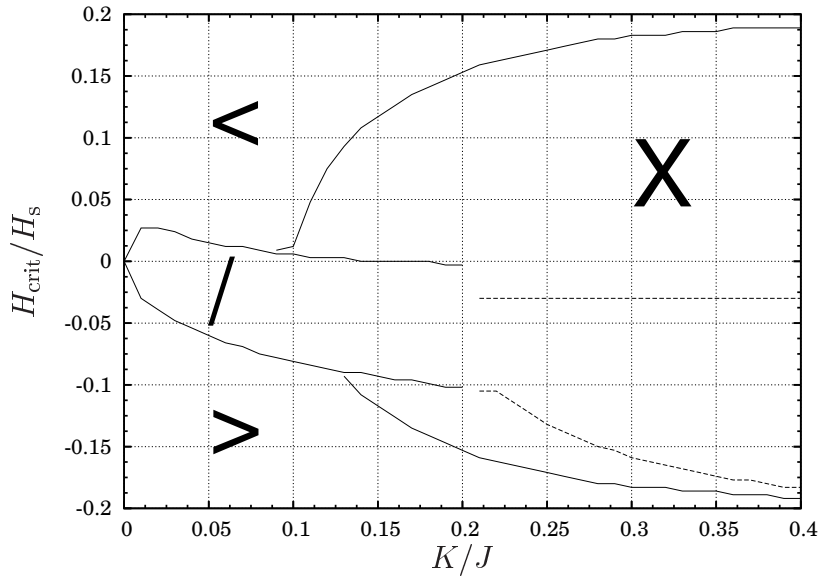

Figure 2.19: Phase diagram envelope of an $n = 20$ ML. The magnetization was swept from positive saturation to negative saturation along a hard axis. Up to $K/J = 0.2$ the two phases (X and /) have a first order transition, while above that point the /-state is not reached, only two small jumps are visible in the magnetization curves (at the field denoted by dashed lines).

to the /-state at very low anisotropy values, rotating to the anisotropy symmetric (easy axis) AF-state in remanence, then aligning in the field symmetric <-state. At higher anisotropy values ($K/J \geq 0.1$) the vertical domain wall state (X-state) emerges, splitting the spins in all four easy directions. Above $K/J = 0.2$ the 'pure AF' state is not reached anymore, as the flops lead to a different X-state. The remanent state (according to these simulations) depends on the K/J ratio. It can be the AF state (up to $K/J \approx 0.15$) or the X-state.

In conclusion, the effects of finite stacking were again underlined. The finiteness of the 'spin chain', the missing coupling term leads to an interesting spin-flop phenomenon resembling the SSF transition. The local and global minimization algorithms suggest different spin alignments, depending on field history, leading to different remanent states. Only measurements on real samples can show, which path is taken by the sample.[32] The effect of higher order coupling terms have to be taken also into account for the particular sample.

[32]By careful sample preparation the starting configuration can be fixed. In our case by saturating the sample in an *easy* direction and letting down the field, then turning the sample by 45° will set the global AF alignment.

Chapter 3

Classical magnetization measurements

After the familiarization with different models of AF coupled MLs we can proceed in the description of a real sample. First the global magnetic behaviour (full magnetization loops and bulk-spin-flop transition) will be presented. The sample under investigation is a strongly AF coupled ML with structural composition of MgO(100)/$\left[^{57}\mathrm{Fe}\left(26\ \text{Å}\right)/\mathrm{Cr}\left(13\ \text{Å}\right)\right]_{20}$. The ^{57}Fe isotope will be important for the Mössbauer studies. Details of structural characterization will follow later in Chapter 5.

3.1 Sample description

The AF-coupled Fe/Cr ML described in our work was grown in Leuven by RIBER MBE. The date of growth was 1999.06.17; the sample was grown by Johan Dekoster and Stephan Degroote. The identification string of the sample was 990608. A cleaned and UHV-degassed (at 600 °C for 30 min.) MgO(100) substrate of $1 \times 1\ \mathrm{cm}^2$ was used. The pressure before growth was $3 \cdot 10^{-11}$ Torr, during growth $3 \cdot 10^{-10}$ Torr. The deposition rates were 0.35 Å/s for Cr and 0.1 Å/s for ^{57}Fe, respectively. The sample was rotated during growth to achieve better lateral homogeneity. The nominal substrate temperature was 450 K during growth. Neither buffer nor capping layer was grown. The nominal thickness profile of the sample was MgO/$\left[^{57}\mathrm{Fe}\left(25\ \text{Å}\right)/\mathrm{Cr}\left(14\ \text{Å}\right)\right]_{20}$. The ^{57}Fe source was a special small volume effusion cell, while Cr was grown from an electron gun. The ML is epitaxial, as was confirmed by in-situ RHEED measurements and ex-situ X-ray diffractograms [47]. It follows the well-known [48] epitaxy of Fe(001)[100]||MgO(001)[110]. From Synchrotron Mössbauer Reflectometry measurements [47] and the measurement techniques detailed in Chapter 5 the structure of $\left[^{57}\mathrm{Fe}\left(26\ \text{Å}\right)/\mathrm{Cr}\left(13\ \text{Å}\right)\right]_{20}$ was deduced.

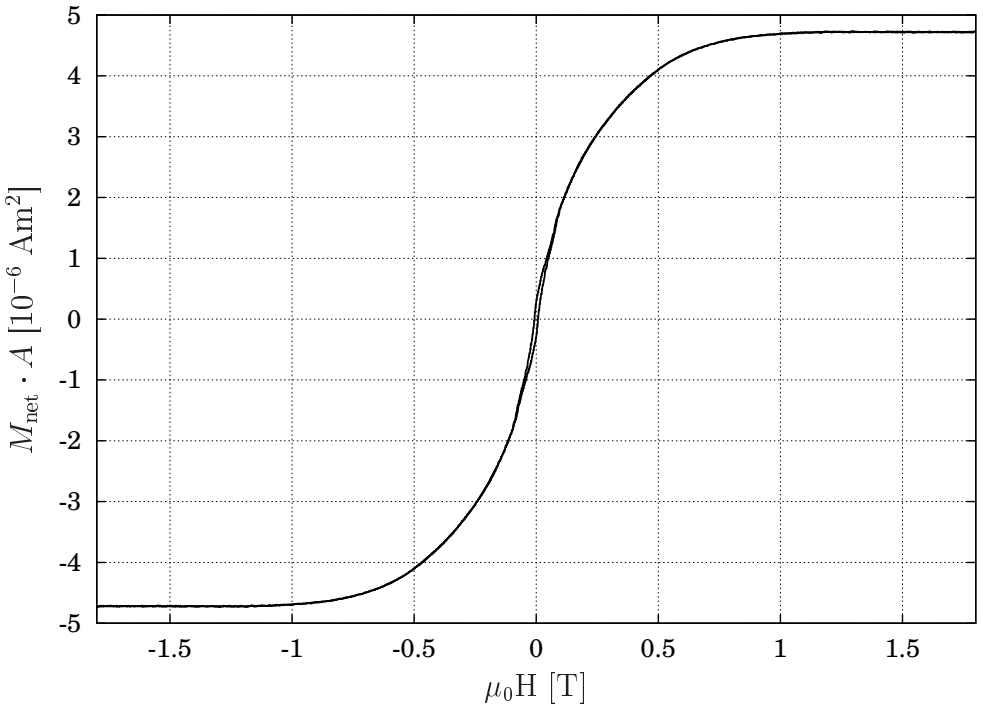

Figure 3.1: The VSM curve of sample 990608 measured in hard direction. The horizontal dimensions of the sample were $A = 7.12 \times 10.2$ mm^2. The net satuartion moment of the sample was$M_{\text{net}} \cdot A = 4.723 \cdot 10^{-6}$ Am^2.

3.2 SQUID and VSM global cycles

The topics of Fe/Cr MLs would not be so interesting if the coupling trough the Cr interlayer would be understood in all details. In the following we will see how to fit a phenomenological model to the hysteresis measurements (Fig. 3.1). The methods used, vibrating-sample magnetometry (VSM) and the superconducting quantum interference device (SQUID) are both capable of measuring the average magnetization of a sample versus the external field with high precision.

3.2.1 First fits

To get a first view, the SQUID measurements[1] were normalized and evaluated.[2] From Fig. 3.2 it is evident that the sample is strongly AF-coupled. The hysteresis is minute, the remanent magnetization is less, than 1%. It can be also seen that the magnetization reaches saturation asymptotically which is not the feature of the bilinear-biquadratic model. The easy- and hard-direction-averaged[3] loops were simultaneously fitted by a finite layer model (Fig. 3.3) and we gained the best fit at the following parameter values with notation according to (2.38): $J = 1$, $B = 0.239$, $\tilde{K} = 0.059$ and $\tilde{M} = 8.363$. Those numerical values are parameters of the

[1] Earlier VSM measurements suffer from the 'phase-slip' effect, see latter.
[2] The SQUID measurements were taken by László Kiss (MTA SZFKI) in May 2002.
[3] The up and down branches were averaged in order to get rid of the hysteresis.

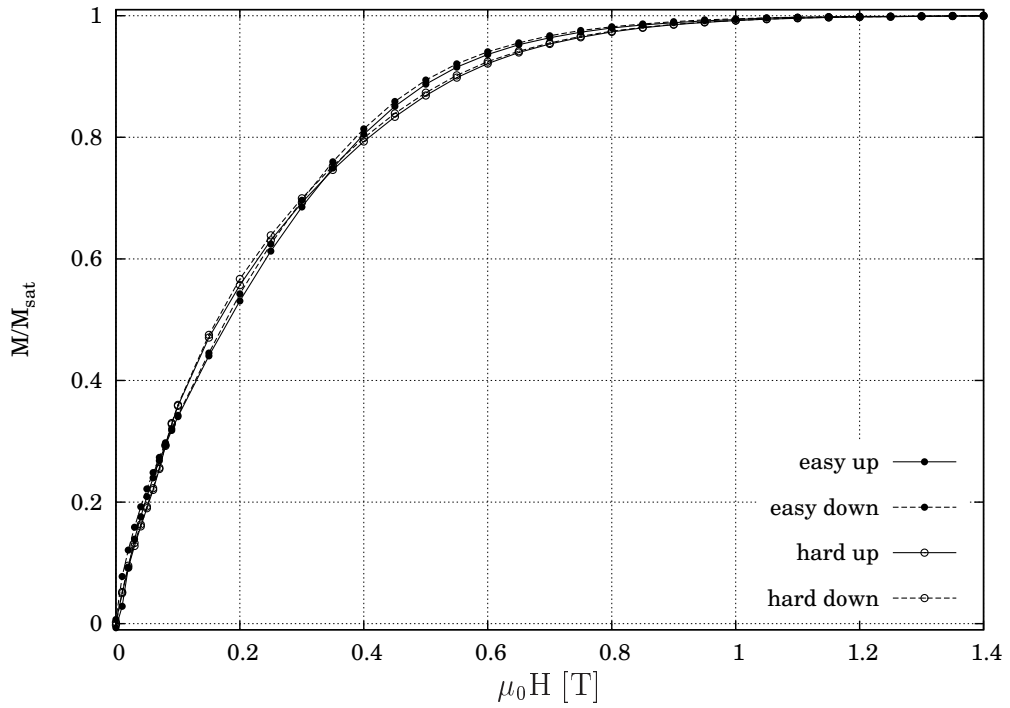

Figure 3.2: Normalized SQUID measurements on a small piece of sample 990608 (easy- and hard-direction magnetization loops). The measurements were taken from 0 T to 5 T and back to 0 T. The lines are guide to the eye.

minimizing algorithm. We compare all coupling and anisotropy terms to the AF coupling, thus $J = 1$ by definition.[4] Finally all parameters are scaled according to the measured saturation magnetization of the sample (see Table 3.2 for example).

Unfortunately the measured total magnetization of the sample depends on the exact geometry (producing different results even for the same orientation). Furthermore, since the SQUID measurements were also taken on a small piece of the sample for averaging on the whole sample the VSM measurements were performed and evaluated. The magnetic moment of the sample as obtained from the hard-direction VSM measurement was $M_{\mathrm{net}} \cdot A = 4.72 \cdot 10^{-6}$ Am^2 (see Fig. 3.1). The area of the sample is 7.12×10.2 mm^2. The total iron thickness (20 layers) is approximately 51 nm (see Chapter 5.1.2). Thus the total iron volume is $3.78 \cdot 10^{-12}$ m^3. From this the magnetization[5] is M $= 1.275 \cdot 10^6$ A/m . This is not far from the $\approx 1.4 \cdot 10^6$ A/m measured by Fullerton *et al.* [14], which is less than the bulk value (see Table 3.1). The number of uncertainties (VSM calibration, phase shift,[6] total Fe thickness, measurement along the hard axis) all sum up in our case.

[4]We could add the units here directly, but this could confuse the reader, as in fact we determine only the ratios of the parameters ($J/\tilde{M}$, $B/\tilde{M}$, $\tilde{K}/\tilde{M}$) because we fit M/M_{s} curves

[5]1 emu=1 Gcm^3, but this G is in "4π" units. See for example [49]. Note that M_{bulk} is magnetization (gives the magnetic moment per unit volume). We 'measure' magnetization in A/m (1 G corresponds to 10^3 A/m).

[6]Due to the lock-in phase shift of the particular VSM set-up it was impossible to give the exact magnetic moment. The lock-in angle was drifting for small samples, thus the slopes of the saturated regions were unequal. It resulted in intersecting or open loops.

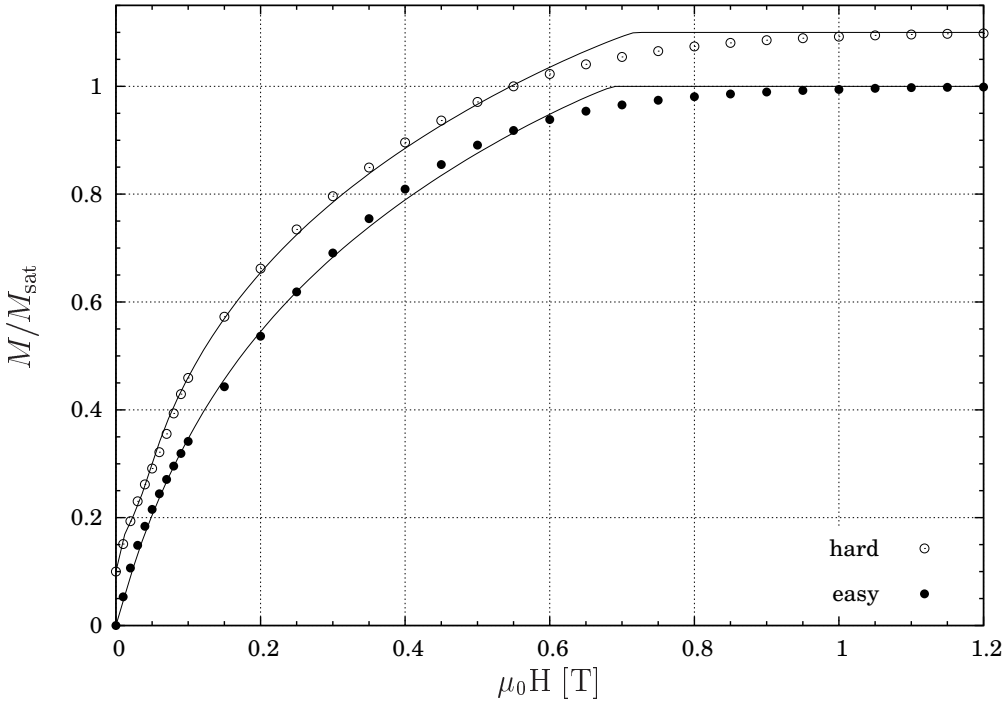

Figure 3.3: Bilinear-biquadratic (BB) fit to the averaged SQUID data. The hard-direction curves are shifted by 0.1 units for clarity. The solid lines are the best fitting curves in the frame of the BB model.

constant	literature value	SI value
$K_{\rm bulk}$	$4.75 \cdot 10^5$ erg/cm^3	$4.75 \cdot 10^4$ J/m^3
$M_{\rm bulk}$	1717 emu/cm^3 (in "4πG" units)	1.717×10^6 A/m

Table 3.1: Literature value [49] of the bulk magnetization density and anisotropy constant of Fe.

Alternative models

As the bilinear-biquadratic (BB) model did not give a good enough fit in the high-field region, other coupling models were fitted. The proximity magnetism model for example did not give a better fit, as it predicts an AF alignment in remanence only if $C_+ = 0$. This constraint does not give enough degrees of freedom[7] to fit the magnetization curves appropriately. The other alternative coupling models are also giving a non-collinear coupling angle in remanence. In conclusion, none of the alternative models can describe the strongly AF-coupled ML with AF alignment in remanence and asymptotic saturation, thus we should apply a different phenomenological model to get a better fit for our sample.

Results of the biquadratic fit

As one can see, the BB fit is better for low field values than for the saturation region. The main shortcoming of the fit is the underestimation of the saturation field. It would give H_{sat} of approximately 0.7 T, while the measured H_{sat} is ≈ 1.1 T.[8] Nevertheless, accepting the BB model, we can approximate the values of the variables describing the ML. As noted above, we will accept $\mathrm{M} = 1.275 \cdot 10^6$ A/m for magnetization. From this the anisotropy density will be $\mathrm{K} = 0.9 \cdot 10^4$ J/m^2, which is only $\approx 20\%$ of the bulk value. $J = 0.389 \cdot 10^{-3}$ J/m^2 and $B = 0.929 \cdot 10^{-4}$ J/m^2.

As we have seen from the above paragraph, there is no 'simple' fit in the frame of literature models of our sample. We define a fit 'simple' when all layer parameters are equal ($J_i = J$, $M_i = M$, ... $\forall i$) and the finite-stacking effects are included. No distributions of parameters and even no deviation of any kind are permitted.

After the realization of the shortcomings of the simple model, a natural way would be to allow distributions, deviations of the parameters. In principle with high enough number of parameters a good fit can be produced with almost any kind of model. Unfortunately enough, we have no direct measurements of the sublattice angles one by one for example,[9] thus from the magnetization data we cannot select amongst the 'sophisticated' models.

3.2.2 Extended bilinear-biquadratic model

A different approach to the extension of the model is the addition of new energy terms to the energy. Based on the two-sublattice inversion (Appendix 9.1) we take the Fourier components of the energy function up to the 12th order.[10] In the two-sublattice model the spins are

[7] Only C_- can be fitted.

[8] It is not easy to give a well-defined saturation field value from the magnetization measurements alone due to the asymptotical behaviour of the magnetization.

[9] This could be achieved by enriching only a single layer with ^{57}Fe.

[10] The higher order Fourier terms give only very small contribution according to the two-sublattice inversion.

param.	model	sample
$\tilde{M} = M \cdot d$	8.367	$1.25 \cdot 10^6$ A/m $\cdot$ 2.6 nm
$\tilde{K} = K \cdot d$	0.126	$1.88 \cdot 10^4$ A/m $\cdot$ 2.6 nm
J	1.0	$0.388 \cdot 10^{-3}$ J/m^2
B	0.2556	$0.876 \cdot 10^{-4}$ J/m^2
J_3	0.0435	$0.169 \cdot 10^{-4}$ J/m^2
J_4	0.0482	$0.187 \cdot 10^{-4}$ J/m^2
J_5	0.0201	$0.781 \cdot 10^{-5}$ J/m^2
J_6	0.0244	$0.948 \cdot 10^{-5}$ J/m^2

Table 3.2: Parameters of the extended model. The column *model* shows the numerical values used in the fitting program, while the last column shows the values recalculated for the given sample.

symmetric to the external field, thus only the following energy terms are taken into account:

$$\varrho_E(\vartheta) = \sum_{m=1}^{6} \frac{J_m}{m} \cos m \cdot \delta\vartheta - \frac{A_4}{4} \cos 4\vartheta - hM \cos\vartheta. \tag{3.1}$$

Here $\delta\vartheta = \vartheta_{i+1} - \vartheta_i = 2\vartheta$ (in the two-sublattice model) and $J_1 - J_6$ and A_4 are the coupling and anisotropy Fourier harmonics, respectively.[11] To compare with existing models the biquadratic and anisotropy terms were substituted:

$$\varrho_E = J \sum_{i=0}^{n-2} \cos(\vartheta_{i+1} - \vartheta_i) + B \sum_{i=0}^{n-2} \cos^2(\vartheta_{i+1} - \vartheta_i) + \frac{K}{8} \sum_{i=0}^{n-1} 1 - \cos 4\left(\vartheta_i - \vartheta^{\mathrm{S}}\right) + \sum_{m=3}^{6} \frac{J_m}{m} \sum_{i=0}^{n-2} \cos m(\vartheta_{i+1} - \vartheta_i) - HM \sum_{i=0}^{n-1} \cos\vartheta_i. \tag{3.2}$$

Here ϑ^{S} is the orientation of an easy axis compared to the external field.

Equation (3.2) is an extended version of the BB model. It allows for 'simple' fitting of the magnetization curve with a few variables. Numerical fitting on an $n = 20$ layer model by sequentially minimizing the parameters give a good agreement with the magnetization measurements as shown in Fig. 3.4. The saturation region fitting is still not perfect, but much better than with the simple BB model. The parameters of the model are summarized in Table 3.2.

The extended model shows a much better fit in the high-field range ($H > 0.5$ T) compared to the BB model and it also yields a larger crystalline anisotropy, which is almost 40% of the bulk value. The saturation fields are $H^e_{\mathrm{sat}} = 0.935$ T and $H^h_{\mathrm{sat}} = 0.995$ T in easy and hard directions, respectively. Comparing the common terms M, J, B the values are approximately

[11] Based on measurements we can exclude uniaxial anisotropy ($A_2 = 0$). The higher anisotropy terms were excluded by fitting the magnetization curves. A better distinction between possible higher order anisotropy and coupling terms could be made only based on magnetization loops taken along more directions.

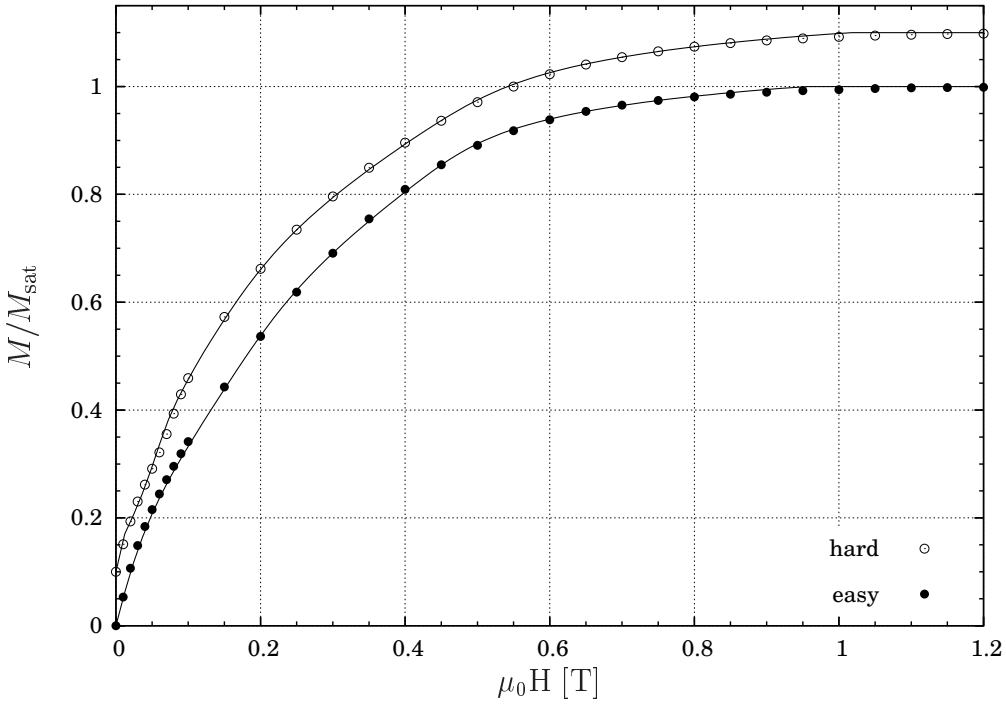

Figure 3.4: Fit by the extended bilinear-biquadratic model of the averaged SQUID data. The hard-direction curves are shifted by 0.1 units for clarity. The lines are the fits to the data.

the same, which is no way a surprise, as the BB model is the subset of the extended Fourier series.

3.2.3 Model-independent parameters

Before we proceed with the elaboration of the magnetization curves, we take a short glance on the model-independent parameters. Based on VSM measurements, we have an approximation on the total magnetization of the ML and the magnetization density (see page 37). We can also approximate the anisotropy of the iron layers.[12]

In the following we will show that the total anisotropy energy is proportional to the area difference between the easy- and hard-direction magnetization loops. Supposing that we have only fourfold anisotropy, subtracting the area of the two magnetization loops[13] we get $\Delta E = 0.425 \cdot 10^{-2}$ T. The anisotropy constant is obtained from $K = 4M\Delta E$, where M is the magnetization (we use $1.25 \cdot 10^6$ A/m) and ΔE is the area difference. We get $K = 2.125 \cdot 10^4$ J/m^3, which is not very far from the value obtained in the frame of the extended model.

To obtain the anisotropy from the magnetization loops one may proceed similarly to [44] (p. 131).

[12]Normally one should measure the anisotropy of a single layer which was grown under similar condition as the ML, but we do not possess such sample.

[13]More precisely the M/M_{sat} loops.

As the external field is coupled to the ML only via the magnetic moments we can write:

$$\int_0^{H_s} M\, dH = -\int_0^{H_s} \frac{\partial \varrho_E}{\partial H}\, dH = \varrho_E(0) - \varrho_E(H_s). \tag{3.3}$$

More precisely, as a direct consequence of (3.2) for example, $\partial \varrho_E / \partial H = -M \sum_{i=0}^{n-1} \cos\vartheta$, which is in turn the measured VSM signal.

Assuming global energy path behaviour, the sample in remanence is in the AF-phase. When saturated, the coupling energy term is the same for the easy and hard orientation, only the anisotropy energy changes. From (3.2) it is easy to see that the difference is $K/4 \cdot n$, where n is the number of layers. As the magnetization is also a 'bulk' parameter, we can rescale the equation to a single layer, or even to the bulk density, arriving to $\Delta E = K/4$. Here ΔE is the area difference of the magnetization loops of a unit volume of the ML. If we measure M/M_{sat}, then we must multiply the result by the bulk magnetization: $(\Delta E/M) \cdot M = K/4$.

3.2.4 Distribution of the parameters

In the previous paragraphs we showed that the sample could be relatively well described by a 'simple' extended Fourier model. This is a phenomenological model. We could follow the other way, by adding distributions of some parameters. However from the magnetization cycles alone it is impossible to decide between a broad distribution – plane-parallel and/or plane-perpendicular – of some parameters and a different model. We cannot decide on those issues by a single sample. In Appendix 9.2 a brief introduction is given, how one can start to examine the distribution case.

Numerical investigations of the model (not detailed here) show that if a single parameter (for example the biquadratic coupling) has a distribution (a narrow Gaussian type for example), then the magnetization curve is almost the same as it would be for the average of the distribution, differing only a tiny bit from it at the saturation region. This finding prefers the Fourier model against the distribution one.

Finally we have to stress that really good description of a ML could be given only based on the knowledge of the 'building blocks' themselves. It does not only include the independent measurement of the anisotropy, bulk magnetization and other model parameters, but the investigation of smaller systems (single layers, trilayers etc.) of the same type. As was measured by Parkin *et al.* [12] even a single Fe layer sandwiched between Cr layers can show a non-rectangular hysteresis loop.

3.3 Bulk spin flop

The bulk spin flop (BSF) was first observed by MOKE[14] on sample 990608 (see Fig. 3.5). As mentioned in Sec. 2.5 BSF transition may occur in uniaxial atomic antiferromagnets or in antiferromagnets of fourfold crystalline symmetry. In the latter case the BSF is related to a local energy minimum path, thus it is only observable in AF-coupled MLs. To observe the BSF a special magnetic sample preparation is needed. The 'spins' should be turned parallel/antiparallel to the field. This can be achieved by increasing the field over the critical field of the BSF, then going to remanence and turning the external field by 90° compared to the last seen field. This can be done most easily by turning the sample itself, the actual procedure that was used at the MOKE measurements. First a 'simple magnetization loop' was recorded in the $-150 : 150$ mT range (not shown), then the sample was turned by 90°, saturated in $\mu_0 H = 0.95$ T. The field was removed and the sample was turned back by 90°. A second loop was taken, starting from zero field. As can be seen in the inset of Fig. 3.5 the magnetization first stayed parallel/antiparallel up to ≈ 10 mT. Then it switched to the perpendicular alignment. The BSF transition was over at ≈ 16 mT. Further BSF scans were taken (not shown) after aligning the spins in (smaller-than-saturation) fields of[15] 150 mT and 30 mT with exactly the same BSF transition range and shape.

After the MOKE justification of the BSF, VSM measurements were also done. First the experimental difficulties lead to no significant result, thus the sample was cooled down in order to enhance the BSF. The perpendicularly magnetized sample[16] was turned by 90°, then cooled to 20 K and measured (Fig. 3.6). The spin flop occurred between 12 mT and 30 mT (but it was not so well defined as for the MOKE case.[17] Later the preparation of the magnetizations was improved by the help of an external magnet. The sample rod was placed between the poles of the magnet, which magnetized the sample in the proper way. Now the room temperature observation of the BSF was possible, see Fig 3.7. The spin flop is now well-defined, and occurred at ≈ 12 mT.

In conclusion, we proved indirectly[18] the existence of the BSF transition. The low-temperature and room-temperature measurements led to similar results and showed an $H_{\mathrm{bsf}} \approx 12$ mT. In the following we will compare these results with theoretical predictions.

[14] Measurements were taken by Johan Swerts and László Bottyán in Leuven Aug. 2000.

[15] By passing the BSF transition from below the spins will align to the perpendicular-to-field orientation. There is no need to saturate the sample.

[16] In this stage the magnetization was done by the superconducting solenoids of the VSM machine.

[17] This could be attributed to the improper magnetization procedure for example.

[18] The VSM and MOKE measurements give an incoherent sum of all sublayer magnetizations. We cannot exclude other spin configurations leading to a similar result.

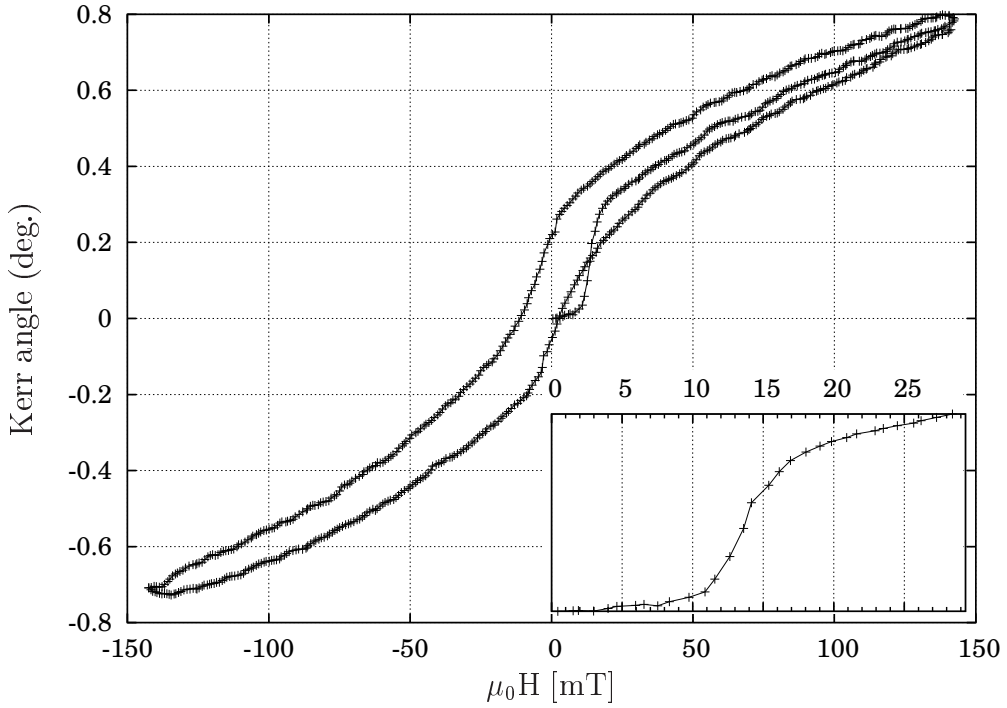

Figure 3.5: BSF transition observed by MOKE (for details see text). The inset shows the zoomed BSF region.

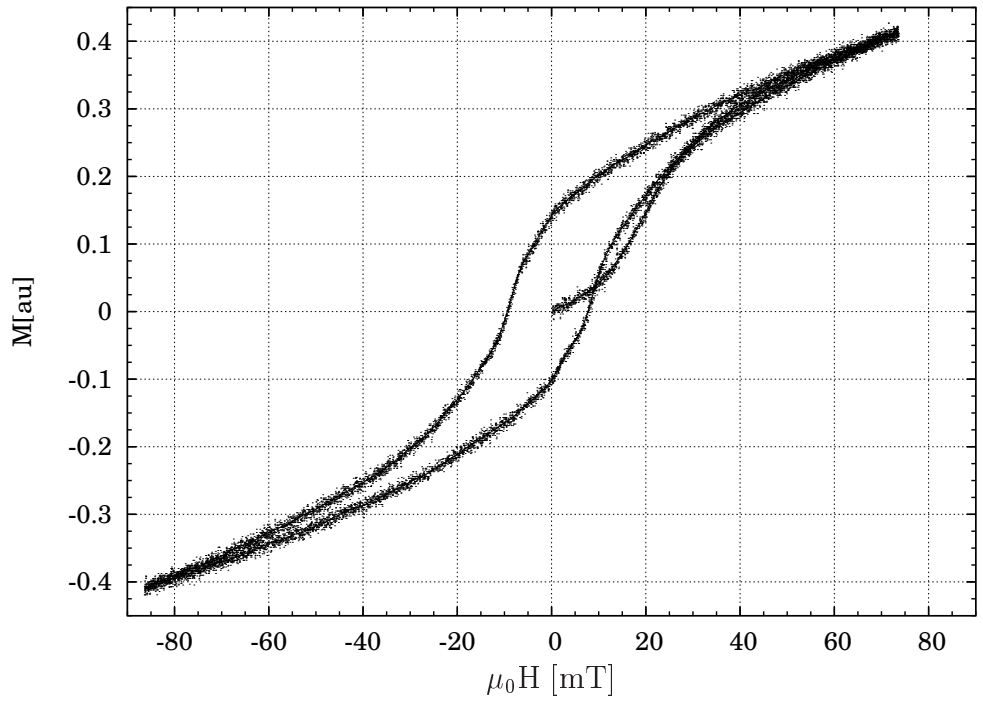

Figure 3.6: BSF transition observed by VSM at 20 K (for details see text). The curves are guide to the eye.

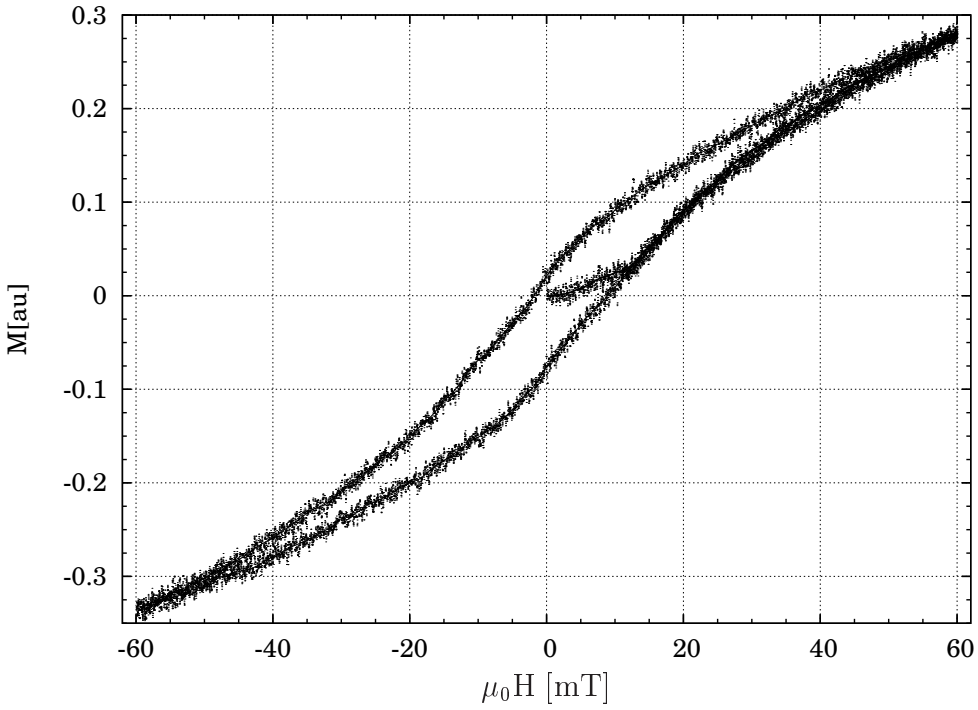

Figure 3.7: BSF transition observed by VSM at RT. The curves are guide to the eye. The spin flop branch is printed in bold for clarity.

3.3.1 Theoretical considerations

The effects of the finite stacking were discussed in Section 2.5. The only difference is now that the coupling is extended with further Fourier terms. As this is not changing the 'global' behaviour, the BSF field and saturation field equations still hold. The new critical fields will be the following:[19]

$$H_{\mathrm{bsf}} = \frac{2\sqrt{K\left(K + J - 2B + 3J_3 - 4J_4 + 5J_5 - 6J_6\right)}}{M}, \tag{3.4}$$

$$H_{\mathrm{s}} = 2\frac{2\left(J + 2B + 3J_3 + 4J_4 + 5J_5 + 6J_6\right) - K}{M}. \tag{3.5}$$

Substituting the values obtained by the fits this will result in $H_{\mathrm{bsf}} = 60.4\,\mathrm{mT}$, $H_{\mathrm{s}}{}^{\mathrm{easy}} = 0.965\,\mathrm{T}$, $H_{\mathrm{s}}{}^{\mathrm{hard}} = 1.025\,\mathrm{T}$. Those results are in extremely good agreement with the numerical simulation, verifying the algorithms used by the optimization code for this particular case.[20] The obtained H_{bsf} field however is much larger than the measured 12 mT. This is a strong indication that the spin flop occurs by intralayer domain wall movement and not coherent rotation of the lattice spins [47]. The domain wall movement can drive the spins trough the local energy barriers. The spin-flop field is not zero, thus the system moves between the global and local minimum path, closer to the global side.

[19] Modifying the calculations presented in 2.5.3 with the constraint that the additional coupling terms do not destroy the general symmetric AF coupling behaviour.

[20] The numerically achieved values: $H_{\mathrm{bsf}} = 60.28 - 60.65\,\mathrm{mT}$, $H_{\mathrm{s}}{}^{\mathrm{easy}} = 0.959\,\mathrm{T}$, $H_{\mathrm{s}}{}^{\mathrm{hard}} = 1.0196\,\mathrm{T}$

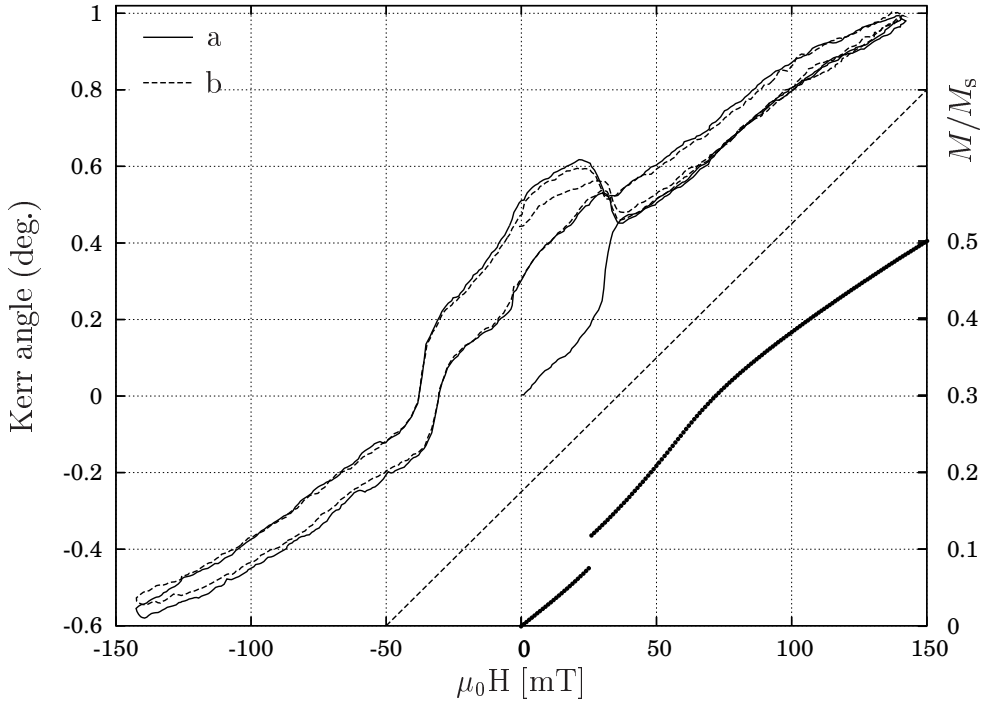

Figure 3.8: MOKE hysteresis loop in the hard direction. The field history was $0 \to 150 \to -150 \to 150$ mT. The first loop (a) was taken after an easy direction loop, while the second one (b) was a repetition of (a). In the inset at the bottom left corner the result of the numerical simulation is shown. The jump on the net magnetization is 0.04 measured in units of M/M_s.

3.4 Hard-axis spin reorientation

The easy-direction hysteresis loop of a strongly AF-coupled sample with fourfold anisotropy is a 'smooth curve'. When the sample is saturated, all magnetic vectors point parallel to the external field, and to an easy direction. When the field is lowered, the moments open smoothly trough a <-phase. They pass the hard axes continuously, arriving to the easy-axis orientation in remanence. In a hard-direction scenario the moments are pointing parallel to a hard axis in saturation, while located along easy directions in remanence. The hysteresis loop in hard direction and the transition of the magnetizations from the hard to easy axes can be smooth or sharp depending on the model parameters (for detailed analysis see Sec. 2.6). In our particular case the magnetization curve showed a well-defined jump in the hard-axis MOKE measurements (Fig. 3.8). Numerical simulation with *global* energy minimization[21] also pointed out a sharp phase transition (see Fig. 3.9).

At increasing fields the first smoothly rotating magnetizations jump when the system chooses a state with different symmetry. This phenomenon is also related to the finite stacking 'freedom' of the ML, as opposed to the two-sublayer model, the layer magnetizations can occupy all four perpendicular easy directions by creation of a 'domain wall' (see the 26 mT

[21] As already noted, the ML can move between the global and local minima. For the easy-direction BSF transition we observed such behaviour close to the global minimum. In the case of hard axis reorientation the local minimum loop would lead to an asymmetric spin reorientation, not observed in the MOKE measurements.

state in Fig. 3.9). The rearrangement of magnetization could be seen by magnetization measurements. MOKE measurements on the sample did show the jump at ≈ 32 mT, but it was not observable either on the VSM curves or in SQUID measurements. The SQUID loop was taken with 10 mT/point in this region, thus it was too coarse to see such a jump. The step width of the VSM measurement (0.88 mT/point) would allow the observation of such a jump, but it was not observed on the loops.

The reasons of the missing jump in the global methods (VSM, SQUID) could stem from many factors. First of all, the jump in the parallel magnetization is minute, 0.04 in units of saturation magnetization, see inset in Fig. 3.8. A small distribution in the parameters can smear it out to the noise region. Secondly, VSM and SQUID sees the magnetization of the whole sample, while at MOKE measurements only a tiny fraction of the sample is illuminated with the laser beam. Finally MOKE is 'surface sensitive' in the sense that it enhances the signal coming from the first layers and due to mixing of different MOKE signals the jump is even more pronounced thanks to the 'negative' kink of the magnetization loop.

The effect of sample misorientation was investigated. Up to $\pm 5^\circ$ the 'jump' is preserved in the MOKE measurements (not shown) with the same averaged flop field of 32 mT. The numerical simulations for the sample reproduce this feature, however showing a slight shift in the critical field.

Finally we note that Aliev *et al.* found a similar effect on the hard-direction AC magnetic susceptibility data [50], which they attributed to the spin reorientation from easy to hard direction. Their sample $\left[\mathrm{Fe}\left(30\ \text{Å}\right)/\mathrm{Cr}\left(13.5\ \text{Å}\right)\right]_{10}$ was very similar to '990608', and numeric simulation of an $n = 10$ ML show an even more pronounced jump. In this case the transition region dominates the stack, leaving only $\approx 2-2$ outer layers in the AF configuration. In our view the jump is not a consequence of an 'easy-hard' transition but an $/-X$ one.

3.5 Conclusions

After the introduction of the effects of finite stacking in the previous part, we tried to magnetically characterize our samples with 'traditional' magnetometry. We used an extended phenomenological model, based on the bilinear-biquadratic formalism to fit the hysteresis loops of sample '990608'. In this Chapter we also introduced two types of spin flop transitions for AF-coupled artificial MLs with fourfold anisotropy. The BSF transition and the hard-axis spin-reorientation (HASR) transition were numerically investigated with the parameters obtained from the fit of the hysteresis loops. In the case of BSF we concluded that domain wall motion, rather than coherent rotation plays major role in the transition.[22] For HASR transition the numerical simulation with global minimization showed good agreement with the MOKE measurements.

[22] We will see that even not domain wall motion, but domain wall annihilation occurs at the BSF transition.

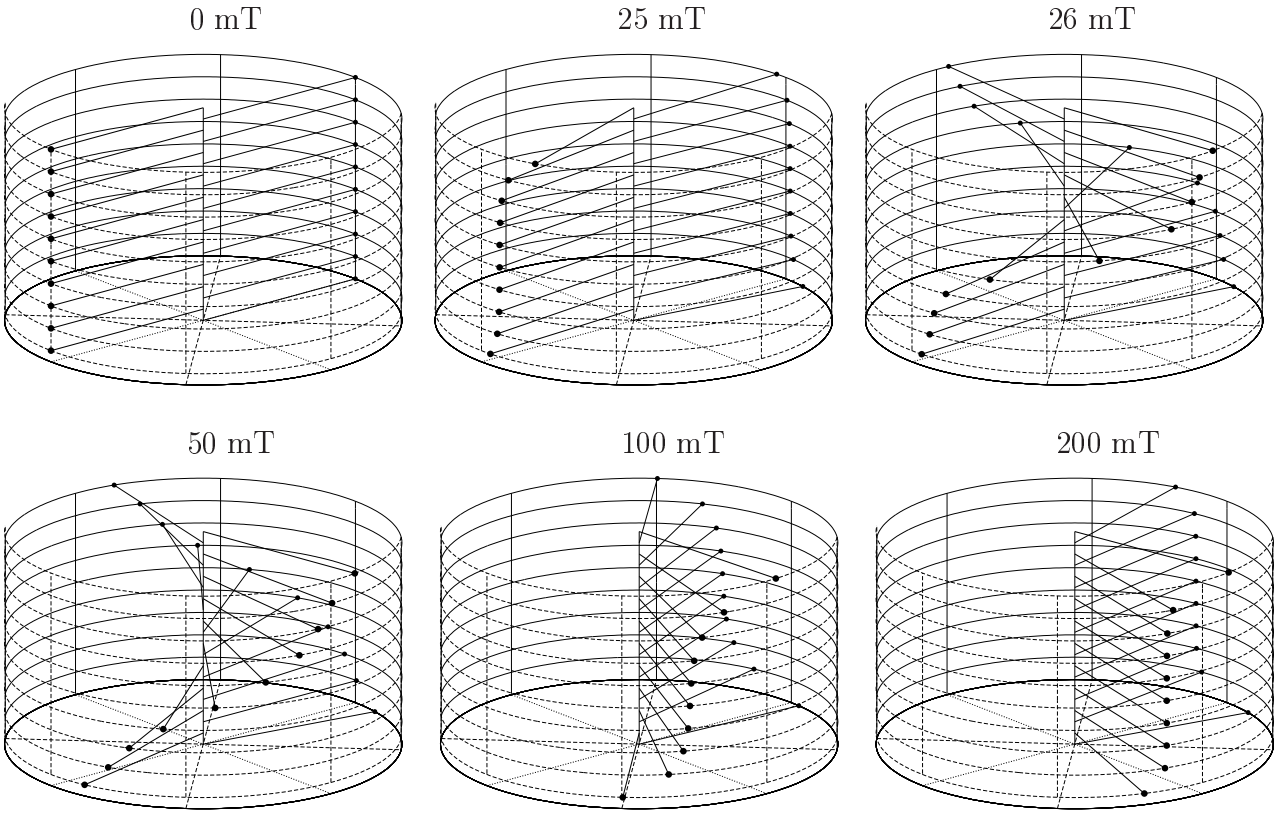

Figure 3.9: Numerical simulation by global energy minimization. The external field is parallel to the hard axis. Increasing the field from zero the first strictly AF alignment cants smoothly up to 25 mT, then a phase transition occurs, and from 26 mT the stack is divided to two subparts, each retaining the AF alignment, but orthogonal to each other. The central layers act as a 'domain wall' rotating from one part to the other. When the field is further increased this X structure smoothly transforms to a $<$ as the Zeeman energy compared to the anisotropy and exchange terms gets larger and larger.

Chapter 4

Measurements in momentum space

In the previous chapters we dealt with 'direct space' measuring methods. In the following we will introduce techniques that are working in the momentum space. For the investigation of AF coupled MLs it is often favorable to 'dress up' the ML structure with the magnetic information. After the introduction to Synchrotron Mössbauer Reflectometry (SMR) and Polarized Neutron Reflectometry (PNR) we briefly review the momentum-space representation, and finally a short part is devoted to coherence issues, which may be important for magnetic domain measurements.

4.1 SMR

Nuclear resonant scattering of synchrotron radiation (NRS of SR) [51], also referred to as Synchrotron Mössbauer reflectometry (SMR) [52], is a powerful method for analyzing hyperfine fields and thus magnetization of thin films and MLs containing nuclear resonant isotopes. In SMR measurement the illuminated sample scatters the radiation coherently, which can make evaluation of the measured curves a hard task. Without the knowledge of the underlying structure (layer thicknesses, hyperfine fields, etc.) it is not possible to get a reliable picture. For homogenous thin films the determination of the layer parameters may be easy. In the case of Fe/Cr MLs, however, the number of parameters to be fitted (hyperfine structure of the interface regions, the structural roughness, etc.) may prohibit the correct evaluation.

One could ask, what are the benefits of SMR in such a complex system compared to 'classical' magnetization measurements (like MOKE or VSM)? The answer lies in the coherent nature of SMR. As it can distinguish different regions in the reciprocal space, it may show direct evidence of magnetic structures, separate magnetic correlations (domains) from structural roughness.[1] SMR is also good in mapping patch-domains of AF-coupled MLs.

[1] In fact, the 'coherence-related' statements are also true for polarized neutron scattering.

4.1.1 Introduction to SMR and PNR

Total external reflection (TER) of x-rays [53, 54] and neutrons [55] from flat surfaces are phenomena dating back to the first half of the twentieth century. The real part of the index of refraction n of most materials for thermal neutrons and of all materials for non-resonant x-rays is by about 10^{-5} less than unity. At low enough angles of grazing incidence $\theta < \theta_c = \sqrt{2\,(1-n)}$ the waves are totally reflected. The intensity of the reflected specular beam for $\theta > \theta_c$ rapidly decreases with increasing wave vector transfer $q = 2k \sin\theta$ where k is the length of the wave vector of the incident radiation. In a stratified medium, reflected and refracted beams appear at each interface. The interference of the reflected beams leads to patterns of the reflectivity vs. wave vector transfer spectrum $R(q)$ that bear information on the depth profile of the index of refraction $n(z)$, the argument z being the coordinate perpendicular to the sample surface. $R(q)$ can be calculated from $n(z)$, e.g. using the method of characteristic matrices [56, p. 51]. Therefore, in frames of a given model for the stratified system, $n(z)$ can be reconstructed from $R(q) = |r(q)|^2$ where $r(q)$ is the reflectivity amplitude. This latter approach is the basic idea of specular x-ray and neutron reflectometry, two methods that can be used for mapping the electron density and the isotopic/magnetic structure of thin films, respectively.

The coherent forward scattering of a scalar wave of momentum much higher than that of the scatterers can be described [57] by the index of refraction close to unity

$$n = 1 + \frac{2\pi N}{k^2} f \tag{4.1}$$

where N is the density of scatterers and f is the scattering amplitude. The electron density for non-resonant x-rays or nuclear and magnetic scattering length density for neutrons is implied in the latter quantity [58].

X-ray reflectometry may optionally be performed with nuclear resonant photons. We shall call this technique, henceforth, Mössbauer reflectometry (MR). MR benefits from the fact that, close to the nuclear resonance, the photon scattering amplitude f is strongly energy-dependent and contains the matrix elements of the hyperfine interactions. MR is therefore suitable to study the magnetic structure of thin films.

A serious limitation of MR with conventional sources [59] is the small (10^{-5}) solid angle involved. Due to its high collimation, synchrotron radiation (SR) is much better suited for reflectometric experiments than radioactive sources. Synchrotron Mössbauer reflectometry (SMR) is the application of grazing incidence nuclear resonant scattering of SR [60] to thin film and ML structure analysis.

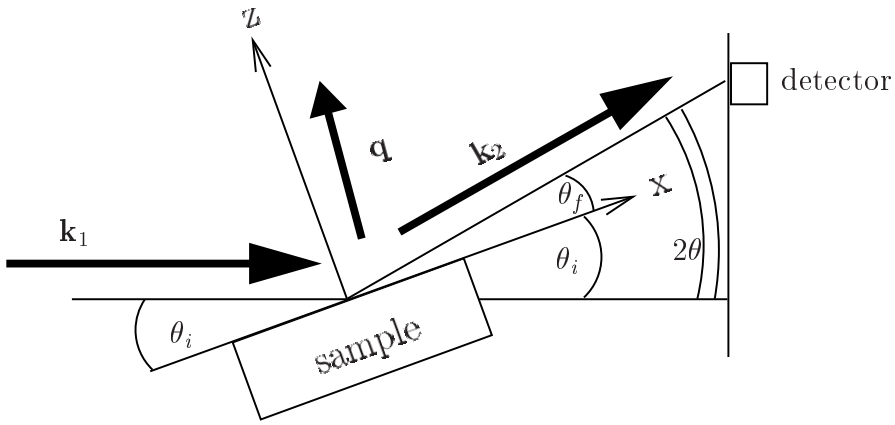

Figure 4.1: Schematic drawing of the measurement setup. The incoming beam $\mathbf{k}_1$ is scattered on the sample to $\mathbf{k}_2$. The scattering is described by angle 2θ in the lab system. In sample coordinates with axes x and z the scattering is described by angles θ_i and θ_f. In the figure the angles are unrealistically large for demonstration purposes ($\theta_i = 20°$, $\theta_f = 10°$). The figure shows an off-specular case ($\theta_i \neq \theta_f$), thus $\mathbf{q}$ in not parallel to z.

4.1.2 SMR measurements

The sketch of the experimental arrangement of an SMR experiment is shown in Fig. 4.1. The photons from the high-resolution monochromator (not shown) hit the sample mounted on a two-circle goniometer of adjustable height at an angle of grazing incidence θ_i. The reflected (scattered) photons are detected by an avalanche photo diode (APD). The detector position defines the scattering angle 2θ. The angle θ_i is often referred to as ω.

An SMR measurement is performed in either time integral or time differential regime. Time integral SMR (TISMR) records the total number of delayed photons from t_1 to t_2 as a function of θ_i and/or 2θ (for details see below). Here t_1 is a few nanoseconds determined by the bunch quality of the radiation source and by the dead time of the detector and the electronics, while t_2 is set to a value somewhat below the bunch repetition time of the storage ring. Time differential (TD) SMR is a time response measurement performed at various fixed values of θ_i and 2θ. Like in the forward scattering case [61], hyperfine interaction results in quantum beats of the time response. Finally we note that with TISMR spectra usually the 'prompt' spectra are also taken. The prompt tag refers to the non-resonant x-ray scattering.

In a $\theta - 2\theta$ experiment the wave vector transfer $\mathbf{q}$ is perpendicular to the sample surface. For a periodic ML, in the first Born approximation (kinematic theory), Bragg maxima appear at $q = \sqrt{(2\pi/d)^2 + q_c^2}$, where d is the structural or hyperfine (magnetic) period length perpendicular to the film plane and q_c is the critical wave vector transfer of the TER (typically about 0.5 nm^{-1}). Thus a $\theta - 2\theta$ scan reveals the *average* plane-perpendicular structure of the ML. In-plane inhomogeneities reduce the specular reflection. Lateral dimensions of inhomogeneities such as structural and magnetic roughness, waviness, magnetic domains, etc., however, cannot be further studied in a $\theta - 2\theta$ experiment.

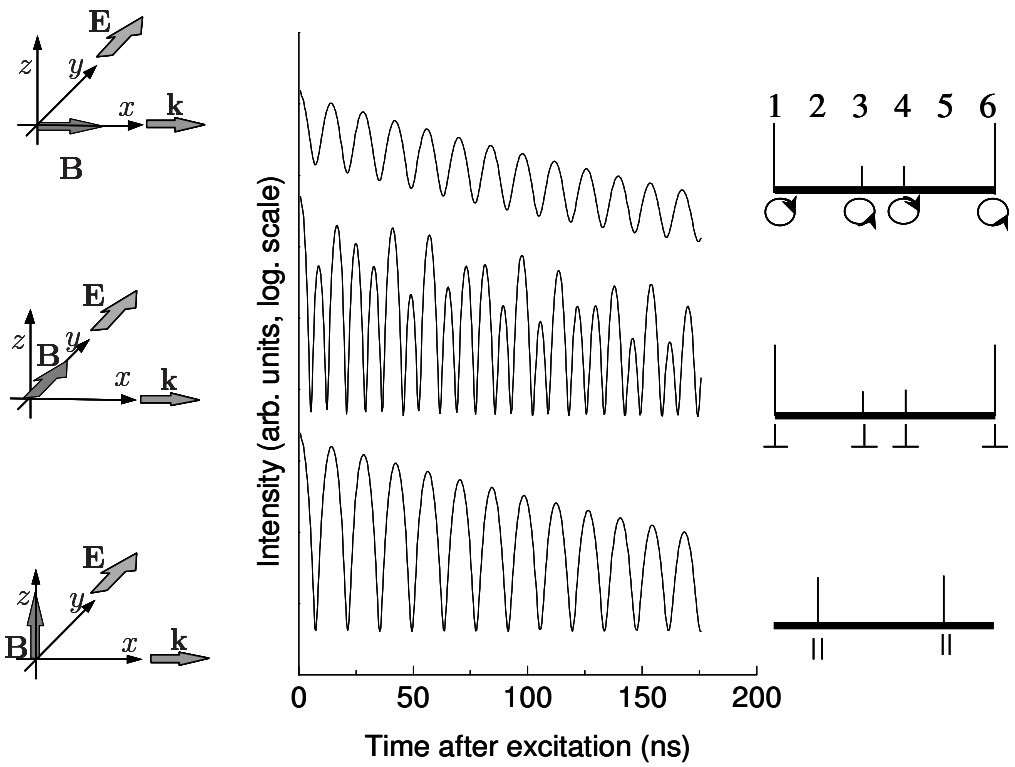

Figure 4.2: Calculated TDSMR of a thin Fe foil magnetized in different directions (**B**). In the right column the polarizations of the hyperfine transitions are sketched (for details see text), after [61].

In an ω-scan experiment for small q values the perpendicular-to-plane component of the wave vector transfer is constant ($q_z = 2k\theta$) while varying θ_i, the in-plane parallel-to-beam component of the wave vector transfer is scanned: $q_x = 2k\theta(\theta_i - \theta)$. The different scan types will be detailed in Sec. 4.3. In order to have significant intensity, the detector height is set to q_z of a Bragg peak. In the first Born approximation, the width of the ω-scan (i.e., q_x scan) is inversely proportional to the longitudinal correlation length

$$\xi = \frac{2\pi}{\Delta q_x} \tag{4.2}$$

where Δq_x is the width of the q_x scan (excluding the specular scattering). ξ is the correlation length of the quantity the perpendicular-to-plane periodicity of which the Bragg peak is due to. Therefore, setting 2θ in an ω-scan experiment to an electronically forbidden pure nuclear reflection the lateral correlation length of inhomogeneities of the hyperfine interaction (magnetic roughness, magnetic domains) can be determined.

4.1.3 Magnetic information

Due to the full linear polarization, nuclear resonant scattering of SR is extremely sensitive to the direction of the hyperfine magnetic field [61, 64], see Fig. 4.2. The same holds true for

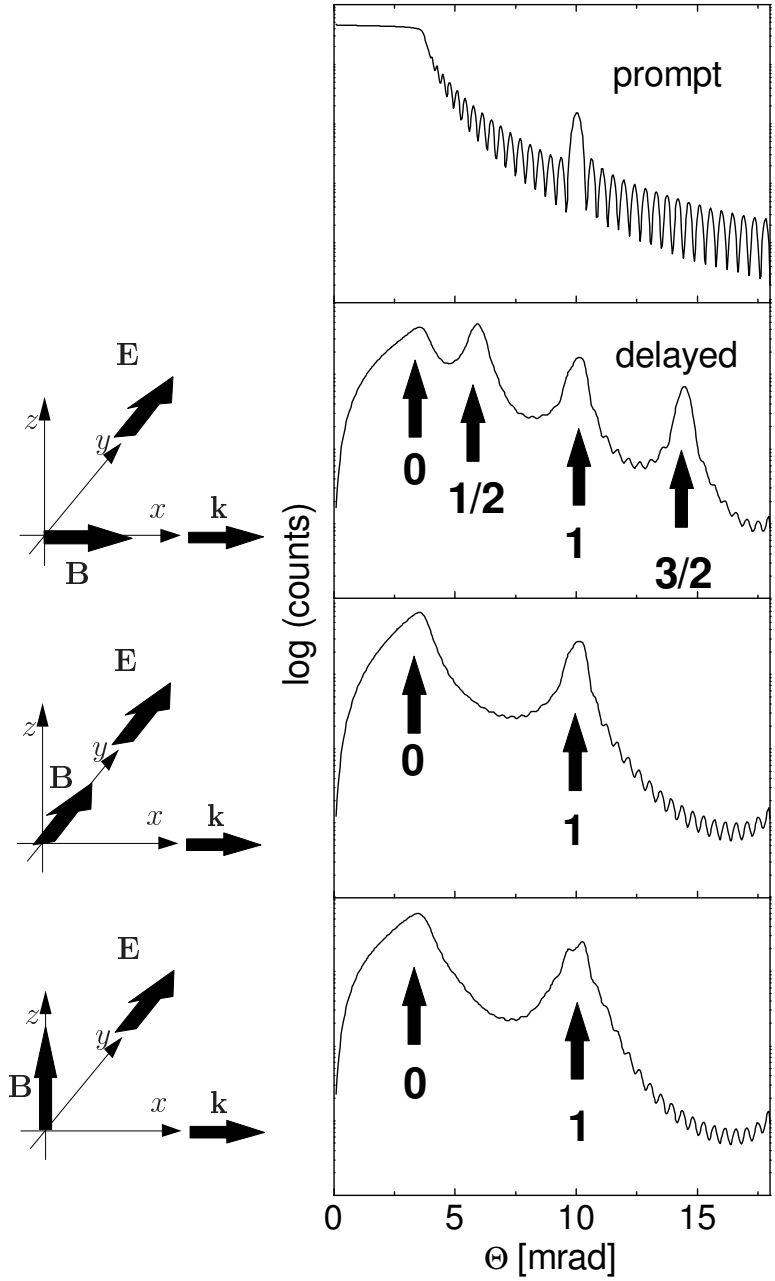

Figure 4.3: "Calculated $\theta - 2\theta$ scans of an AF-coupled $\left[^{57}\mathrm{Fe}\,(20\ \text{Å})\,/\mathrm{Cr}\,(26.2\ \text{Å})\right]_{20}$ ML for three different directions of the hyperfine field **B** (the hyperfine field of the other sublattice is not shown). The scattering plane is perpendicular to the electric field vector **E** of the SR. The arrows indicate the Bragg reflections of different order." [62]

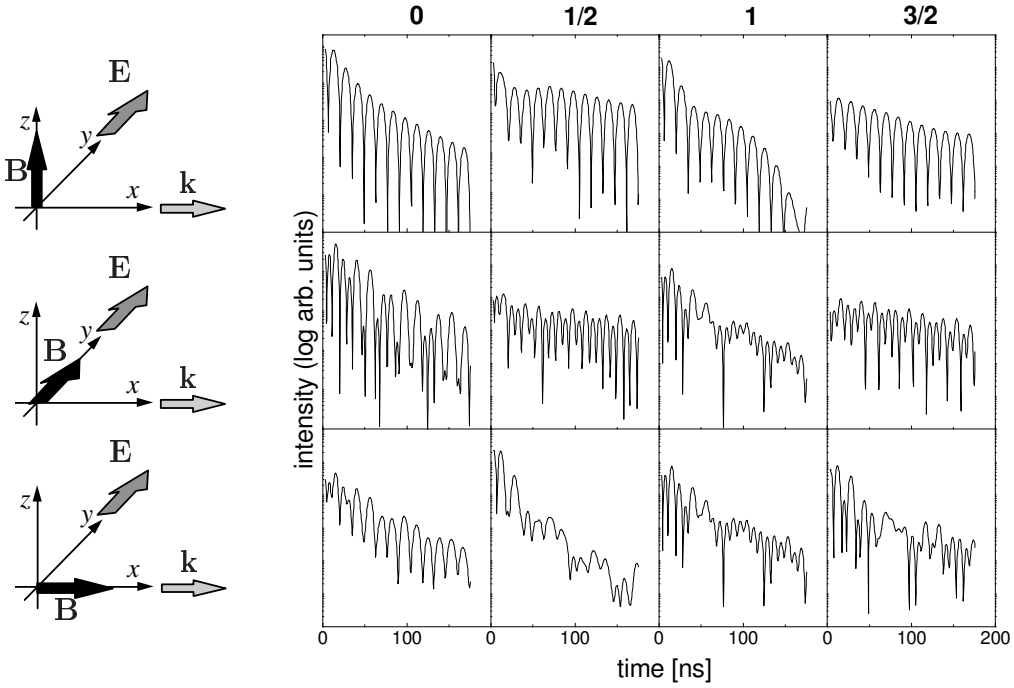

Figure 4.4: "Calculated time response curves of an AF-coupled $\left[^{57}\mathrm{Fe}\left(20\ \text{Å}\right)/\mathrm{Cr}\left(26.2\ \text{Å}\right)\right]_{20}$ ML for three different directions of the hyperfine field **B** (the hyperfine field of one of the two sublattices is not shown). The scattering plane is perpendicular to the electric field vector **E** of the SR. Integer and half-integer numbers indicate the order of the structural and hyperfine (magnetic) Bragg reflections, respectively." [63]

the grazing incidence geometry [51]. Both TISMR and TDSMR can be used to determine the layer magnetization direction in thin films and MLs. Figs. 4.3 and 4.4 show calculated $\theta - 2\theta$ scans and time response curves of an AF-coupled $\left[^{57}\mathrm{Fe}\left(20\ \text{Å}\right)/\mathrm{Cr}\left(26.2\ \text{Å}\right)\right]_{20}$ ML (the scattering plane is perpendicular to the electric field vector of the SR). The magnetic structure of the ML is supposed to be collinear so that the directions of the hyperfine field **B** alternate across consecutive Cr layers. The total reflection peak ('0th order Bragg reflection') and the structural Bragg peak ('1st order Bragg reflection') show up in the time integral scans at the same value of θ as in the prompt scan. If **B** is (anti)parallel to the wave vector **k** of the SR, AF super-reflections ('1/2th and 3/2th order Bragg reflections') can be observed which are missing if **B** is perpendicular to **k**. In fact, the photon scattering amplitude f only depends on the angle of **k** and **B** and so no AF cell doubling for f is possible if $\mathbf{k} \perp \mathbf{B}$. This is how time integral SMR can characterize the orientation of the AF ordered lattice magnetization. The shape of the time response curves strongly depends on θ. This is due to the fact that the phases of the waves scattered at different depth are shifted with respect to each other depending on θ. The shape of the time response curves is most sensitive to the direction of **B** at the AF (half integer order) reflections. The way to thin film magnetic structure analysis with SMR has been opened by Toellner *et al.* who demonstrated the existence of pure nuclear reflections in an Fe/Cr ML [65].

It is interesting to note that the quantum-beat patterns at the structural Bragg peak of the AF aligned ML, belonging to magnetization directions parallel to the beam or parallel to the polarization of SR are identical (see Fig. 4.4). This independency of the orientation of **B** can be easily understood in analogy with the forward direction case. For a single domain of ferromagnetic Fe film the the stick diagrams in the right column of Fig. 4.2 show the polarization of the hyperfine-split lines. For an AF-aligned ML, if the hyperfine magnetic field is parallel to the beam for one sublattice, it is antiparallel for the other. Therefore left and right circular polarized transitions appear at the same energy for the one and the other sublattice, respectively. Consequently, all transitions can interfere with each other, which results in the same quantum-beat pattern as if the hyperfine field is parallel to the polarization of the SR. In this latter case all transition remain σ-polarized for an AF-aligned ML so that no change is expected as compared to case of a ferromagnet shown in the right-hand side of Fig. 4.2. The same magnetic configuration and thus same TDSMR spectrum is obtained in the case of ML with parallel magnetization (in saturation for example) parallel to the polarization of the SR. For an AF aligned ML not only the quantum-beat patterns for in-plane magnetization parallel and perpendicular to the beam but for any in-plane direction of the magnetization are identical [63]. In transversal sample setup (when the direction of the applied external field **H** is perpendicular to **k**) even at intermediate fields, when the ML is in the <-state, the spectra at structural Bragg positions will be almost the same, as model calculations with EFFI revealed.

4.2 PNR

Neutron scattering is also sensible to the local magnetic field. Polarized neutron scattering (PNR) became a routine measurement technique for characterization of films and MLs [66–70]. We define the scattering geometry similarly to the SMR case (see Fig. 4.1). In the case of our investigations even the de Broglie wavelength of the neutrons and the wavelength of the nuclear-resonant γ-rays were in the same range ($\lambda_n \approx 1 - 2$ Å, while for 14.4 keV $\lambda_\gamma = 0.86$ Å).

The PNR measurements described in this work were carried out in JINR, Dubna at the REMUR reflectometer [71]. In that particular setup the polarized neutrons are guided by a small magnetic field from the polarizator till the detector. The spin state relative to quantization axis defined by the applied field can be changed by spin-flippers. In the reflectometry experiment the neutron beam is polarized by supermirrors. The initial spin-state is set by the first spin flipper. The second flipper is located after the sample. External magnetic field may be applied to the sample. After the second flipper the neutrons reach the analyzer, which is a fan shaped supermirror and lets trough the neutrons of one polarization to the detector. The reflectivity spectra are taken in four channels, two non-spin-flip ($++$ and $R--$) and two spin-flip ($+-$ and $-+$). The signs refer to the initial and final spin-state. The above described spin analysis allows to see the spins of different orientations in one single measurement. Indeed, if

the scattering spins are parallel to the neutron spin, then it gives contrast in the non-spin-flip reflectivity (R^{++} and R^{--}), while for perpendicular alignment spin-flip scattering occurs (R^{+-} and R^{-+}) (see Fig. 4.5). Note that on the figure the external field $\mathbf{H}$ is parallel to $\mathbf{k}$, while at REMUR $\mathbf{H} \perp \mathbf{k}$ setup was used.

4.3 Momentum-space representation

The aim of the $Q-$space measurements is to gain information on the lateral and plane-perpendicular structure of the ML. With elastic neutron and $\gamma-$photon scattering we are probing the sample in the momentum or reciprocal space, hereafter called Q-space. In time-of-flight (TOF) neutron measurements we are counting particles in the $\lambda - 2\theta$ coordinates, while in SMR measurements we are measuring the so-called $\theta - \omega$ or $\theta - 2\theta$ curves. Both of those measurements can be mapped to $q_x - q_z$ coordinates for comparison. In principle with scans along the q_z-axis the structural and magnetic depth profile, while with q_x scans at constant q_z the lateral correlations of the ML can be investigated.

4.3.1 Measurements is $Q-$space

We will describe the scattering in lab coordinate system first (see Fig. 4.1). In the lab system the incoming beam is fixed and the sample and the detector is moved. Let us denote $\mathbf{k}_1$ the incoming and $\mathbf{k}_2$ the deflected wave vector. For elastic scattering $|\mathbf{k}_1| = |\mathbf{k}_2| = k = 2\pi/\lambda$, where λ is the wavelength of the radiation.[2] If we define the angle between $\mathbf{k}_1$ and $\mathbf{k}_2$ as 2θ then the length of the scattering vector will be $q = |\mathbf{q}| = |\mathbf{k}_2 - \mathbf{k}_1| = 4\pi/\lambda \sin\theta$. From the above it is trivial that for fixed wavelength the length of the scattering vector $\mathbf{q}$ depends only on the scattering angle 2θ. However, The orientation of $\mathbf{q}$ relative to the sample will depend on the angle of the sample. We have to keep this in mind when describing the scattering in sample coordinate system.

4.3.2 Sample coordinate system

In general scattering geometry in sample coordinate system the impinging and reflected beams can be described by angles θ_i and θ_f measured from the sample surface (see Fig. 4.1). The equation $\theta_i + \theta_f = 2\theta$ connects this description with the lab system one. It is easy to see that for wave vector $|k| = 2\pi/\lambda$ the momentum transfer in sample coordinate system will be [67]:

$$q_x = \frac{2\pi}{\lambda}\left(\cos\theta_f - \cos\theta_i\right), \quad q_z = \frac{2\pi}{\lambda}\left(\sin\theta_f + \sin\theta_i\right). \tag{4.3}$$

[2] Or the de Broglie wavelength of the neutron.

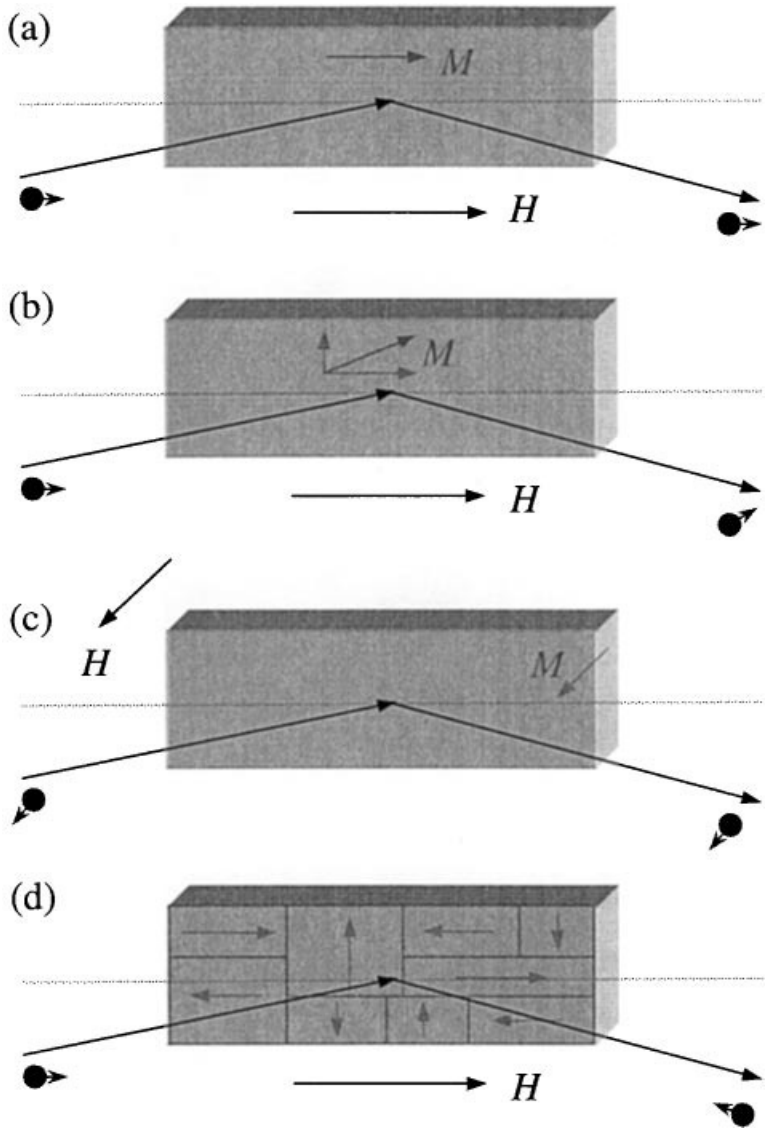

Figure 4.5: "The orientation and magnitude of the sample magnetization $M(z)$ relative to the applied field H determines the relative proportions of spin-flip (SF) and non-spin-flip (NSF) scattering. (a) $M(z)$ in the plane of the surface, parallel to H produces no SF scattering, but creates different spin-dependent refractive indices for neutrons polarized parallel and anti-parallel to H. (b) $M(z)$ canted at an arbitrary angle in the surface plane produces both SF and NSF intensity. (c) $M(z)$ components normal to the surface have no effect on neutron specular intensity. (d) The presence of domains complicates interpretation of SF and NSF intensities. Off-specular methods offer a means of characterizing these domains." [69] Note that the figure shows the experiment in 'top view', while on Fig. 4.1 we see the side view of the same setup.

4.3.3 PNR and Q-space

In the case of TOF PNR we collect counts in a two dimensional grid of time ($\propto \lambda$) and displacement ($\propto 2\theta$). The measurement is made at constant θ_i. To get the actual transformation rules, we have to substitute $\theta_f = 2\theta - \theta_i$ to (4.3):

$$q_x = \frac{2\pi}{\lambda}\left(\cos\left(2\theta - \theta_i\right) - \cos\theta_i\right), \tag{4.4a}$$

$$q_z = \frac{2\pi}{\lambda}\left(\sin\left(2\theta - \theta_i\right) + \sin\theta_i\right). \tag{4.4b}$$

Inverse transformation for TOF measurements

In order to evaluate TOF measurements it is useful to calculate the inverse transformation of (4.4). The reason is obvious. To be able to integrate or to average data easily in $Q-$space, an equidistant grid is useful. To get this grid, the inverse transformation should be applied to the $Q-$grid and data shall be averaged in the (λ, θ) system according to this grid. Then, the averaged data can be transformed back to the proper grid and data manipulation and representation is easily done. It is not difficult to show that the inverse transformation of (4.4) will be:

$$\delta = -2\arctan\frac{q_x}{q_z}, \tag{4.5a}$$

$$\lambda = \frac{4\pi}{\sqrt{q_z^2 + q_x^2}}\sin\left(\theta_i - \arctan\frac{q_x}{q_z}\right) = \frac{4\pi}{\sqrt{q_z^2 + q_x^2}}\sin\left(\theta_i + \frac{\delta}{2}\right). \tag{4.5b}$$

Here $\delta = \theta_f - \theta_i$ i.e. the angle measured from the specular reflection ($\theta_f = \theta_i$). When $q_x \ll q_z$, then (4.5) can be approximated as:

$$\delta \approx -2\frac{q_x}{q_z}, \tag{4.6a}$$

$$\lambda \approx \frac{4\pi}{q_z}\left(\theta_i + \frac{\delta}{2}\right). \tag{4.6b}$$

From (4.6b) we can get $\delta(\lambda) = q_z\lambda/(2\pi) - 2\theta_i$. For constant q_z this is a straight line in the (λ, δ) space with the slope

$$m = q_z/(2\pi). \tag{4.7}$$

The above-described equations can be used to determine the $Q-$scale of the measurement. If the position of the direct beam on the angular scale of the position sensitive detector (PDS) is known compared to the specular reflection, then no more data are needed for the absolute calibration of q (θ_i is known from $2\theta_{\text{spec}} = 2\theta_i$ and from (4.4b) $q_z = q$ can be also calculated).

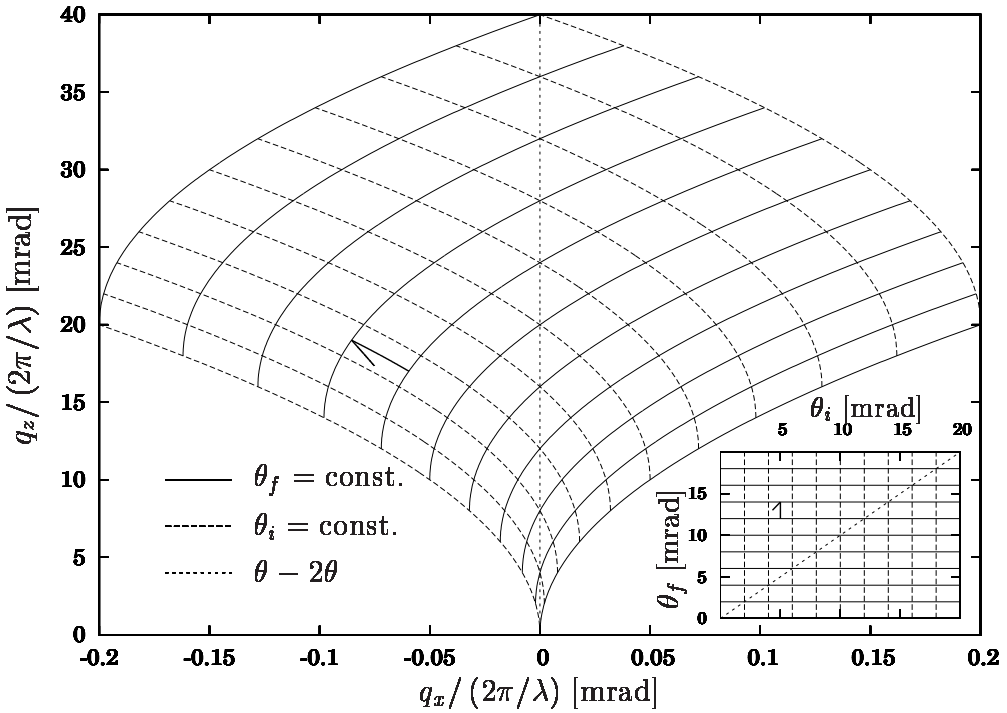

Figure 4.6: $\theta_i - \theta_f$ scan in the Q-space. The q units are normalized to $2\pi/\lambda$. In the inset the original grid of constant θ_i and θ_f values is shown. The calculated range is similar to the one used for the measurements of this work. The pattern '1' helps to see the orientation of the transformation. The specular line, i.e. the $\theta - 2\theta$ scan ($\theta_i = \theta_f$) is also shown.

In the case of no direct beam information the q scale can be still figured out. If we know q_z for a given Bragg reflection, then again $\theta_i = q_z\lambda/4\pi$. And finally by fitting the slope (4.7) of a Bragg sheet[3] yields the q_z of the Bragg sheet, with no need of knowledge of the sample structure. When q_z is known, then for the specular ($\delta = 0$) channel $\theta_i = q_z\lambda/4\pi$.

$\theta_i - \theta_f$ scan

Neutron scans are also taken with monochromatic beam (see [72] for example). In this case the wavelength is fixed and the sample and detector are rotated. The resulting mapping is shown in Fig. 4.6.

4.3.4 SMR and Q-space

In the following we will show the different scan modes, which can be used in x-ray reflectometry experiments. In fact, due to the known $(\theta_i, \theta_f) \rightarrow (q_x, q_z)$ transformation (4.3) for any angle pairs we may get the mapping in the Q-space. Nevertheless, it seems reasonable to plot the transformation for the different scan modes separately.

We note that the SMR measurements were taken with horizontal sample arrangement, i.e. the sample reflected the horizontal beam in the vertical plane. Lacking appropriate 1D

[3] After weighting to the direct beam profile and subtracting the background.

avalanche photodiode (APD) arrays, in contrast to the — already two dimensional — neutron measurements, so far at all SMR experiments have been performed by scanning along a 1D curve in the Q-space.In the following we will outline the scan modes and will discuss the possible curves in case of systematic errors (detector offset, sample zero angle offset and 'open' slits).

$\theta - 2\theta$ scans

The most 'traditional' scan type is the $\theta - 2\theta$ scan. In this case $\theta_i = \theta$, $\theta_f = \theta$ and we scan[4] angle θ. It is easy to see that in this case (4.3) becomes:

$$q_x = 0, \quad q_z = \frac{4\pi}{\lambda} \sin\theta \approx \frac{4\pi}{\lambda}\theta. \tag{4.8}$$

The approximation $\sin\theta \approx \theta$ is valid in our case, because θ is typically not exceeding 1°. The $\theta - 2\theta$ scan is specular ($q_x = 0$), probing the vertical structure of the ML. The $\theta - 2\theta$ scan is conventionally done with wide detector slits [73] (integral measurement mode). In this case we 'cut' the reciprocal space normal to the surface. If the detector slit is narrowed, then only the real specular range is included.

Off-specular or ω scans

In the ω scan the position of the source and detector is fixed thus $\theta_i + \theta_f = 2\theta = const.$ It is best to introduce ω by $\omega = (\theta_i + \theta_f)/2$ thus $\theta_i = \theta + \omega$, $\theta_f = \theta - \omega$. This is equivalent to the rocking by ω from the specular $\theta_i = \theta_f = \theta$ position. The equations now are:

$$q_x = \frac{2\pi}{\lambda} \left(\cos(\theta - \omega) - \cos(\theta + \omega)\right) = \frac{4\pi}{\lambda} \sin\theta \sin\omega \approx \frac{4\pi}{\lambda}\theta\omega, \tag{4.9a}$$

$$q_z = \frac{2\pi}{\lambda} \left(\sin(\theta - \omega) + \sin(\theta + \omega)\right) = \frac{4\pi}{\lambda} \sin\theta \cos\omega \approx \frac{4\pi}{\lambda}\theta. \tag{4.9b}$$

In general case the ω scans are spheres with radius $(4\pi/\lambda)\sin\theta$ but in our special small angle limit, the scan will be a perpendicular line to q_z (Fig. 4.7). Thus we probe the diffuse (off-specular) scattering of the sample. In other words, we are mapping the lateral structures. The ω scans are always taken with narrow slits. We emphasize again: to move along the θ axis in the lab system, one should rotate the sample by θ while the detector should be moved by 2θ. For movement along the ω axis, the detector should stay in-place, while the sample should be rotated around the θ axis (rocking curve).

Note that in an SMR ω scan the actual value of ω is measured from the beam position. Thus in a 'real scan' the scanned coordinates in the lab system are: ω and 2θ which can be transformed to sample coordinates in the following way: $\theta_i = \omega$ and $\theta_f = 2\theta - \omega$. This

[4]Then name originates form the fact that in a fixed-beam setup the detector should be moved 2θ when the sample is rotated by θ.

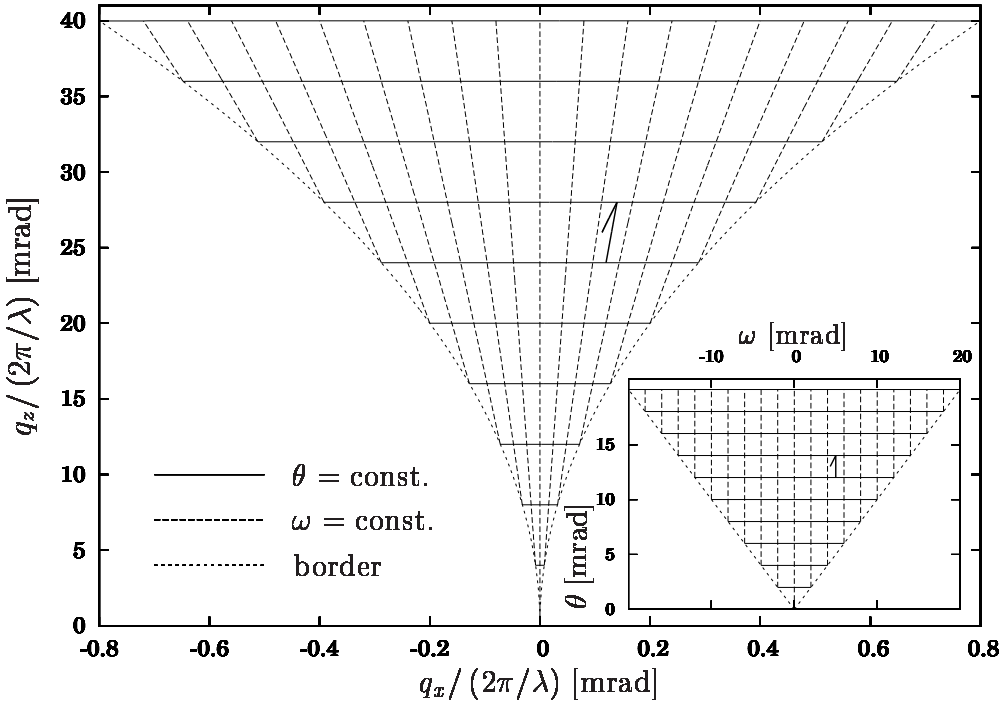

Figure 4.7: $\omega - 2\theta$ scan family in symmetric sample coordinates. In this case $\theta_i = \theta + \omega$, $\theta_f = \theta - \omega$. The inset with the pattern '1' shows the original coordinates fulfilling the conditions $\theta_i \geq 0$, $\theta_f \geq 0$.

difference has consequences for an ω scan with a 1D detector array as it can be seen in Fig. 4.8. The constant ω curves are no straight lines anymore.

Longitudinal off-specular or offset $\theta - 2\theta$ scan

The offset $\theta - 2\theta$ scan (or longitudinal off-specular scan) also provides information about the off-specular range. This is a $\theta - 2\theta$ scan with slightly misaligned sample or detector. The misalignment should be big enough not to include the specular ($q_x = 0$) ridge [74]. First, we investigate the sample misalignment. Let us denote the misalignment angle with δ, thus $\theta_i = \theta + \delta$, $\theta_f = \theta - \delta$. It is easy to see that this regime is similar to the ω scan except that now δ is fixed and θ is scanned. The $\theta - 2\theta$ scan is a special case of this type of scan ($\delta = 0$). For $\delta \neq 0$ the scanned curve is a line, starting from the $(0, 0)$ point. The slope of the line is $1/\delta$. The $\theta - 2\theta$, ω and offset $\theta - 2\theta$ scans belong to one branch, called $\omega - 2\theta$, describing the system in the reciprocal space according to the mapping presented in Fig. 4.7.

In the second case, the detector has a fixed offset of δ i.e., in sample coordinates: $\theta_i = \theta$, $\theta_f = \theta + \delta$. In this case

$$q_x = \frac{2\pi}{\lambda}\left(\cos\left(\theta + \delta\right) - \cos\theta\right), \quad q_z = \frac{2\pi}{\lambda}\left(\sin\left(\theta + \delta\right) + \sin\theta\right). \tag{4.10}$$

When taking the $\theta - 2\theta$ scan in integral mode (wide detector slits) it is equivalent to integrating in the momentum space in the $\pm\delta$ range. As can be seen from Fig. 4.9, the

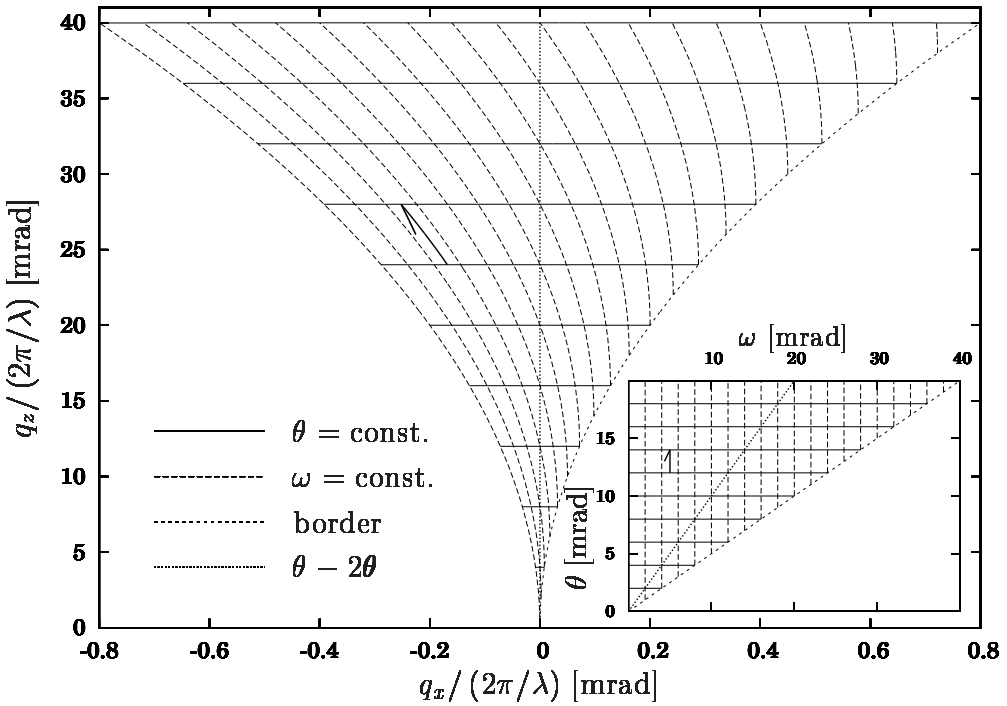

Figure 4.8: The normalized plot of the $\omega-$scan in lab coordinates ($\theta_i = \omega$, $\theta_f = 2\theta - \omega$). The inset with the pattern '1' shows the original coordinates fulfilling the conditions $\theta_i \geq 0$, $\theta_f \geq 0$. The specular line ($\theta - 2\theta$) is shown for comparison with the symmetric sample coordinate system (see Fig. 4.7).

integration region is not perpendicular to q_z.

The above-described scans may be used to evaluate the plane-perpendicular correlation of the lateral roughness. For uncorrelated roughness the diffuse scattering occurs in the whole Q-space, while for correlated roughness it is concentrated along Bragg-sheets [74]. One method to investigate the diffuse scattering is the offset $\theta - 2\theta$ scan while a constant q_z line can be scanned by ω scans. By scanning different regions of the Q-space information on the correlated roughness (structural or magnetic) can be deduced after correcting the measurements for geometrical factors. The details will be presented at the sample evaluation.

Detector scan

The detector scan regime has been rarely used by us. It becomes important with the introduction of the 1D detector array. This is in fact similar to the longitudinal off-specular scan, but in this case the detector is moved, thus θ is fixed and δ is the variable. Fig. 4.9 shows the two latter scan types.

4.3.5 The q_y component

Up to now we looked only at scattering in the $q_x - q_z$ plane. However, of- specular scattering may occur in the q_y direction as well [68]. To treat the whole $Q-$space we will rewrite (4.3) to

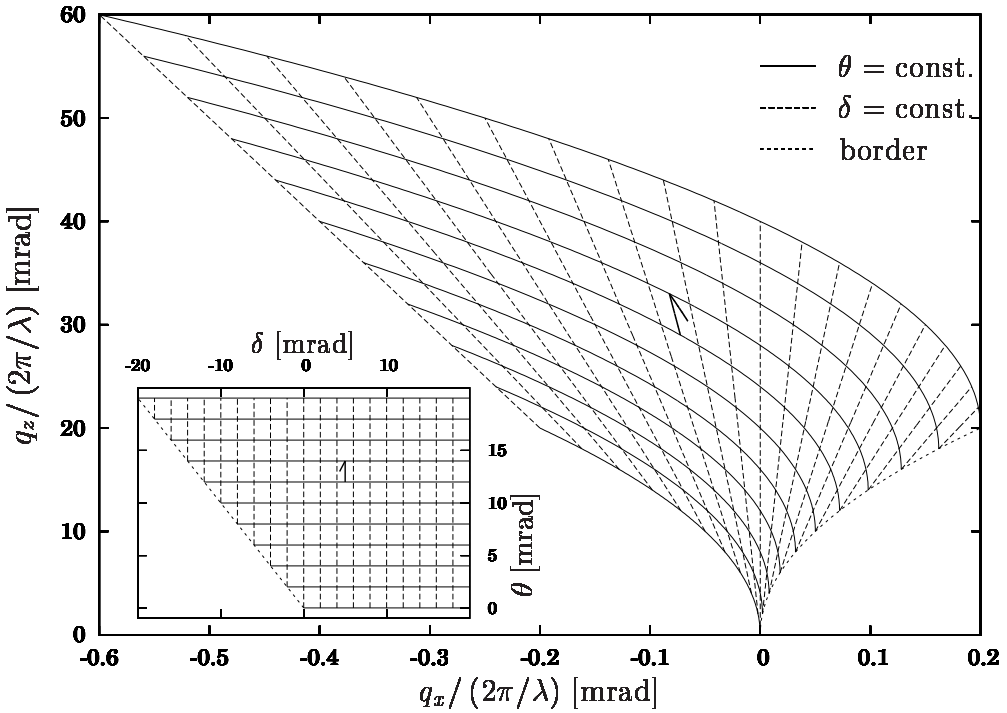

Figure 4.9: The $Q-$space plot of the longitudinal scans. $\theta_i = \theta$, $\theta_f = \theta + \delta$. The inset with the pattern '1' shows the original coordinates fulfilling the conditions $\theta_i \geq 0$, $\theta_f \geq 0$. When taking $\theta - 2\theta$ scans with slit width Δ, then we integrate from $\theta_f = \theta - \Delta$ to $\theta + \Delta$. This symmetric range will be converted to an asymmetric one in $q_x - q_z$ coordinates.

contain the q_y component:

$$q_x = \frac{2\pi}{\lambda}\left(\cos\theta_f \cos\varphi - \cos\theta_i\right), \tag{4.11a}$$

$$q_y = \frac{2\pi}{\lambda}\cos\theta_f \sin\varphi, \tag{4.11b}$$

$$q_z = \frac{2\pi}{\lambda}\left(\sin\theta_f + \sin\theta_i\right). \tag{4.11c}$$

The new angle φ is the azimuthal angle of $\mathbf{k}_2$ or the angle off the reflection plane [68]. It follows from (4.11c) that q_z is not affected by φ. In the case of synchrotron measurements the detector is not position sensitive and the horizontal slit is in the order of millimetres, thus we integrate a huge region in q_y. Let us write the angles in symmetrical sample coordinates:

$$q_x = \frac{2\pi}{\lambda}\left(\cos\left(\theta - \omega\right)\cos\varphi - \cos\left(\theta + \omega\right)\right) \approx \frac{4\pi}{\lambda}\theta\omega, \tag{4.12a}$$

$$q_y = \frac{2\pi}{\lambda}\cos\left(\theta - \omega\right)\sin\varphi \approx \frac{2\pi}{\lambda}\varphi. \tag{4.12b}$$

The above approximations are valid in the range of φ used at synchrotron measurements. For example: a 4 mm wide slit placed at ≈ 75 cm corresponds to $\pm 0.15^\circ$ (2.7 mrad). In q_x and q_z scans we use the vertical component of $\mathbf{q}$, while for q_y scans the horizontal component counts. This is the reason of the missing θ proportionality factor. In other words, $2\theta\omega = \varphi$. Because θ

is in the range of 0.5°, to scan the same range in q_y as in q_x a much smaller φ angle (resolution) should be applied. Or otherwise, we integrate to the full q_y range in our measurements. To see the possible feasibility of a 2D detector, let us calculate the necessary resolution for a q_y scan at the AF Bragg position (0.4°) of sample 990608. We know that a vertical slit[5] height of 0.1 mm ($\rightarrow$ 66 μrad) gave satisfactory resolution in q_x. For the same resolution we need 90 nrad $\rightarrow$ 1.36 μm horizontal slit setting in this case.

We can draw the conclusion that we integrate to q_y in all $\omega-$scans. Also, if we would not approximate but evaluate (4.12) as it is, then we would see that for a constant θ and ω if we scan φ, then we are moving along a circular path in the $q_x - q_y$ plane. But this would be relevant only for higher q_y values, where the scattering is already negligible.

The integration in reciprocal space from zero to high values means an integration in direct space from infinity down to a critical length. Because q_y scales as q_z only scattering from lateral inhomogeneities smaller than a few Å are not included. The domains we investigate are well seen in q_y scans, thus they are much larger than the lower integration limit. In conclusion, due to broad horizontal slit setting the q_y component is integrated and we measure domain distribution along one dimension.

4.4 Coherence length

When mapping the sample in reciprocal space, we make use of the coherent nature of the scattering. Each impinging neutron and photon 'sees' the whole[6] vertical structure in z, resulting in Bragg peaks and Kiessig fringes[7]. We will discuss in the following the concepts of the different coherence lengths.

4.4.1 Geometrical considerations

The geometrical uncertainties are the main source of loss of *transverse* coherence length. We can define two transverse lengths. One is the 'horizontal' coherence length, related to the beam collimation parallel to the sample surface, while the 'vertical' coherence length is related to the beam collimation parallel to the plane of the specular scattering (and almost perpendicular to the sample surface). When mapping lateral structures of the ML we assumed that the neutrons and photons are scattered coherently. The coherence length will set the upper limit of domains that can be measured. For the case of neutrons $\approx$ 100 μm was reported [69], but the instrumental resolution sets an even lower limit of $10 - 30$ μm [75, 76].

[5] We call a slit vertical, if it cuts the beam vertically. The SMR measurements were taken with vertical plane of reflection.

[6] For resonant photons the penetration depth can be smaller, than the layer thickness, but still enough repetition is 'seen' for the appearance of Bragg peaks.

[7] The neutron and photon sources are incoherent. The average resonant photon yield at ESRF is still much less than 1 photon/bunch.

For photons the lateral coherence length can be estimated from simple geometrical considerations. The transverse coherence length will be

$$L_{\mathrm{tr}} = \frac{\lambda}{2\pi}\frac{S}{s} \tag{4.13}$$

Where λ is the wavelength of the incident radiation, S is sample-detector distance and s is the detector slit width. When we take grazing angle reflection, then lateral structures smaller than the projection of L_{tr} can be resolved. In other words:

$$L_{\mathrm{lat}} = \frac{L_{\mathrm{tr}}}{\theta}. \tag{4.14}$$

Here θ is the incident angle.

For the SMR measurements $L_{\mathrm{tr}} = 51$ nm and $L_{\mathrm{lat}} \approx 10$ µm for a typical ω scan at the first AF Bragg peak ($\theta = 0.4°$). The instrumental resolution has an upper limit of ≈ 5 µm being the primary limiting factor.

In conclusion, for both PNR and SMR measurements the instrumental resolution sets the limit of lateral resolution in practice.

Chapter 5

SMR and PNR measurements

One of the main points of this work is the thorough magnetic characterization of a strongly AF coupled Fe/Cr ML. Information on both plane-parallel and plane-perpendicular magnetic structures is obtained. To achieve this goal, coherent scattering methods are utilized. To be able to feed the coherent models with structural information, description by independent 'traditional' structural and magnetization measurements of the ML is needed. Some of the magnetization results were already discussed in Chapter 3. Before we present the SMR measurements, we should describe the sample in accordance with the precision needed for the coherent methods.

5.1 Thickness calibration

Proper thickness calibration is of utmost importance for the evaluation of reflectivity data. Our goal is to describe the Fe/Cr sample 990608, nominally MgO/$\left[^{57}\mathrm{Fe}\left(25\ \text{Å}\right)/\mathrm{Cr}\left(14\ \text{Å}\right)\right]_{20}$ (see 3.1).

5.1.1 RBS and PIXE measurements

In the literature mainly x-ray reflectivity is used to calibrate sample thicknesses. The high-angle x-ray reflectivity measurements are sensitive to the interatomic distances, while the low-angle measurements are sensitive to the total film and the bilayer thicknesses. In our case the individual layer thicknesses cannot be resolved due to the low contrast of Fe and Cr in the given energy range, thus we used applied nuclear physics methods to get the individual thickness of the layers. From combined evaluation of Rutherford backscattering (RBS) and low angle x-ray measurements the values $\left[^{57}\mathrm{Fe}\left(26\ \text{Å}\right)/\mathrm{Cr}\left(13\ \text{Å}\right)\right]_{20}$ were concluded [6]. The sample was measured with particle induced x-ray emission (PIXE) spectrometry [77]. According to the PIXE measurements made on the side of the sample the total thickness was 526.7 ± 44.5 Å Fe and

246.2 ± 19.5 Å Cr, respectively. The homogeneity of the sample was checked by measuring two 1 mm radius spot in the middle of both ends of the sample.[1] The thickness of the sample was homogenous according to the PIXE measurements ($\pm 3\%$). Assuming no plane-perpendicular thickness distribution of Fe and Cr, a $\left[^{57}\mathrm{Fe}\left(26.3\ \text{Å}\right)/\mathrm{Cr}\left(12.3\ \text{Å}\right)\right]_{20}$ was deduced.[2]

Both RBS and PIXE are sensitive to the plane-perpendicular projection of the atomic density, thus to get a thickness value one has to assume a density, which can differ in MBE-grown MLs from the bulk value. Low-angle x-ray measurements could be more precise in determining individual layer thicknesses if the contrast were better and the 'bulk' parameters (electron density, absorption, layer roughness) were known from independent measurements.[3]

The main benefit of the application of nuclear methods was to exclude the 'inverse' system (with thick Cr and thin Fe layers), which gave a better fit to some of the resonant x-ray data. The finally obtained structure can be used as a base for fine-tuning the thickness and related parameters in the resonant x-ray reflectivity curves.

5.1.2 Measured thickness values

The bilayer thickness can be determined from the position of the higher-order Bragg peaks (both structural and magnetic) in SMR and PNR measurements. By this method $d_1 = 38.1 \pm 0.4$ Å and $d_2 = 38.5 \pm 0.15$ Å bilayer thickness was found from SMR measurements taken at ESRF and SPring-8, respectively. From PNR scans $d = 39.3 \pm 2.3$ Å was achieved. From the fitting of the prompt x-ray reflectivity of the SPring-8 measurements $d = 38.2$ Å was found with layer division of $\left[^{57}\mathrm{Fe}\left(25.2\ \text{Å}\right)/\mathrm{Cr}\left(13\ \text{Å}\right)\right]_{20}$. From all the above-described results we will use $\mathrm{MgO}/\left[^{57}\mathrm{Fe}\left(26\ \text{Å}\right)/\mathrm{Cr}\left(13\ \text{Å}\right)\right]_{20}$ [47]. Calculating with the bulk Fe and Cr lattice constants of 2.87 Å and 2.88 Å and taking into account the orientation of the ML the bilayer structure consists of 9 monolayers of Cr and almost 18 monolayers (17.75) of Fe.

5.2 Non-resonant x-ray measurements

5.2.1 High angle x-ray reflectometry

The high-angle x-ray reflectometry scan (not shown) of sample 990608 is similar to the one reported by Fullerton *et al.* for similar systems [14]. The only difference is the appearance of two small peaks indicating possible oxidization. The extra peaks cannot correspond to a Fe/Cr(211) plane; due to the position of the supposed peak and they vanish in the off-specular[4] $\theta - 2\theta$ scans. A splitting of the Fe/Cr(200) peak could be seen, but this could be related to the

[1] The line connecting the spots was parallel to the longer edge of the sample piece of 10×7 mm.
[2] RBS measurements were done by Edit Szilágyi. PIXE measurements were performed by András Kocsonya.
[3] This approach was used by R. Schad [48], but it is not too widely used.
[4] Off-specular by 0.3°.

not proper alignment of the sample and the detector. On the off-specular scans the multilayer peaks are more pronounced.

The presence of oxides could result from the fact that neither buffer nor capping layers were used, giving place to possible bottom and top oxidization.

5.2.2 Low angle x-ray reflectometry

In the case of low angle specular and rocking curves we are luckier, because all the SMR measurements automatically generate a non-resonant counterpart. Due to the excellent control of the experimental parameters like wavelength, slit size, angle (except the zero-position uncertainty which we will discuss later) and the high brilliance, fast and reproducible measurements are possible.

Lateral inhomogeneities of the layer parameters

Comparing the different measuring methods (see Section 5.1) we conclude that the overall thickness fluctuations of the sample do not exceed 3%. This is a small value, but can be still seen by the reflectometric methods. On the other hand, from x-ray reflectivity measurements taken with very small slits ($h = 25$ µm) the perfect local homogeneity of the ML is seen in two orthogonal directions along the middle of the sample (Fig. 5.1).[5] This is not surprising, as the sample was rotated during growth. All SMR measurements were taken in the middle of the sample, while for neutron scans the whole sample width was used. Finally we note that comparison with older scans shows that the structure of the sample (at least as seen by the x-rays at low angle) did not change during the years.

Evaluation of low-angle prompt x-ray measurements

Before we can add the 'nuclear information' to the multilayer it is of immense importance to correctly fit the structural part. For this reason we take measurements taken at SPring-8,[6] because the sample alignment was here the best.[7]

From reflectivity simulations carried out with the IMD software [78] it turned out that the top layers' roughness and thickness are essential parameters to the non-resonant fit. They determine the details of the whole curve. The intensity ratios of the Bragg peaks are also strongly roughness-dependent. We used literature roughness values reported by Schad *et al.* on similar Fe/Cr systems [48] as starting parameter set. The relevant data are summarized in Table 5.1. With these starting roughness values and the help of IMD a good fit was achieved. The final parameters are reported in Table 5.2. Finite instrumental resolution could be applied

[5] In fact the difference between the two scans is so small that they look like a single line.

[6] http://www.spring8.jp/ENGLISH/facility/bl/PublicBeamline/BL09XU/index.html

[7] At the ESRF measurements the sample was placed in a huge Dewar flask, and the whole Dewar flask was rotated, while in SPring-8 a small precision goniometer was used.

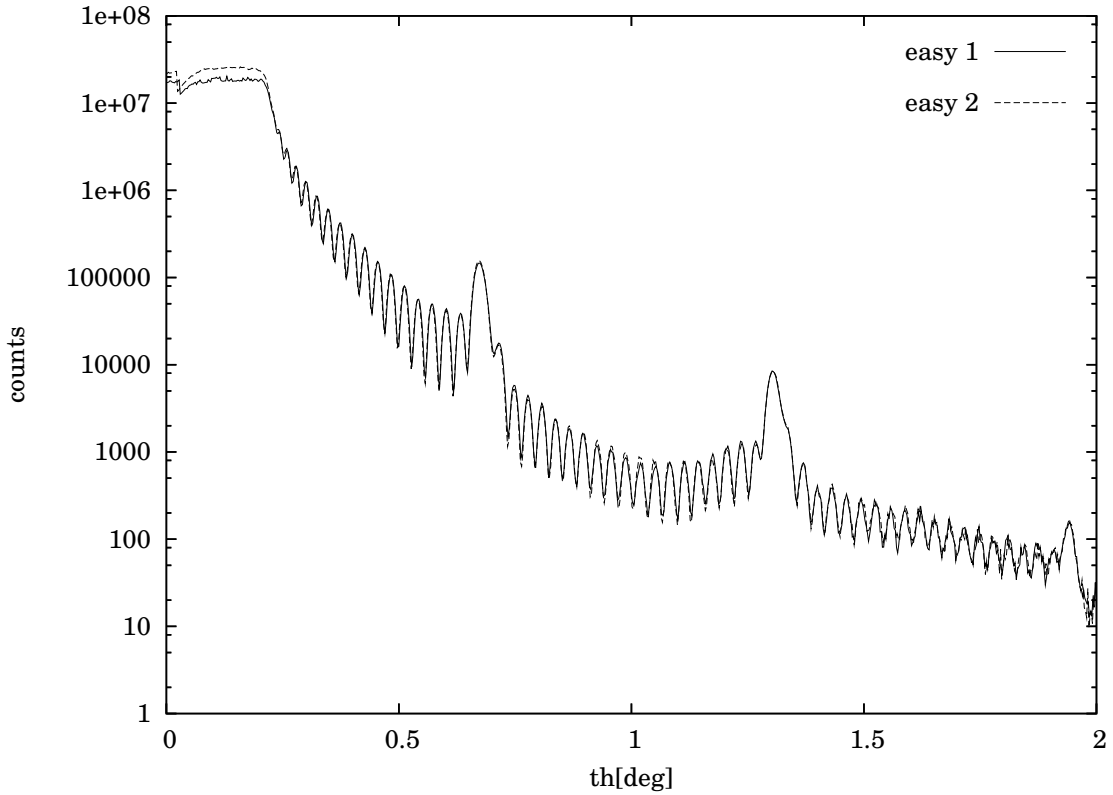

Figure 5.1: X-ray reflectivity (λ = 0.86022 Å) curves of 990608 taken at SPring-8 BL09XU in October 2002. The two easy axes measurement are perpendicular to each other. The detector slit size was 25 μm × 1.5 mm (vertical×horizontal). The beam divergence is 0.0023 mrad × 0.23 mrad (vertical×horizontal). The scattering plane is vertical. The two scans are corrected for θ_0 misalignment and sample size.

to smear out the deep minima by convolution, but EFFI has no such parameter, thus it was not applied.

Low-angle x-ray reflectometry is a powerful tool to see certain parameters of the sample. From IMD simulations and the good reproducibility of the spectra it is obvious that the ML structure is laterally homogenous and vertically periodic (the possible random error of the individual Fe and Cr thicknesses is < 1 Å). But reflectometry gives an 'integral' view of the sample. The oxide for example plays a major role in the exact shape of the reflectivity curve. Also there is no "best" fit, but many possible candidates due to the enormous number of parameters (layer thicknesses, reflectivity values, roughness, possible top and bottom oxidation, etc.). Parameter cross correlations inevitably exist. As a consequence, the more parameters are known in advance from independent measurements, the better chance we have to obtain not only a good-looking, but also a physically realistic model and fit. Fortunately, essential data on similar MLs can be found in the literature [48].

In conclusion, sample 990608 is laterally homogenous and the layer thicknesses are also constant along the plane-perpendicular direction. According to expectations, the top Cr layer is partly oxidized. The interfaces are relatively sharp with average roughness ≈ 1 monolayer. No bottom layer oxidization was found.

Finally we note that that a) the ESRF spectra significantly differ from the SPring-8 spectra[8] and b) that in the range of total reflection — first structural Bragg peak according to EFFI the roughness is not important even with the resonant $\theta - 2\theta$ curves.

$\sigma_{\text{substrate}}$	3.4 Å
σ_{Cr}	3 Å
σ_{Fe}	3 Å
σ_{oxide}	6 Å
Oxide thickness	15 Å

Table 5.1: Thickness and roughness values reported by Schad *et al.* [48] for a Fe/Cr multilayer grown on MgO.

5.3 SMR measurements

Up to now we discussed non-resonant x-ray reflectometry results. By analysis of the delayed reflectivity curves we now focus on the 'magnetic dress-up' of the structure. As those measurements depend on a huge number of parameters, first we try to deduce some basic information by comparing the measurements to each other. Then we will discuss the problems arising due to the integral mode $\theta - 2\theta$ scans. Finally notes on possible model calculations and fits will be presented.

[8] This is due to instrumental uncertainty as the slits were not well controlled in the first series of the ESRF spectra (in October 1999), while very accurately recorded at SPring-8.

layer	1-n [1e-6]	k [1e-6]	thickness [Å]	σ [Å]
oxide1	2.373	0.122	6.36	3.41
oxide2	4.257	0.122	10.48	5.21
Cr1	6.735	0.243	7.97	3.44
Fe1	7.428	0.339	25.2	$0^{\dagger}$
Cr	6.735	0.243	13	1.0 / 1.23
Fe	7.428	0.339	25.2	1.46
MgO	3.566	0.012	∞	1.24

Table 5.2: Thickness and roughness values gained by fitting the SPring-8 low angle prompt measurement ($\lambda = 0.860220$ Å). The assumed structure was: MgO/[Fe/Cr]$_{19}$/Fe1/Cr1/oxide2/oxide1. The σ values correspond to the top interfaces (for example $\sigma_{\text{oxide 1}}$ is the vacuum/oxide 1 interface). The two σ values in the Cr row are the Fe1/Cr and Fe/Cr roughness values, respectively. For further details, see text. († The model was not sensitive to this roughness parameter.)

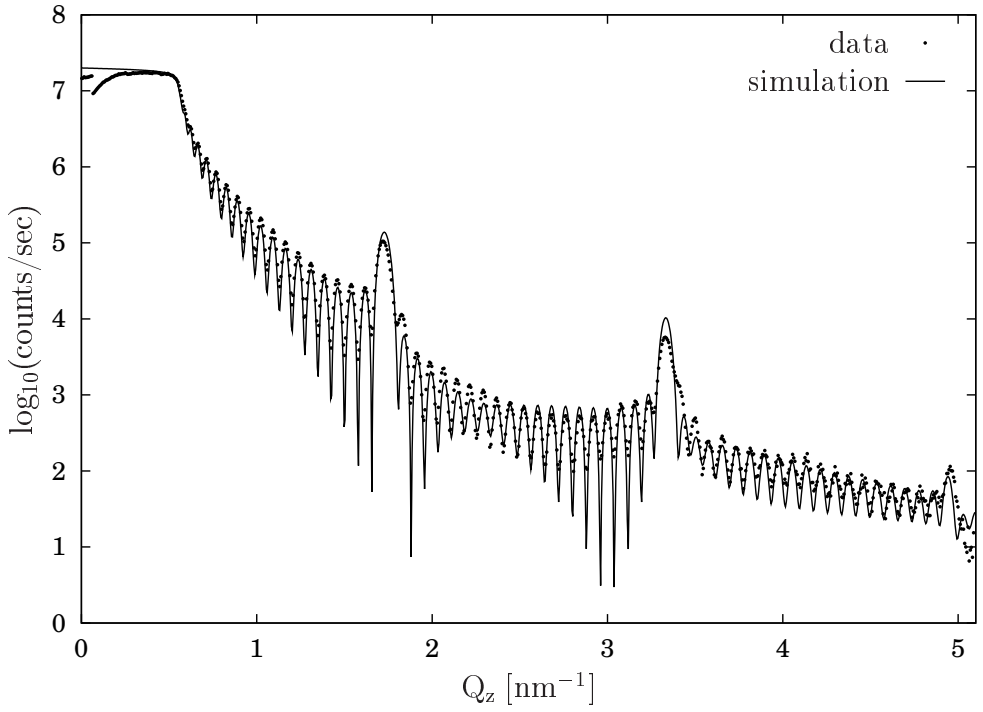

Figure 5.2: IMD fit of SPring-8 measurement (scan 'Budapest54').

SMR scans are taken in the time-differential (TD) and-time integral (TI) modes Time-differential mode may be better in evaluating the detailed hyperfine parameters, while TISMR helps to get a fast overview of the 'landscape' (see Fig 5.3 for example). For AF coupled MLs both method may show the alignment of the layer magnetizations. The majority of SMR measurements, discussed in this work, was done in TI mode, thus we will restrict ourselves to the evaluation of the TISMR measurements.

The resonant $\theta - 2\theta$ scans were taken in 'integral' slit mode (slits wide open), thus not only the specular ridge, but a neighbouring region was integrated[9]. The scan history of Fig. 5.3 is the following: The sample was saturated, then let to remanence *ex situ* before the first measurement. Then it was inserted to the cryostat with layer magnetizations perpendicular to $\mathbf{k}$. This resulted in $\theta - 2\theta$ scan (not shown) with no AF Bragg peak. The field was increased in transversal geometry, thus the sample passed the BSF transition. The emerging AF peak was detected in the following scans (Fig. 5.3), starting with 50 mT and reaching the maximal field of 2 T. Finally the external field was released, producing the spectra of 0 T. The AF peak is visible up to 875 mT. We used the integral-slit mode because the low resonant count rate. In almost all ESRF measurement session transversal-field setup was used. In this setup the external field is set perpendicular to the wave vector of the x-rays.

[9]The region was even non-symmetric in q-space, as one can see at the detector scan graph Fig. 4.9.

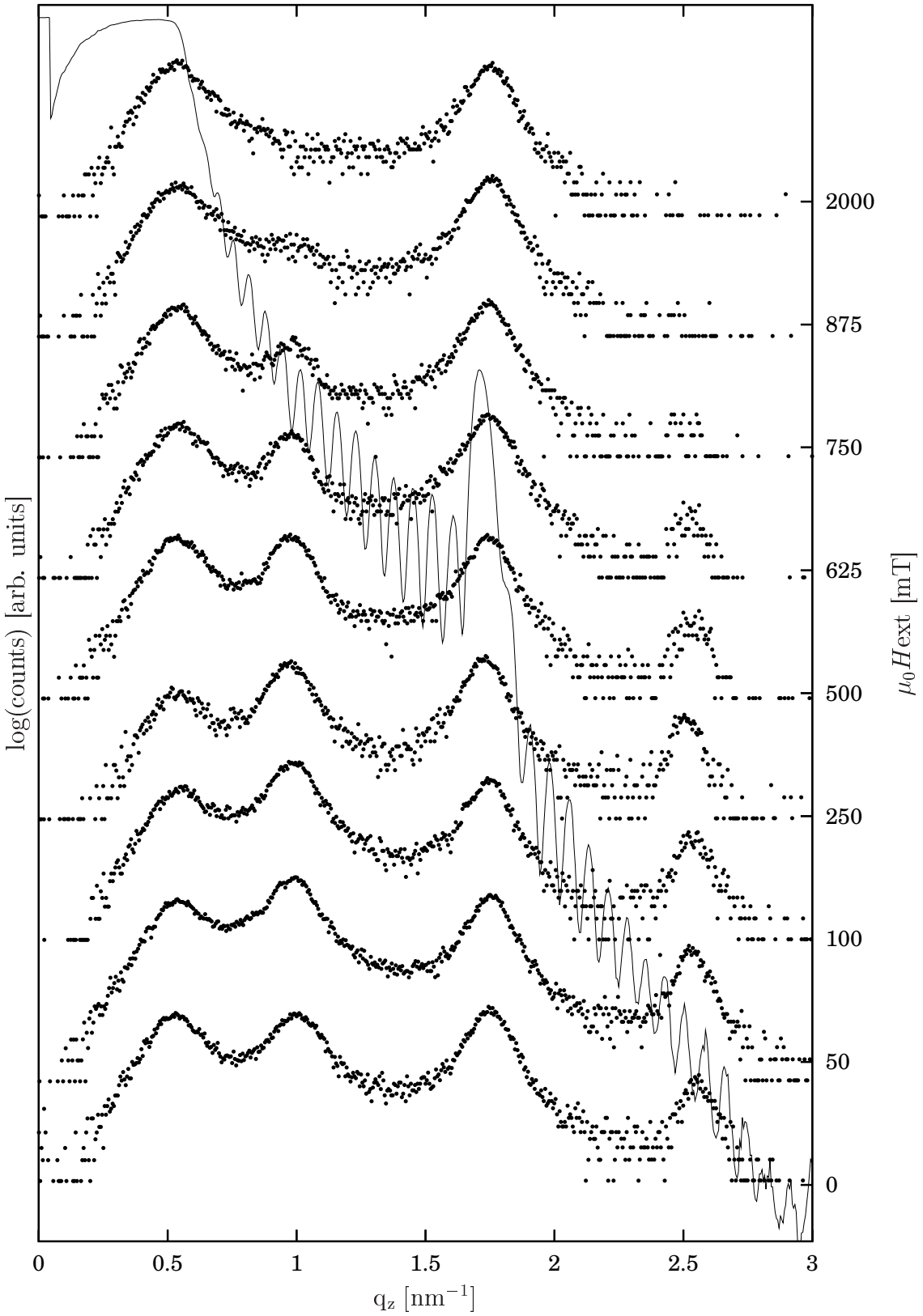

Figure 5.3: TISMR spectra of the Fe/Cr multilayer along easy direction in increasing external field. The scans were taken after the BSF transition (for details see text). In the background the prompt reflectivity is shown for comparison.

Chapter 6

Direct evidence of Bulk Spin Flop

After the introduction to reciprocal space and momentum transfer measurement methods we return to the BSF thread. As emphasized earlier, only *indirect* evidence of the BSF transition was presented in this work. By using *coherent* methods the reciprocal space can be mapped and scattering of different origin distinguished. In our particular case we are able to detect the scattering arising due to magnetic cell doubling, unambiguously showing the BSF transition [6, 47, 79].

If a ML with *in-plane* fourfold crystalline anisotropy is saturated along an easy axis and then the field is reduced to remanence, the layer magnetizations will align perpendicularly to the given easy axis. An increasing field along the orthogonal easy axis[1] causes the so-called bulk-spin-flop (BSF) transition [47].

The indirect evidence (MOKE and VSM) was described in Section 3.3. The first *direct* evidence in the case of sample 990608 came from SMR measurements at BW4 in HASYLAB (Hamburg) [47]. Due to the low resonant count rate only the presence of the BSF was confirmed, the details of the transition were clarified in a subsequent measurement at ESRF ID18 [79].

6.1 BSF and magnetization orientation

In Fig. 6.2 the BSF transition can be followed in a spectacular way.[2] In the starting situation the layer magnetizations of the AF coupled multilayer are parallel/antiparallel to the external field direction[3] and perpendicular to $\mathbf{k}$. This results in no AF reflection. With increasing external field the AF intensities (peaks marked with 1/2 and 3/2) increase. The first AF peak

[1] This can be achieved by either rotating the external field, or equivalently by rotating the sample in remanence, the latter being the easier in the synchrotron case.

[2] The ESRF measurements were done in October 1999 (SI-508).

[3] This was achieved by saturating the sample in 2 T, releasing the field and turning the sample by 90°.

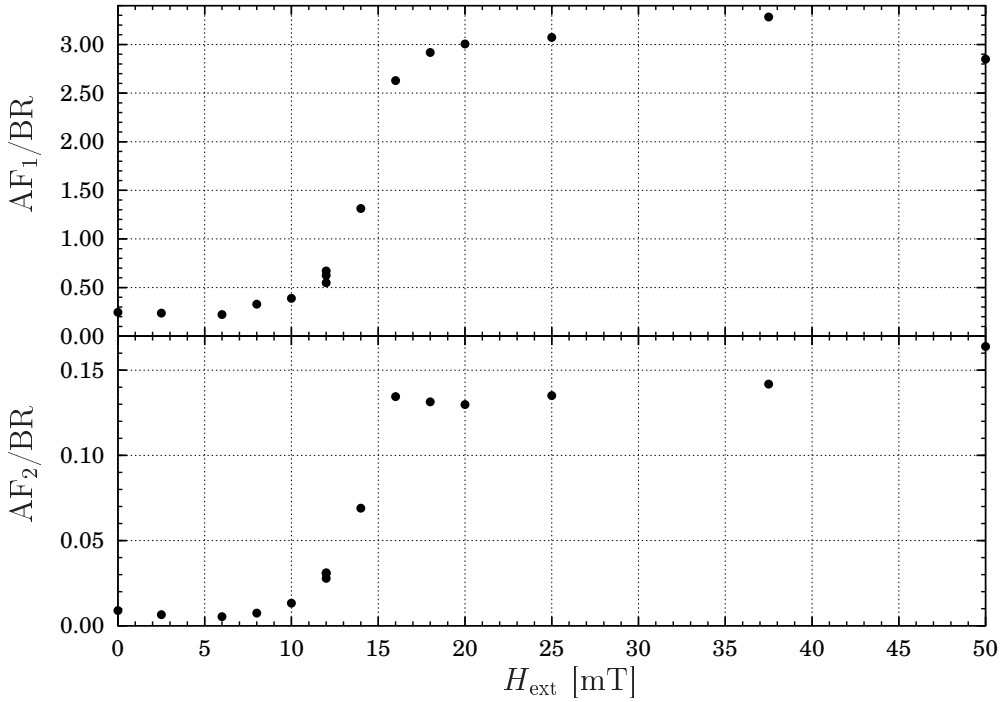

Figure 6.1: The increase of the AF peaks during BSF. The areas of the first and second AF peak (AF_1 and AF_2, respectively) are divided by the first Bragg peak (BR). The AF peaks are the same as peaks 1/2 and 3/2 on Fig 6.2.

divided by the first Bragg peak on Fig. 6.1 clearly shows the BSF transition region between $10-20$ mT. The transition is probably even sharper extending in the range of $12-16$ mT. The uncertainty is caused by the statistical fluctuations and the change in the measurement geometry which causes the change of the footprint angle[4] leading to systematic errors in the AF peak intensity. The 3/2 peak, which is not affected by the footprint correction and background counts from the total-reflection peak starts to appear at 12 mT and has a cusp at 16 mT. The first scan (0 mT) was originally taken in 600 points, 0.5 point/s while all the others are taken in 300 points thus two channels were averaged for the first scan. The scans at 2.5, 5, 20, 25 and 37.5 mT are not shown (they do not contain new information — no change in the ratios). The scans are normalized to the structural Bragg peak. The θ-misalignments are also normalized to each other. Note that at 12 mT 3 scans were taken (12a−c). A refill occurred between 12a and 12b. Scans from 12b−18 mT were taken with double time (1 s/channel).

In conclusion, direct evidence of the BSF transition was shown and sharp BSF range of $12-16$ mT was deduced [63]. Later in the domain description part we will show PNR evidence of the BSF transition and the domain coarsening related to the BSF will be discussed.

[4]The angle at which the sample blocks the incoming radiation totally.

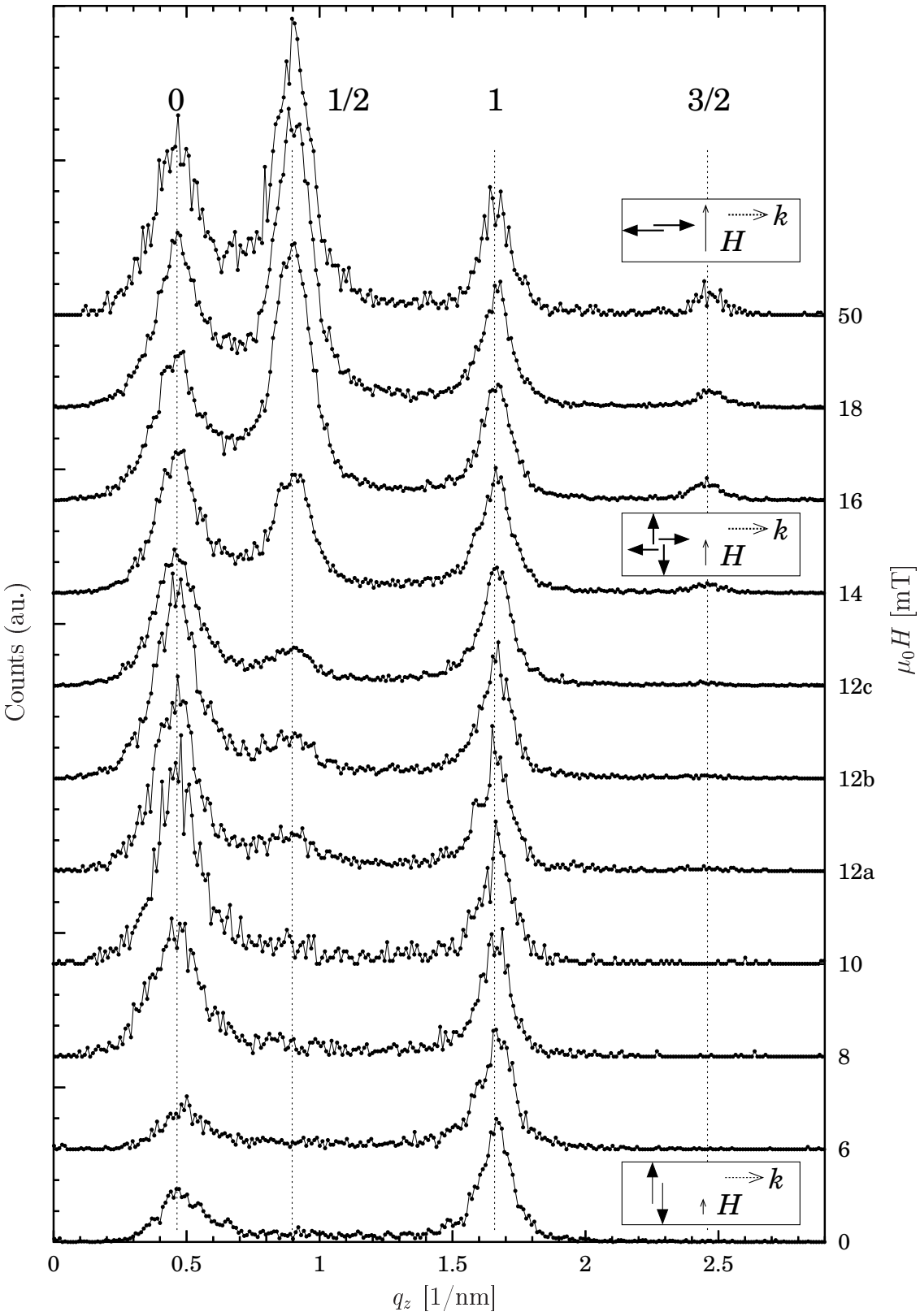

Figure 6.2: BSF as seen on the resonant $\theta - 2\theta$ scans. Curves are shifted for clarity. On the insets the in-plane geometrical relation of the layer magnetizations (bold arrows), the external field and the $\mathbf{k}-$vector of the photons is shown. The scans are normlized to the structural Bragg peak.

Chapter 7

Antiferromagnetic domains

Magnetic thin films and ferromagnetically coupled layers often show ripple domains perpendicular to the external field in order to minimize the stray field energy [4, 17]. In contrast, strongly AF-coupled magnetically compensated MLs like to form 'patch-like' domains. The direct visualization of those domains is difficult due to the vertical compensation of the magnetization in the ML stack.[1] Indirect methods (for example resistance noise, magnetoresistance) and reciprocal space measurements (unpolarized and polarized neutron reflectometry) showed contradictory results on domain evolution [6]. The domain-size distribution in AF-coupled MLs is important, as the domain-size dependent resistance noise may be as large as to limit GMR-sensor applications [80]. Our group was the first to show that by appropriate magnetization history the domains can be enlarged by at least one order of magnitude (domain coarsening) [6].

In remanence, a magnetic ML is in multidomain state. In a strongly AF-coupled ML the magnetic domain structure of the individual ferromagnetic (FM) layers is strictly correlated through the ML stack from substrate to surface. This results in zero net magnetization magnetic super-structure domains in a periodic ML of an even number of equally thick FM layers. We will use the term 'AF domains' for those patch domains. The vertical correlation allows for a two-dimensional representation, e.g. according to the domains of the topmost magnetic layer.

We found a complex domain history in Fe/Cr MLs. The first effect, viz. domain ripening can be best described by tracking the domain evolution from saturation to remanence. In saturation the sample is single domain: all magnetizations are parallel with the external field. When the field is lowered, the forced ferromagnetic state starts to break up into multidomain state. The angle of magnetization between neighboring domains, i.e. the domain-wall angle is small in high fields, and the domain wall energy is also minute. On decreasing the field to remanence, the domain-wall angle grows to 180°. The increasing angle results in increasing

[1] To our knowledge, the only MOKE microscopy observation on Fe/Cr was made on thick trilayers [17].

domain-wall energy, which is in turn can be lowered by increasing the average size of the domains and, thereby, decreasing the domain-wall energy per unit area, a process that we shall call, hencefort, domain ripening. Domain ripening is realized by domain-wall motion, which is a dissipative process, thus the once enlarged domains will not shrink back on increase of the external field again.

The ripened domains may grow further by passing the BSF transition. At the BSF transition the perpendicularly applied field ignites a domain coarsening. As here no domain wall motion, but annihilation plays the main role, the resulting domains can be in the range of the sample. The once coarsened domains will again not shrink back on consecutive BSF transitions. It seems, that the domain size (ripened or coarsened) does not play role in the field range of the BSF transition. We have MOKE evidence on this point as the BSF was repeated with relatively low 'aligning fields', showing the same loop each time (see Sec. 3.3).

Before detailing the experimental results we present theories of domain ripening and Monte Carlo simulations on 'unsaturation' domain formation and domain coarsening.

7.1 Domain ripening

In the following we will present two, admittedly simplified, models of the ripening process. Nevertheless these models will describe the main features of domain ripening and will allow estimating the size of the ripened domains.

7.1.1 Theory 1

In the first theory we will calculate the average domain size of a single magnetic layer in continuum approximation. All magnetization vectors are assumed to lie in plane. The total energy of a round AF domain will be calculated [81].

Energy terms

In the first model only one layer is taken into account. The AF-coupled ML is considered by neglecting the stray field energy, which can be done as in the AF-coupled stack no energy gain is associated with the creation of domains. In this case, domains are formed as a consequence of laterally random unsaturation.

First we calculate the bulk ferromagnetic coupling within the Fe layers. As a first approximation, we take a straight domain wall, with a linear wall profile. Let $\phi(x)$ denote the in-plane angle of the magnetization at the position x and let l be the domain width with the local magnetization varying as $\phi(x) = \{\pi/2, \text{ if } x < 0,\ \pi/2 - \pi x/l, \text{ if } 0 \leq x \leq l \text{ and } -\pi/2 \text{ if } x > l\}$. In this case the exchange energy will be: $E_x = \int A\left(\phi'\right)^2 dV$ (see [4, pp. 112, 217]). A slab of

width w, total height t_{Fe} and wall width l has the energy of[2] $E_x = At_{\mathrm{Fe}}w\pi^2/l$. Here A is the exchange constant of bulk iron.

For the same type of wall the anisotropy energy can be also easily calculated, in our case E_K being equal to[3] (see for example [4, p. 113]): $E_K = \int K \sin^2\phi \cos^2\phi \, dV$. Integrating with respect to the given volume we will have[4] $E_K = t_{\mathrm{Fe}}wKl/8$. The total energy is the sum of the two previous terms:

$$E_w = E_x + E_K = t_{\mathrm{Fe}}w\left(\frac{A\pi^2}{l} + \frac{Kl}{8}\right). \tag{7.1}$$

In case of equilibrium dE/dl should vanish. From this we get:[5]

$$l = 2\pi\sqrt{\frac{2A}{K}}. \tag{7.2}$$

Substituting l in the energy function we finally have:

$$E_w = \pi t_{\mathrm{Fe}}w\sqrt{AK/2}. \tag{7.3}$$

If we bend the domain wall to get a round domain of diameter $\xi \gg l$ then all the above argumentation stays valid with the substitution $w = \pi\xi$. Thus the energy of a domain of diameter ξ is

$$E_w = \pi^2 t_{\mathrm{Fe}}\xi\sqrt{AK/2}. \tag{7.4}$$

In case of applied external field the directions of the momenta will change less. The previous arguments could be repeated with a new $\phi(x)$ function: $\phi(x) = \phi_0$, if $x < 0$, $= \phi_0 - 2\phi_0 x/l$, if $0 \le x \le l$ and $= -\phi_0$ if $x > l$. In this case the exchange energy will be: $E_x = 4At_{\mathrm{Fe}}w\phi_0^2/l$. The anisotropy energy is:[6] $E_K = t_{\mathrm{Fe}}wKl\,(4\phi_0 - \sin 4\phi_0)/32\phi_0$. Thus the total energy equals to:

$$E_w = t_{\mathrm{Fe}}w\left(\frac{4A\phi_0^2}{l} + \frac{Kl\,(4\phi_0 - \sin 4\phi_0)}{32\phi_0}\right). \tag{7.5}$$

From $dE/dl = 0$ we get:

$$l = \sqrt{\frac{128A\phi_0^3}{K\,(4\phi_0 - \sin 4\phi_0)}} \tag{7.6}$$

---

[2] $\phi(x) = \pi/2 - \pi x/l \to \phi(x)' = -\pi/l, \quad A_e = A\int_0^{t_{\mathrm{Fe}}} dz \int_0^w dy \int_0^l (\pi/l)^2\, dx = At_{\mathrm{Fe}}w\left(\pi^2/l^2\right) \times l$

[3] $E_{Kc} = K_{c1}\left(m_1^2m_2^2 + m_1^2m_3^2 + m_2^2m_3^2\right) + K_{c2}m_1^2m_2^2m_3^2$, where m_i-s are the angle cosines (or the magnetization components along the cubic axes). In our coordinate system $m_1 = \sin\vartheta\cos\phi$, $m_2 = \sin\vartheta\sin\phi$, $m_3 = \cos\vartheta$ and $\vartheta = \pi/2$. We are neglecting the second term ($K_{c2} = 0$).

[4] Again, the integrand depends only on x. The result was crosschecked by Mathematica.

[5] This result is $\sqrt{8}$ times the wall width, one can obtain by variational calculus. See [4, pp. 215-219] for example.

[6] To see the relationship with the previous case: $\frac{4\phi_0 - \sin 4\phi_0}{32\phi_0} = \frac{1}{8}\left(1 - \frac{\sin 4\phi_0}{4\phi_0}\right)$.

Substituting l to the energy term, the final equation is

$$E_w = t_{\mathrm{Fe}} w \sqrt{\frac{AK\phi_0\left(4\phi_0 - \sin 4\phi_0\right)}{2}}. \tag{7.7}$$

And for a round domain of diameter ξ

$$E_w = \pi t_{\mathrm{Fe}} \xi \sqrt{\frac{AK\phi_0\left(4\phi_0 - \sin 4\phi_0\right)}{2}}. \tag{7.8}$$

Now we have to calculate the energy loss due to magnetization reversal. This is the so-called hysteresis loss, which is related to coercivity. When the local layer-magnetization flips once back and forth the energy loss due to coercivity will be equal to the area of the 'virtual' $H - M$ graph. In first approximation, this is $E_c = 4\mu_0 H_c M V$ where $\mu_0 H_c$ is the coercive field, M is the bulk Fe magnetization and V is the volume involved. For a round domain expanding its diameter from ξ to $\xi + \delta\xi$ where $\delta\xi \ll \xi$ we will have[7]

$$\delta E_c = 2\pi\xi t_{\mathrm{Fe}} \mu_0 H_c M \delta\xi. \tag{7.9}$$

In the case of $\phi_0 < \pi/2$ the magnetization reversal loss is less. Only the perpendicular-to-field component has to flip, which is proportional to $\sin\phi_0$. Thus the final form of δE_c:

$$\delta E_c = 2\pi\xi t_{\mathrm{Fe}} \mu_0 H_c M \sin\left(\phi_0\right) \delta\xi. \tag{7.10}$$

The hysteresis loss is a dissipative, always acting against the domain wall movement, it actually resembles friction. When coming from saturation, the domain size is small, governed by the primary domain formation rules (see later). Close to saturation, the domain-wall energy is small then by lowering the external field it grows. The system would like to get rid of the extra excess energy. In this simple model the domains will grow to make less domain walls and, thereby, reducing the domain-wall density. They can do so only as long as the energy 'drive' is bigger than the dissipative term. If a round domain of diameter ξ expands to $\xi + \delta\xi$, where $\delta\xi \ll \xi$ then the energy gain is:

$$\delta E_w = \pi t_{\mathrm{Fe}} \sqrt{\frac{AK\phi_0\left(4\phi_0 - \sin 4\phi_0\right)}{2}} \delta\xi. \tag{7.11}$$

Taking $\delta E_w = \delta E_c$ we have for ξ:

$$\xi = \frac{\sqrt{AK\phi_0\left(4\phi_0 - \sin 4\phi_0\right)}}{2\sqrt{2}\mu_0 H_c M \sin\phi_0}. \tag{7.12}$$

[7] We took only half of the total hysteresis loss curve because, during ripening the moments should turn only once.

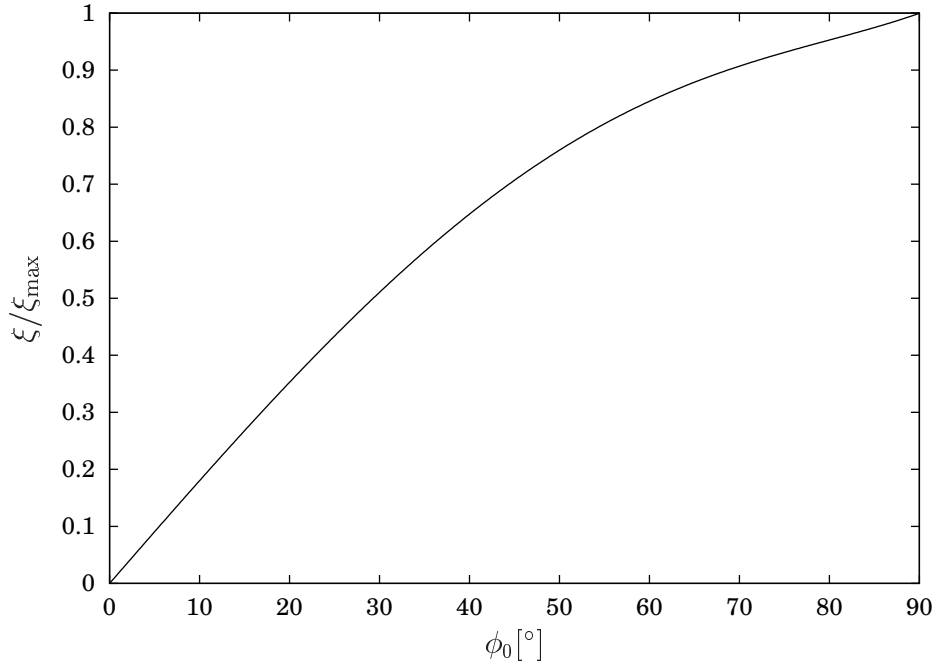

Figure 7.1: The angle dependence of ξ in 'Theory 1' in units of $\xi_{\max}$. The angle is measured from the external field, zero meaning saturation.

As expected, this equation does not depend on t_{Fe}, because only bulk parameters were used, and due to the symmetry of the problem, this is a two-dimensional case. In the limiting case ($\phi_0 = \pi/2$) we will have:

$$\xi_{\max} = \frac{\pi\sqrt{AK}}{2\sqrt{2}\mu_0 H_c M}. \tag{7.13}$$

We can plot the domain evolution as the function of $\xi/\xi_{\max}$ (Fig. 7.1).

The coercive field H_c is only known with a large error. Indeed, due to the fully compensated, AF-coupled nature of the investigated ML, H_c cannot be deduced from conventional magnetization measurements. In the following we shall use the rough estimate $0.2\ \mathrm{mT} < \mu_0 Hc < 3\ \mathrm{mT}$. Substituting the parameters $A = 2.1 \cdot 10^{-11}$ J/m $K = 4.7 \cdot 10^4$ J/m^3, $M = 1.7 \cdot 10^6$ A/m from [81], we have $220\ \mathrm{nm} < \xi_{\max} < 3.45\ \mu\mathrm{m}$.

This model is lacking a basic parameter, namely the interlayer AF coupling. This model not only does not depend on J, but in the limiting case of $K = 0$ breaks down (the energy becomes zero and wall width infinite). A second shortcoming of this model is the exclusion of the Zeeman energy, which would lower the domain wall energy in external fields and would make the domains slightly bigger but would not change $\xi_{\max}$. This will also be corrected in the next model.

7.1.2 Theory 2

The redefined model takes into account the interlayer coupling and assumes a symmetric wall structure which runs perpendicular to the ML stack (see Fig.7.2). In the first approximation

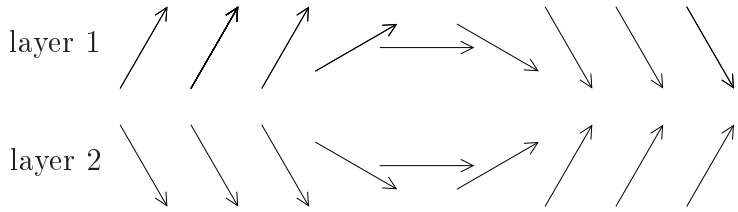

Figure 7.2: The sketch of a symmetric wall in strongly AF-coupled ML according to 'Theory 2'. The two layers are aligned symmetrically relative to the applied (in this case horizontal) external field. The arrows are representing the in-plane angle ϕ of the layer magnetizations.

we will neglect the magnetocrystalline anisotropy. In this case the two energy terms are the FM intralayer coupling and the uniaxial-type[8] AF interlayer coupling. We will again integrate with respect to the whole stack, but neglect finite-stacking effects. The energy terms are $E_x = A\int (\phi')^2\, dV$ and $E_J = J\int \cos 2\phi\, dA_t$ where dA_t means integration with respect to all Fe interfaces. In our case this would mean $E_J = nJ\int \cos 2\phi\, dA$ where dA is the area of the domain wall. Let us denote the thickness of a single Fe layer with t_1, thus $t_{\mathrm{Fe}} = nt_1$ where n is the number of the Fe layers. For this model we will calculate everything for a single layer with two coupled surfaces.

The energy, which has to be minimized for a domain wall along the x-axis[9] becomes in remanence:

$$E_w = E_x + E_J = At_1 w \int_{-\infty}^{\infty} \left(\phi\,(x)'\right)^2\, dx + 2Jw \int_{-\infty}^{\infty} \cos^2 \phi\,(x)\, dx \tag{7.14}$$

This can be directly substituted to the energy density of eq. (3.105) in [4] with the constants $A = A$ and $2J/t_1 = K$ and, integrating the result, the wall energy [4, p. 217] will be:

$$E_w = 4w\sqrt{2At_1 J} \tag{7.15}$$

In the case of external field (including the Zeeman term in a two-sublattice model), with domains having angles ϕ_0 and $-\phi_0$ a more generalized formula will apply. In this case we can use the formula (3.111) from [4]. In the original formula the generalized energy density term is $G\,(\phi) - G_\infty = K_{u1}\,(\cos\phi - \cos\phi_0)^2$ which we should integrate to get the wall energy in one dimension: $\gamma_w = 2\sqrt{A}\int_{-\phi_0}^{\phi_0} \sqrt{G\,(\phi) - G_\infty}\, d\phi$ yielding:

$$\gamma_w = 2\sqrt{AK_{u1}} \int_{-\phi_0}^{\phi_0} \cos\phi - \cos\phi_0\, d\phi = 4\sqrt{AK_{u1}}\,(\sin\phi_0 - \phi_0\cos\phi_0)\,. \tag{7.16}$$

In our case integrating γ_w with respect to the other two dimensions and substituting the

[8] $\cos 2\phi = 2\cos^2\phi - 1$. And we can neglect constant terms in the energy expression.
[9] $\phi\,(-\infty) = \pi/2$, $\phi\,(\infty) = -\pi/2$

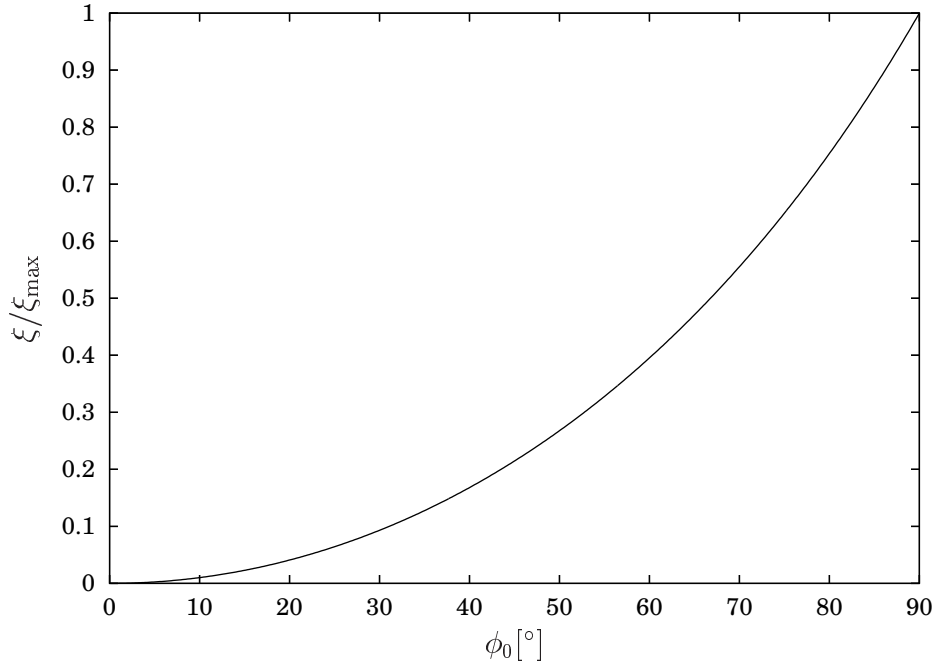

Figure 7.3: The angle dependence of ξ in 'Model 2' in units of $\xi_{\max}$. The angle is measured from the external field, zero belonging to saturation.

constants and calculating for a domain with diameter ξ we have:

$$E_w = 4\pi\xi\sqrt{2At_1J}\left(\sin\phi_0 - \phi_0\cos\phi_0\right). \tag{7.17}$$

The hysteresis loss will be the same as for (7.10). Making the two variations equal we get:

$$\xi = 2\sqrt{\frac{2AJ}{t_1}}\,\frac{1-\frac{\phi_0}{\tan\phi_0}}{\mu_0 H_c M}. \tag{7.18}$$

We will get the maximal domain size at $\phi_0 = \pi/2$. Substituting the literature values the range of $\xi_{\max}$ is now 1.6 μm $< \xi_{\max} <$ 24 μm.

We can include anisotropy in this second model. We will calculate only $\xi_{\max}$ ($H = 0$ T). The equation we will start from is again taken from [4] (3.128): $E_w = K_{u1}\left(\cos^2\phi + \kappa\cos^4\phi\right)$. Where $\kappa = K_{u1}/K_{u2}$

In our case the integrand of the energy term[10] (fourfold anisotropy and uniaxial type coupling) is:

$$e_w = \frac{2J}{t_1}\cos^2\phi + K\cos^2\sin^2\phi = \left(\frac{2J}{t_1} + K\right)\cos^2\phi - K\cos^4\phi. \tag{7.19}$$

To get the wall density we should substitute the values $K_{u1} = 2J/t_1 + K$, $K_{u2} = -K$ and

[10] $\cos^2\phi\sin^2\phi = \cos^2\phi - \cos^4\phi$

$\kappa = -\frac{K}{2J/t_1+K}$, thus $\kappa < 0$. In this case the wall energy density:

$$\gamma_w = 2\sqrt{AK_{u1}}\left(1 + \frac{1+\kappa}{\sqrt{-\kappa}}\operatorname{arctanh}\sqrt{-\kappa}\right). \tag{7.20}$$

If we integrate for one layer (thickness and width) and write our variables:

$$E_w = 2wt_1\sqrt{A\left(2J/t_1 + K\right)}\left(1 + \frac{2J/t_1}{\sqrt{K\left(2J/t_1+K\right)}}\right)\operatorname{arctanh}\sqrt{-\kappa}. \tag{7.21}$$

Taking the actual values of J, t and K κ will be small. In this range $\tanh x \approx x$, thus

$$E_w = 2wt_1\sqrt{A\left(2J/t_1 + K\right)}\left(2 - \frac{K}{2J/t_1+K}\right). \tag{7.22}$$

With $K = 0$ equation 7.15 will be a special case of (7.22). For a round domain ($w = \pi\xi$) the energy of the wall will be

$$E_w = 2\pi\xi t_1\sqrt{A\left(2J/t_1 + K\right)}\left(2 - \frac{1}{\frac{2J}{Kt_1}+1}\right). \tag{7.23}$$

The hysteresis loss (7.11) at zero field is $\delta E_c = 2\pi\xi t_1\mu_0 H_c M\delta\xi$. From this the wall width at zero field is:

$$\xi_{\max} = \frac{\sqrt{A\left(2J/t_1 + K\right)}\left(2 - \frac{1}{\frac{2J}{Kt_1}+1}\right)}{\mu_0 H_c M} \tag{7.24}$$

Substituting all numerical parameters, we will result in a maximal domain diameter in the interval of $1.6 - 24.1$ µm. Note that practically no difference can be seen compared to the $K = 0$ case, which will be evident if we make further approximations for the small anisotropy term ($\alpha = t_1K/2J \ll 1$).

$$E_w = 2\pi\xi\sqrt{2t_1AJ\left(1+\alpha\right)}\left(2 - \frac{1}{\frac{1}{\alpha}+1}\right) \tag{7.25}$$

$$2 - \frac{1}{\frac{1}{\alpha}+1} = 1 + \frac{1}{1+\alpha}, \tag{7.26}$$

$$\frac{1}{1+\alpha} \approx 1 - \alpha, \quad \sqrt{1+\alpha} \approx 1 + \frac{1}{2}\alpha, \tag{7.27}$$

$$\sqrt{1+\alpha}\left(1 + \frac{1}{1+\alpha}\right) \approx \left(1 + \frac{1}{2}\alpha\right)(2-\alpha) = 2 - \frac{1}{2}\alpha^2, \tag{7.28}$$

$$E_w \approx \pi\xi\left(4 - \alpha^2\right)\sqrt{2t_1AJ} \tag{7.29}$$

In conclusion, the leading "perturbative term" vanishes, thus the anisotropy energy accounts only for ≈ 0.86‰ lowering of the wall energy, which can be safely neglected.

'Theory 2' is also a 'first-guess' model'. A better domain-ripening model could only be made by the use of micromagnetic calculations. Note that both models predict a continuous domain ripening.

7.1.3 AF-domain formation

In the previous part we treated the ripening of the already existing AF domains. But how are those AF domains formed initially? In the following Monte Carlo simulation we will try to give a phenomenological answer to this question [82].

Let us assume a lateral distribution of the saturation field (caused for example by Fe and Cr layer roughness). This inevitably leads to independent AF domain nucleation centers. When the external field is lowered from saturation, the strongest-coupled parts will form AF domains first. They can do this in two different ways. The top layer may start rotating to the right or to the left (clockwise or counter-clockwise). The two types of domains will grow until the whole sample is unsaturated. In our model we associate the domain formation with the correlation length of the saturation field. We assume the absolute thickness variations of Cr and Fe to be equivalent. Due to the strong oscillatory thickness dependence of the coupling in the Fe/Cr system [83], the actual correlation length of the AF coupling and, consequently that of the unsaturation domains is much smaller than the correlation length of the Cr spacer thickness.

Pixel representation

Due to the vertically correlated domains, the strongly-coupled AF stack can be modeled as a two-dimensional grid of pixels. Each pixel represents the direction of the magnetization of the topmost layer in a given pixel area. The mesh size of the grid should be taken smaller than the actual domain size. In our model, each pixel possesses a macroscopic classical magnetization, saturation field and anisotropy energy. The domains are formed on this grid by first-neighbor rules explained later. Domains are represented as contiguous sets of pixels of the same color.

Saturation field distribution

The unsaturation or primary domain formation is governed by the distribution of the saturation field. The higher the saturation field of a given pixel is the sooner will the pixel unsaturate. First we create a grid of uncorrelated random numbers $U(\mathbf{r})$ of Gaussian distribution according to [9] (p. 288), where $\mathbf{r} = (x, y)$ is the position vector. The saturation field distribution is generated by smoothing the grid by an empirical width ω according to

$$D(\mathbf{r}) = \sum_{|\mathbf{r}-\mathbf{r}'|<\omega} \left(1 - \frac{(\mathbf{r}-\mathbf{r}')^2}{\omega^2}\right) U(\mathbf{r}') \tag{7.30}$$

Periodic boundary conditions are used. Decreasing the external magnetic field H_{ext} from saturation, the ML gradually unsaturates. When H_{ext} matches the saturation field value H_{s} of a given pixel, the pixel unsaturates. The pixel will choose its sense of rotation according to so-called flipping rules. When $H_{\mathrm{ext}} < \min(H_{\mathrm{s}})$, the whole ML is completely unsaturated. We can represent the domains according to their top layer's magnetization: white=left, black=right, gray=still saturated.

Flipping rules

The set of first-neighbor rules governs the decision of each pixel. In our model, all eight first neighbors have equal weights. To avoid creating domain walls, the pixel to decide chooses the sense of rotation of the majority[11] or chooses at random if no decision can be made using the previous rule. The flipping rules involve only first neighbors, allowing for a fast realization of the above algorithm. The grid is scanned for saturated pixels. When found, it is checked if all still-saturated neighbors possess a lower H_{s} value than the one found. If yes, the pixel is allowed to choose its sense of rotation according to the above flipping rules. If not, the next pixel is chosen. The scan of the grid is repeated as long as all saturated pixels flip to either left or right (black or white). Finally, the temporal evolution of the domains is reproduced and a movie of the domain formation is constructed from the final state (Fig 7.4).

The above-described Monte Carlo simulation was tested with MOKE microscopy data from Fe/Cr trilayers [82,84] with good agreement (see Fig. 7.5. In the description of the unsaturation domain formation the crystalline anisotropy term can be neglected, thus the primary domain size does not depend on the in-plane sample orientation. When we are in the low-field region (after the ripening) the orientation does count as will be seen in the following.

7.1.4 Domain ripening in easy direction

In the easy-direction unsaturation scenario the moments rotate smoothly to the AF-remanent state from the FM alignment in saturation. The flipping rules do not contain the domain wall energy explicitly, thus from this model no ripening is expected. A more sophisticated micromagnetic simulation (explicitly including domain walls) should give a better Monte Carlo description.

The ripening of the domains is connected with the coercivity of the Fe films, as discussed in the previous models (7.1.1 and 7.1.2). As the field decreases, the domain-wall angle and, consequently, the domain-wall energy per unit are increases. Therefore also the domains increase in order to decrease the domain-wall density and, thereby, to minimize the domain-wall energy. This spontaneous growth of the domains is limited by the domain-wall pinning (coercivity) and the gain in domain-wall energy is not enough to increase the average domain size

[11] Neighbor pixels still in saturation have no influence

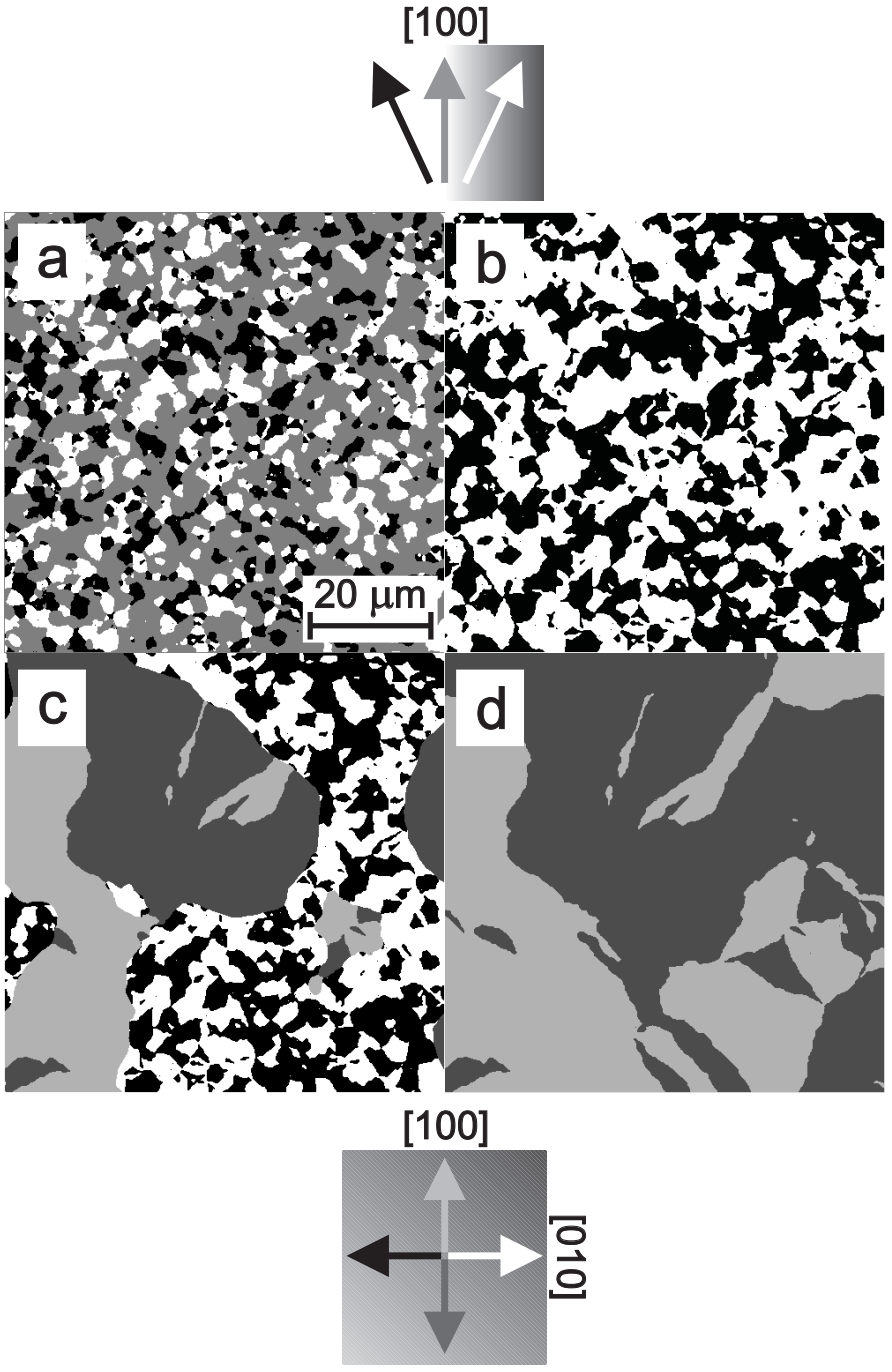

Figure 7.4: Unsaturation (a,b) and BSF (c,d) domain formation [82]. In the unsaturation domain formation black and white pixels represent top layer rotation to the left and right, respectively, gray pixels being still in saturation. The easy axes of the fourfold anisotropy are along [100] and [010] directions. The sample was saturated in the [100] direction. The grid contains 500×500 pixels. The smoothing widths of the primary and secondary distributions (before and after the BSF transition, see below) are $\omega_1 = 10$ and $\omega_2 = 100$, respectively. In (c) and (d), the system during and after the spin flop is shown. The BSF is induced by an increasing field along the [010] direction. The secondary large domains are perpendicular to the primary small ones. Gray-scale scheme id (d): light gray pixels: top layer up, dark gray pixels: top layer down. The scale was adjusted [84] to a Kerr image measured by Rührig *et al.* [17] with a mesh size of 146 nm.

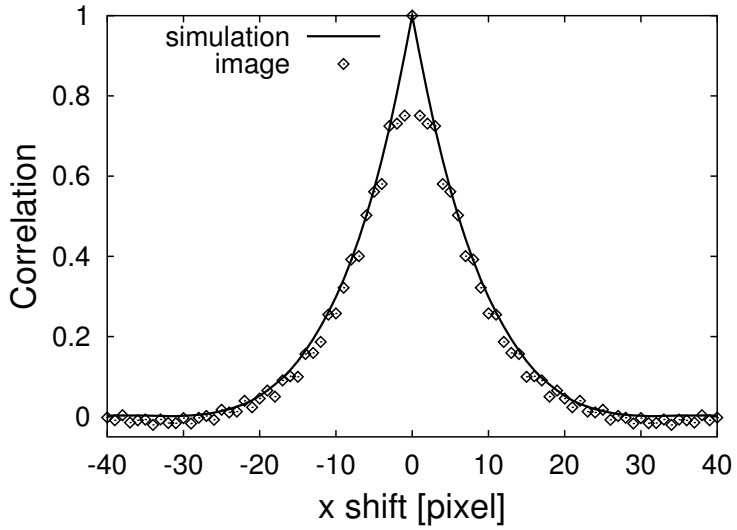

Figure 7.5: "The autocorrelation function of the Kerr microscopic image (Fig. 4b in [17] as compared with the autocorrelation of the simulated image in Fig. 7.4b with $\omega = 10$ and pixel size of 146×146 nm^2." [84]

beyond a certain limit. The domains are bound to their original sense of rotation as long as the magnetic field remains parallel to the original axis of magnetization, since in higher fields the Zeeman energy, in lower fields the magneto-crystalline anisotropy stabilizes the domain orientation.

7.1.5 Domain ripening in hard direction

In the hard-axis scenario there is a second 'critical point', viz. the hard-axis reorientation transition (see Section 2.6). Now the system is in a frustrated state between different energy minimum paths. The role of domain walls will be enhanced. In a simple model unsaturation along a hard axis result in nearly 180° domain walls when approaching a critical field H_{prt} [85]. At this field, the sublayer magnetizations are directed along the hard axis and perpendicular to the field, a configuration that becomes energetically unfavorable on further reducing the field.[12] In remanence the magnetizations will lie parallel to the easy axes. See Fig. 7.6 for the evolution of domain ripening in hard direction.

Assuming that the domains do not change shape but rotate, the domain image remains the same down to H_{prt} as it was in complete unsaturation, only the angles of the layer magnetizations change. At the spin-partition field $H_{\mathrm{prt}}(\mathbf{r})$ the pixel magnetizations start partitioning, i.e., rotating clockwise or anticlockwise. The AF domains gradually develop into four different orientations along the easy axes in remanence resulting in $\pm 45°$ relative rotation from the H_{prt} state. The domain nucleation of this partition spin-flop is now governed by the effective correlation length of the spin-flop field, which is much broader than that of the saturation field. A

[12] This is an oversimplified picture as we know that for finite number of layers complex reorientation transition occurs, but the main idea, i.e. the frustration of the magnetizations (domains) is still valid.

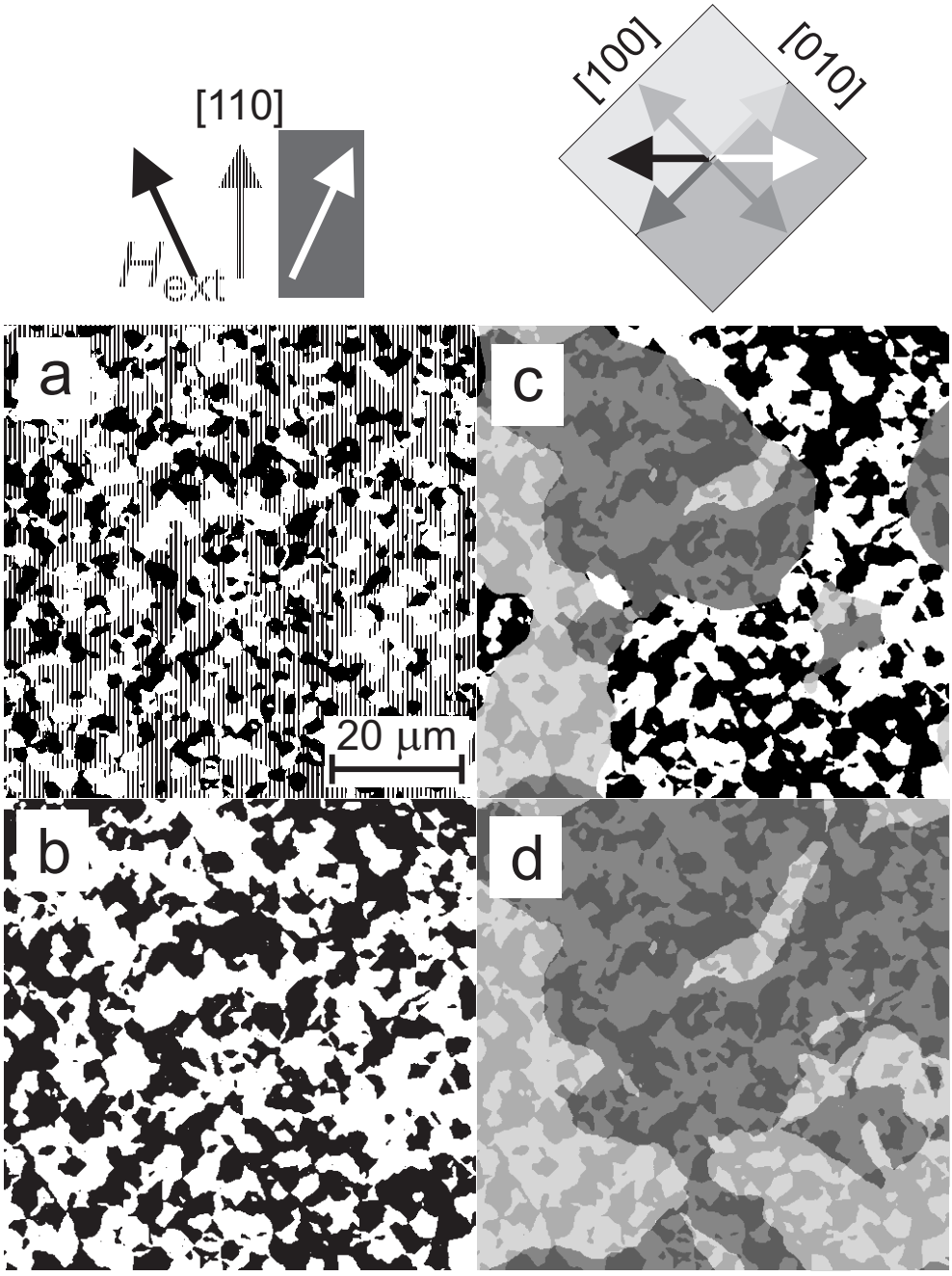

Figure 7.6: Evolution of AF domain structure during unsaturation along a hard direction of the fourfold anisotropy [85]. a) In high field, partial unsaturation, b) in intermediate field, above spin partition, c) following incomplete partition of domains according to the two perpendicular easy directions, d) in remanence. The gray gradation represents the direction of the top layer of a pixel according to the arrows, while the striped regions in a) are still in saturation. The easy axes of the fourfold anisotropy are directed along the [100] and [010] crystalline axes of Fe. The grid is 500 by 500 pixels. The smoothing widths of the unsaturation and BSF distributions are $\omega_1 = 10$ and ω_2=100, respectively. The scale was adjusted [84] to a Kerr image measured by Rührig *et al.* [17] with a mesh size of 146 nm.

pixel can choose its new direction if all pixels with higher spin-flop field have already decided. A left-directed pixel (e.g., top layer pointing left) can now choose between up-left and down-left directions. The rules are similar to the unsaturation rules, but here the energy penalty of a neighbor pixel is proportional to the square of the relative angle of the neighbors.[13]. The pixel to decide will choose the direction with the least total energy penalty. Consequently, the remanent domain structure following a hard axis unsaturation remembers the primary domain structure. The four types of domains are not randomly distributed, but in groups of two in order to avoid 180° domain walls. Indeed, if a left-directed pixel has chosen to rotate left-up, a neighboring right-directed domain will definitely rotate right-up rather than right-down since the domain-wall angle in this case will be only 90°.

7.1.6 Domain coarsening on BSF

At the BSF transition the magnetic moments are switched by ±90° by the external field. This abrupt change in layer magnetization gives the chance to change the domain structure. In Fe/Cr MLs, we found a coarsening of the domains on BSF transition [6].

The mechanism of the BSF-induced *coarsening* basically differs from that of the unsaturation domain formation and ripening. Indeed, when an increasing magnetic field is applied in the *magnetization-parallel* direction, the anisotropy energy preserves the primary domain structure only for $H < H_{\mathrm{bsf}}$. At H_{bsf}, the system becomes energetically unstable and the layer magnetizations flip to the field-perpendicular direction. There is again a freedom in the sense of rotation and, similar to H_{s}, also H_{bsf} obeys a distribution. However, at $H \approx H_{\mathrm{bsf}}$ the system is close to an energy maximum and behaves like an explosive material: it may jump to an energy minimum by 90° or −90° rotation of the magnetization. Once the first region with the lowest value of H_{bsf} 'decides' between a 90° or −90° flop, it will 'ignite' the neighbor regions, which will choose the same direction of magnetization to avoid creating new domain walls. In contrast to primary domain formation, secondary domains at the BSF transition may grow *without any long-range domain-wall motion*, and this growth is, therefore, not limited by coercivity. BSF-induced domain coarsening is an *explosion-like* 90° *flop of the magnetization annihilating primary* 180° *walls*. Consequently, the secondary patch domain size might become comparable with the sample size.

In the BSF Monte Carlo simulations [82] we used similar spin-flip rules, which ensure the unnecessary creation of excess domain walls. A pixel can choose now its new direction if all pixels with lower spin-flop field have already decided. The rules are now the same as those during unsaturation, but the pixels may now flip from the left/right into the up/down orientation. In a simple model of the domain-wall energy, the energy penalty is proportional to the sum of the square of the relative angle of the neighbors. It can be shown that with these

[13] We assume, that in first approximation the domain wall energy is proportional to the square of the angle of the wall

conditions, the secondary domain formation is independent of the primary structure and only depends on the lateral distribution of the spin-flop field. The BSF domain coarsening is shown in Fig. 7.4.

7.1.7 Domain stability and process

If in the ML isolated round domains would exist, they could be annihilated below a critical size. For a ML with patch-domains, a chessboard-like structure is more realistic. The wall-energy calculations can be repeated in this case, and will lead to the same critical size but with stable domains. [81]

We presented two theories, where AF-domain grows continously with decreasing external field. We also noted, that if a domain is coarsened, then it will stay like that unless the sample is (super)saturated. We also know, that the primary domain formation results in a given correlation width of the 'saturation domains'. From the above it follows, that domain ripening will start only, when the theoretical size of the ripened domains reaches the actual primary domain size.

Chapter 8

Domain experiments on the Fe/Cr sample

8.1 Introduction

In the first part of the experiments, we investigated the specular spectra, which corresponded to the $q_x = 0$ specular ridge in the momentum space, showing the plane-perpendicular correlations of the sample. In the last part of the thesis we will deal with lateral structures (in our case mainly domains) of the AF-coupled MLs from experimental point of view. Mangetic domains strictly AF-correlated trough the ML stack give rise to diffuse scattering at Bragg positions (Bragg sheets) as will be detailed later. They can be mapped in q_z = const. scans, which correspond to ω scans in SMR. Domain ripening observed in the easy and hard directions of the fourfold in-plane anisotropy is discussed as well as domain coarsening at the bulk-spin-flop transition.

The physical quantity that we would like to obtain from the off-specular SMR and PNR measurements is the lateral autocorrelation function of the AF domains. In the first Born approximation, neglecting magnetic interface roughness, we obtain the Fourier transform of the domain autocorrelation in the reciprocal space [86].

Magnetic domains in AF-coupled MLs have been investigated by PNR since a long time [67, 68, 87]. SMR can yield the same information for nuclear resonant isotopes (in our case ^{57}Fe). Recently, X-ray Magnetic Scattering has been also utilized to study Fe/Cr MLs [88,89]. The evolution of different techniques leads to a growing competition of measurement methods. We will focus only on PNR and SMR, which were used in our experiments.

As already mentioned, coherent scattering techniques give *direct* information on the magnetic structure. Scattering contributions of structural and magnetic origin separate in reciprocal space for well-chosen conditions. For AF-coupled MLs, this manifest in the appearance of pure magnetic scattering peaks. Those peaks are the result of the unit cell doubling by the alternating AF magnetic ordering of the ML, giving rise to 'half order', structurally forbidden

peaks. Those AF Bragg peaks are of pure magnetic origin.

In this work the majority of our statements is based on SMR scans. The fast development in user environment and beam collimation at ESRF resulted in an increase of an order of magnitude in resonant yield, thus the last taken scans are the most reliable ones.[1] In the future the environment will evolve further by the introduction of on-line sample-height monitor and adjuster. The parameters we measure are the peak heights (from $\theta - 2\theta$ scans) and the diffuse shoulder parameters (from ω scans).

In spite of the different probing depth the PNR results basically matched well with SMR data. In the TOF PNR measurements the sample position is constant thus minimizing the systematic errors stemming from sample 'sliding', but the neutron yield is low, leading to long measurement times and, consequently, to a low number of data sets measured as a function of the external magnetic field. In the following we will discuss the results from the SMR point of view, inserting PNR measurements, where available.

8.1.1 Domain ripening and coarsening as seen by SMR and PNR

In saturation all sublayer magnetizations are parallel to the external field. This forced ferromagnetic alignment ceases with decreasing field, giving rise to domain growth. The evolution of the domains in the high-field region is governed by random processes, due to the mirror symmetry of the magnetic configuration. The net magnetic moment of the AF stack does not depend on the symmetry of the domains (top layer left or right) and the magnetic field lines are shortcut by the AF structure, thus the stray field plays no role. We attribute the patch like domain formation [17] to the distribution of the saturation field and the simple rule of domain wall energy minimization (see Chapter 7).

Both the SMR and PNR measurements confirmed the existence of the strictly correlated AF domains. The domain ripening occurred in a narrow field range of $(0.2 - 0.1\ \mathrm{T})$ in both easy and hard direction loops. We found that domain ripening is an irreversible process, in the sense that the domain size does not change on increasing or reverted fields. This meets our expectations as the ripening involves long-range domain wall movement, thus it is inevitably a dissipative process.

To obtain again the small ('virgin') domain state, the sample has to be saturated, in order to erase all 'domain memory'. Our experiments revealed that 'simple' magnetic saturation was not enough, but a field higher than the apparent saturation must be applied to retain the primary domain state. We call this effect 'supersaturation' effect. The supersaturation field was found in a narrow field range between $1.25 - 1.3$ T, independently of the orientation of the sample (easy or hard direction). The saturation field was less than 1.05 T even for the hard direction loop.

[1] For the sample 990608 the measurements with best statistics and most detailed field dependence were carried out in February and December 2003 at the ESRF ID18 beamline.

The supersaturation effect was investigated in full hysteresis loop to exclude the minor-loop effect.[2] We found that completing the loop by saturation of -1.1 T did not change the domain distribution.

Traditional hysteresis loops are taken along one direction. For AF-coupled MLs with four-fold in-plane anisotropy also a trickier magnetization history is possible. Doing a half-hysteresis loop (up to saturation, then back to remanence) and applying a perpendicular field (in practice by rotating the sample by 90°), the bulk-spin-flop (BSF) transition (see Section 2.5) occurs, inducing a domain *coarsening* (see Section 7.1.6). The majority of the resulting domains were larger than the experimental resolution.

The supersaturation effect was also investigated at low temperature. Starting with coarsened domains the sample was cooled to 15 K in zero field. At this temperature the saturation field was $H_s = 1.55$ T (indicated by the disappearance of the AF Bragg peak), but the supersaturation field was larger than 2.5 T. Lacking sufficient beamtime, it was only possible to establish that the supersaturation field at 15 K was less than 4.07 T. Indeed, having applied this latter field, the lateral correlation function determined from $\omega-$scan in remanence was equivalent to that of the 'virgin' domains.

8.1.2 SMR measurements and sample correlations

The SMR measurements map the sample in reciprocal space. The $\theta - 2\theta$ scans are reflecting the plane-perpendicular structure and correlations, for example the layer thickness and average roughness parameters. The ω scans are basically constant-q_z scans, mapping the off-specular (or diffuse) scattering. The origin of diffuse scattering can be structural or magnetic lateral inhomogeneities.

Rough interfaces

Rough and diffused interfaces lead to the decrease of specular X-ray scattering and appearance of off-specular or diffuse scattering [90–92]. If the applied method is magnetization-sensitive then the magnetic roughness also contributes to the diffuse scattering [86,93]. The distribution of the off-specular scattering in the $Q-$space depends on the plane-perpendicular correlation of the roughness. For uncorrelated roughness, the off-specular scattering is basically the sum of the scattering of the individual layer roughnesses [94], giving rise to diffuse scattering in the whole reciprocal space, while for perfect spatial replication of the interfaces (correlated or 'conformal' roughness [95]) the off-specular scattering will occur at the so-called Bragg sheets (Fig. 8.1), summing up the *amplitudes*, resulting in an intensity higher by a factor proportional to the number of layers [94]. Thus off-specular (ω and longitudinal off-specular) scans reveal

[2] In SMR and PNR measurements normally the hysteresis loops were minor loops. The field was cycled from saturation to remanence and then back to saturation. H. Zabel suggested that the supersaturation is an artefact of the uncompleted (full saturation) cycle.

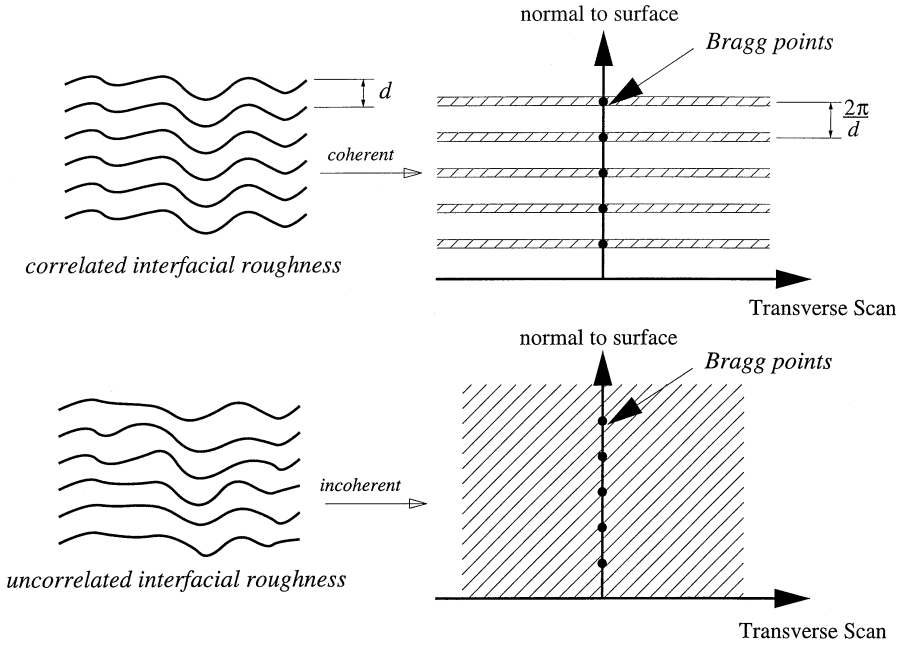

Figure 8.1: Sketch of correlated and uncorrelated interfacial roughness and intensity distribution from the roughness in the reciprocal lattice (after [96]).

the degree of plane-perpendicular correlation and the lateral correlations of the interfaces. From specular scans only the average roughness and magnetization profile can be deduced.

Magnetic scattering

Not only structural roughness breaks the lateral symmetry of the interfaces. Magnetic roughness, as already discussed, also contributes to the off-specular scattering. Magnetic domain formation is also modulating the magnetization-dependent scattering. In general, both magnetic interface roughness and domains give contribution to the off-specular wings [86]. If, however, the interface is uncorrelated, we shall see only the domain information.

8.1.3 SMR scans, slit settings and systematic errors

Before describing the measurement results in detail, we have to discuss the sources of systematic errors. This is important as in our case systematic errors often prohibit the quantitative analysis of the data.

In SMR scans we mapped the momentum space with $\theta-2\theta$, ω and off-specular longitudinal scans (see Section 4.3.4). The $\theta-2\theta$ and off-specular scans were measured in integral mode with 'broad' detector slits, while the ω scans were taken with 'narrow' slits. In the February 2003 shift at ESRF ID18 the 'broad' slit corresponded to 3 mm vertical aperture, which is equivalent to an acceptance angle of[3] $\Delta 2\theta = 2$ mrad, while the 'narrow' slit setting was 0.2 mm, which

[3]From the sample-detector distance (which was calibrated to be 74.48 cm): 1°=26.0 mm on the z-stage.

gives $\Delta 2\theta = 0.13$ mrad. From a previous session[4] it is known that the sample's specular reflection width is ≈ 0.087 mrad at the first AF peak. When measuring with slit setting larger than this value, we do see line broadening due to the inadequate instrumental resolution.

The majority of the $\theta - 2\theta$ scans were taken with broad slits. The horizontal slits were wide enough to integrate along q_y for all scans (see Section 4.3.5). The prompt and resonant $\theta - 2\theta$ scans show a part of the diffuse (off-specular) scattering due to the integral mode measurements.

The longitudinal off-specular scans were also taken in integral mode (broad detector slits) and they contained the specular reflection, too. Consequently, they were not appropriate for deducing the 'pure' diffuse scattering, however, we learned from them that sometimes the so-called specular $\theta-2\theta$ measurements were in fact off-specular ones. The reason is the uncertainty in the angle ω, as the sample stage could move a bit between and during measurements causing small shifts of sample's position and angle. We call this latter effect the θ_0 uncertainty. The θ_0 uncertainity results in systematic errors as it may change the peak ratios. When measuring slightly off-specular then, due to the broad off specular AF wings, the AF peak does not change much while the narrow specular peaks are lowered biasing strongly the peak ratios, as shown in Fig 8.2. The θ_0 and sample stage height instability also resulted in systematic errors concerning off-specular scans. By measuring at wrong q_z positions the $\omega-$scans could be "off-peak", resulting in slightly modified diffuse scattering profile.

Peak ratios in $\theta - 2\theta$ scans

As mentioned above, the $\theta - 2\theta$ scans were done with relatively wide slits. The inclusion of the part of the diffuse scattering means that the height of the AF Bragg peak depends not only on the specularly reflected radiation but the distribution of the off-specular scattering can also have a dramatic effect (Fig. 8.3). The large difference is not so surprising if we take a look at the ω scan at the first AF peak (Fig. 8.4). The partial integration of the wide delayed off-specular wing compared to the narrow structural one causes the huge difference. We will use this 'integral effect' later to study the domain history.

A resonant photon counter would help to normalize the specular and off-specular scattering[5] relative to the number of incident resonant photons per second. The possible energy shifts caused by the displacement of the monochromator crystals and the drift of the sample induced a systematic uncertainty in the absolute resonant yield. Without the possibility of external

[4]The ω scans with highest resolution were taken at session SI-735 (August 2001). The FWHM of the prompt peak did not change much when a detector slit of 0.04 mm ($\Delta 2\theta = 0.026$ mrad) or 0.1 mm ($\Delta 2\theta = 0.066$ mrad) was used. However, the FWHM doubled when the aperture was increased to 0.4 mm. The FWHM with the narrowest slit setting (0.04 mm) of the prompt $\omega-$scan was 0.087 mrad (0.005°) at the AF peak ($\omega = 0.39°$). The delayed FWHM was 0.12 mrad (0.007°) for the same slit setting.

[5]In case of the neutron measurements the normalization is easier as the incoming flux is monitored. In PNR TOF measurements the sample and the detector are not moving, which makes the measurement geometrically more reliable than in case of an SMR scan.

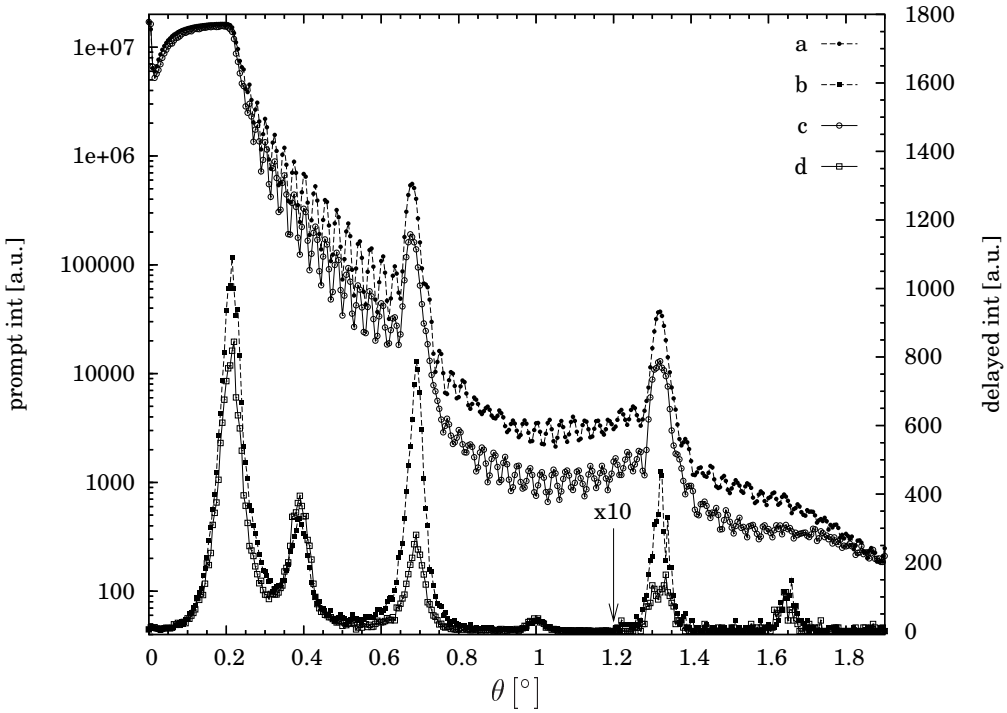

Figure 8.2: The θ_0 uncertainty effect. At the first measurement (prompt c, delayed d) the intensity at the first Bragg peak was too low, thus the experiment was repeated after θ_0 correction (prompt a, delayed b). The intensity of the AF peaks did not change much, while the narrow structural peaks increased enormously. The prompt measurements are plotted on logarithmic scale (left axis) while the delayed curves are shown on linear scale (right axis). Note the $\times 10$ magnification from 1.2° on the delayed data. The scans were taken at ESRF (2003 December). Sample 990608 was measured along an easy axis in transversal setup. The preceding field history was 4 T $\rightarrow \ldots \rightarrow$ 0 T $\rightarrow$ 0.3 T. The measurements were taken in 0.3 T.

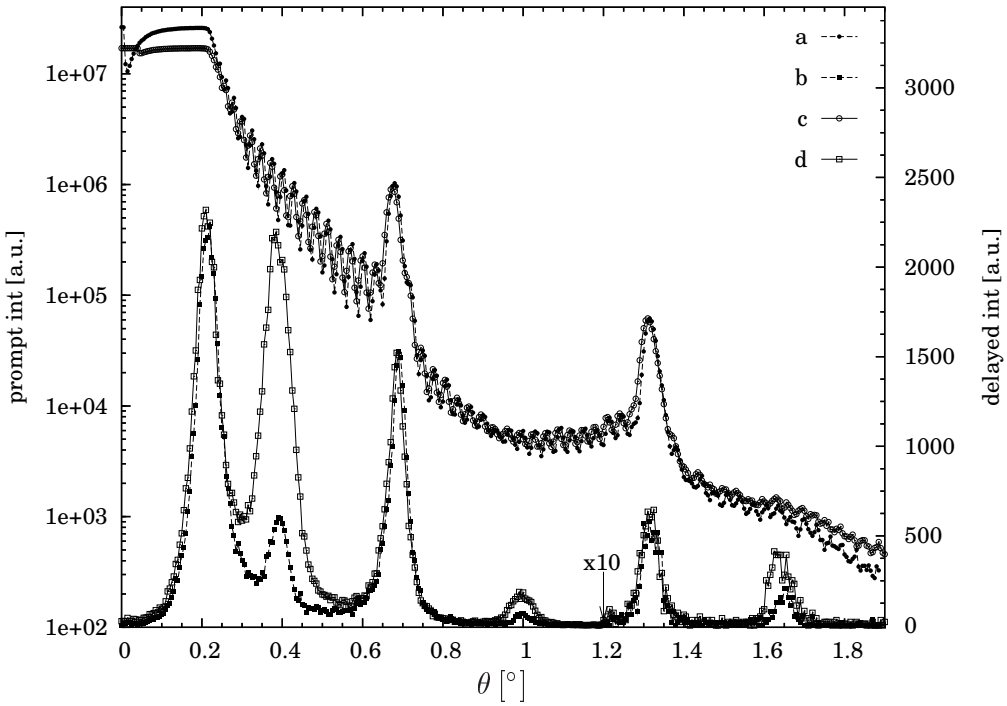

Figure 8.3: Effect of the integral mode scan. The prompt of the $\theta - 2\theta$ scan with narrow slit (a) was normalized to the prompt of the wide slit scan (c). The normalization was made by a signal obtained with a detector after an Al plate to avoid detector saturation (not shown in the figure). The delayed curves show the enhancement of the magnetic Bragg peaks in the case of broad detector slits (d) compared with the narrow slit setting (b). The narrow slit was 200 μm, while the broad slit was 2 mm wide. For scale axes see the comments in Fig. 8.2. The scans were taken at ESRF (2003 December). Sample 990608 was measured along an easy axis in transversal setup. The preceding field history was 4 T $\rightarrow \ldots \rightarrow$ 0 T. The measurements were taken in remanence.

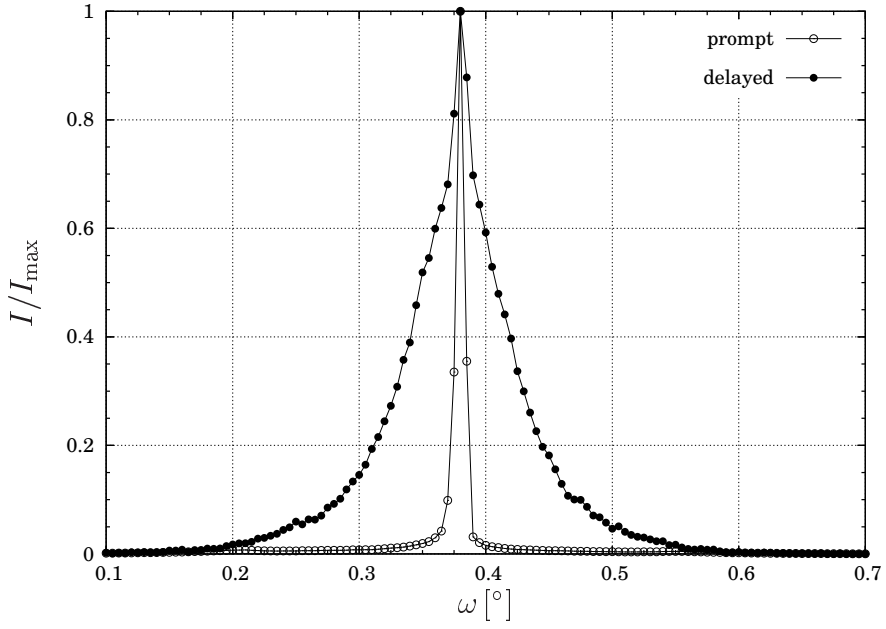

Figure 8.4: ω scan on the first AF Bragg peak ($\theta = 0.38°$) in zero external field, easy direction.

normalization, the measured curves had to be normalized intrinsically.

The 'data mining' included integration of all resonant peak areas (total reflection, structural and AF Bragg peaks) in the SMR scans and the tabulation of peak heights. For analysis mainly the peak areas were used because in some cases the peaks were broad with two maxima. The conclusions did not change essentially depending on the height or area selection. In some cases an alternative approach of linear combination of spectra was used. This gave again qualitatively the same result.

Gathering magnetic data by comparison of peaks is possible only if the information is 'localized' to given regions. The existence of AF peaks is the direct consequence of the magnetic 'unit cell' doubling. On the other hand the magnetic structure itself influences the scattering in general. For our particular measurement setup we have seen no change of the scattering with the changes of the magnetization angles at the first structural Bragg peak. This is a consequence of the particular geometrical setup (see Sec. 4.1.3).

The appearance of AF peaks in TISMR spectra and the absence of magnetic sensitivity at the structural peak has consequences on the off-specular reflectivity, too. It implies that the consecutive magnetic layers are strictly AF correlated through the ML [6]. If it were not the case then, as it was observed for weakly coupled Co/Cu MLs by Borchers *et al.* [97] the AF peak would disappear.

In the following we will use the area of the Bragg peak to normalize the spectra based on the previous theoretical and following practical considerations, assuming that it contains only structural information but not magnetic:

1. The resonant $\omega-$scans taken at the structural Bragg peak in low (7 mT) and high (1 T) external field showed identical peaks, while the $\omega-$scan at the first AF peak had no off-specular scattering (see Fig. 8.5) at high fields.[6]

2. The $\omega-$scan at the structural Bragg peak was the same for the prompt and delayed photons (except for the norm. factor) independently of the sample condition (temperature, external field). See Fig. 8.6.

Finally we note, that by analysis of $\theta-2\theta$ scans taken with broad and narrow slit, magnetic scattering was found only at the AF peaks.[7] This means, that in principle the total-reflection peak could also be used for normalizing the peaks. In practice it is not a good idea, because of the systematically changing footprint correction.

[6] In 1 T we measured at the possible 'AF position', as no AF peak was present.

[7] Normalizing to the prompt yield, the broad-slit and narrow-slit curves were compared for a whole loop (in easy direction of SI-962.)

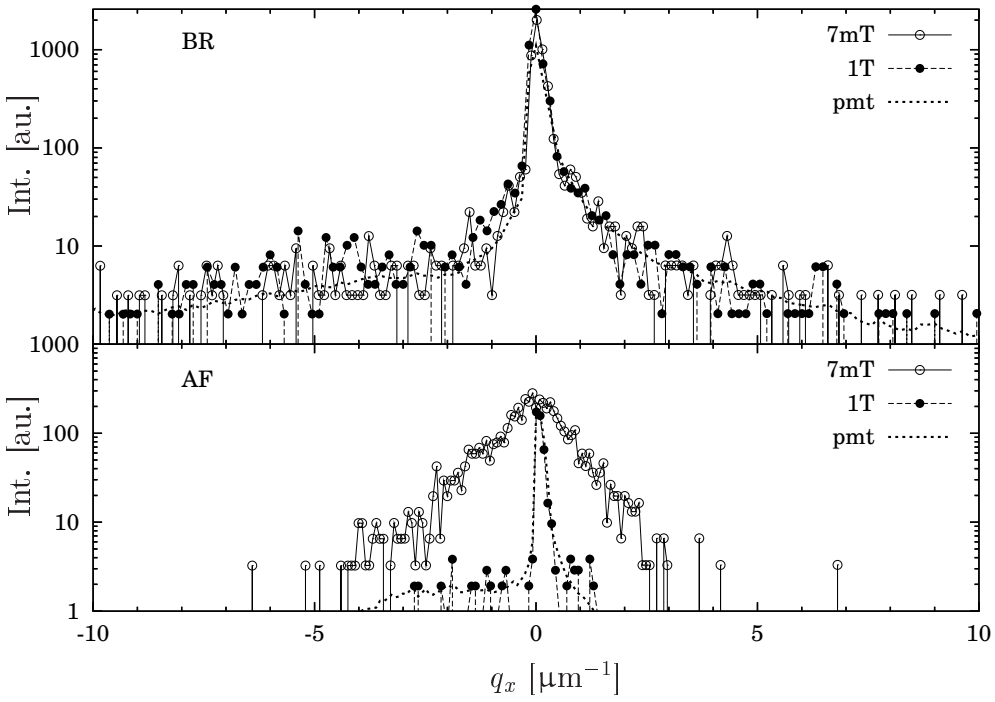

Figure 8.5: The first AF and first structural Bragg peaks in easy direction. The AF resonant off-specular intensity changes with field while the Bragg peak is 'constant' and coincides with the prompt off-specular scan. The scans were taken at ESRF, session SI-508b (July 2002). The intensity was scaled to the specular channel.

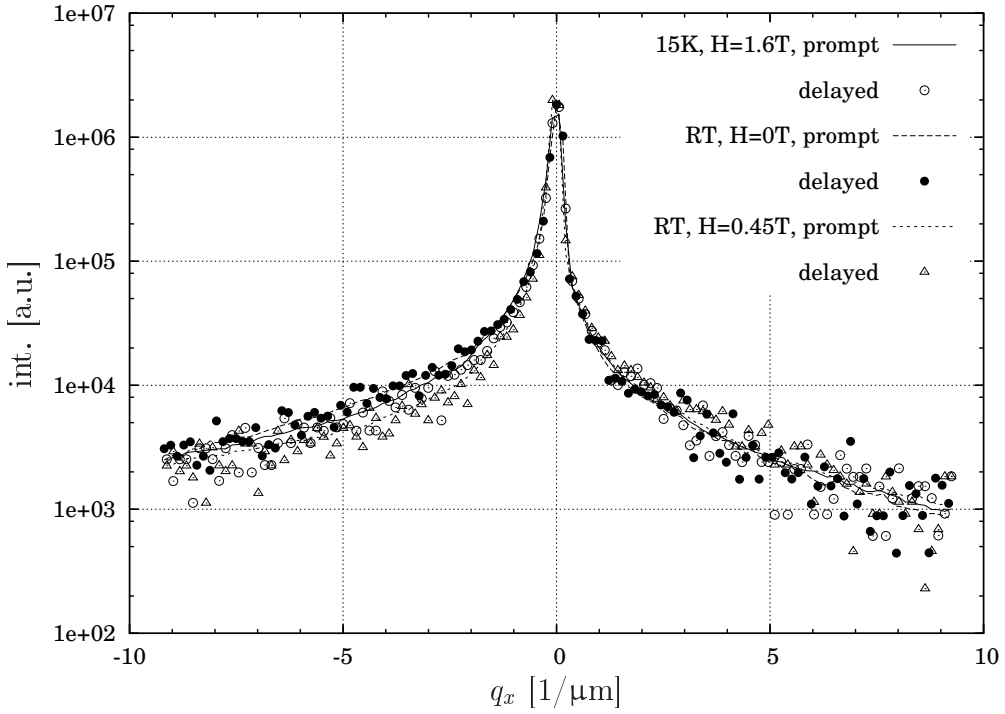

Figure 8.6: ω scans at the first structural Bragg peak at different parameters. The prompt (lines) and delayed (points) data are scaled to a common curve. The scans were taken at ESRF, session SI-962 (December 2003).

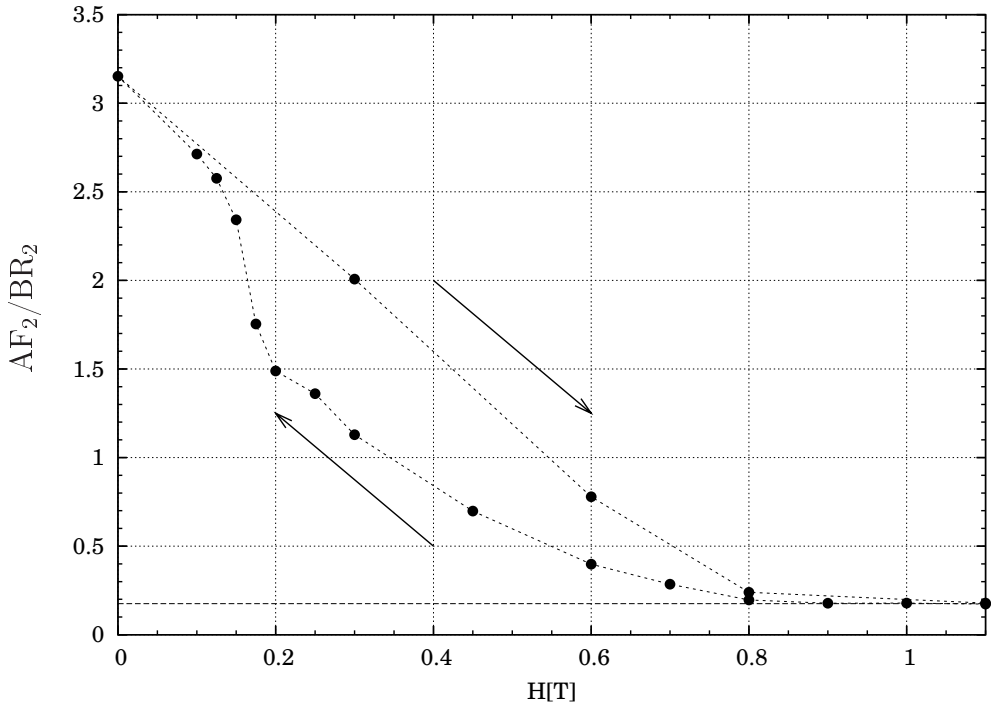

Figure 8.7: Peak integral ratios of the second AF peak divided by the second structural peak. The integrated regions in degrees: AF_2 $[0.9 - 1.1]$, BR_2 $[1.2 - 1.45]$.

8.2 Domain ripening

Domain ripening is the process, when the average domain size grows from its 'native' (just below saturation) state to the zero-field equilibrium size (see Chapter 7). We performed SMR and PNR measurements to study the details of the change of the domain size distribution. Similar measurements were previously done by PNR on AF-coupled systems (see for example [72, 76] and further references in [67]) but the present SMR study is the first thorough and systematic investigation of the domain evolution process.

8.2.1 Easy direction

The SMR mapping of domain transformation in easy direction was one of the first of our off-specular synchrotron measurements (ESRF, SI-735, August 2001). The feasibility of off-specular scanning was demonstrated in earlier shifts (SI-508, July 2000; SI-618, December 2000) but at that time the brilliance of the beam did not allow for systematic investigation with acceptable count rate. The easy-axis loop was repeated in December 2003 with much better statistics (session SI-962). Here both $\theta - 2\theta$ and $\omega-$scans were taken. Starting from well above saturation ($H_{\text{max.}} = 4.065$ T) the field was lowered to 1.2 T and then $Q-$space mapping was done. Reducing the external field step by step, the domain history was scanned.

From the $\theta - 2\theta$ scans with wide slits [81] we see an irreversible domain ripening[8] (Fig. 8.7).

[8] In the SI-962 session $\theta - 2\theta$ scans up to the third structural Bragg peak were taken. In principle all three

The AF peak rises sharply below $H = 0.2$ T and when the field is increased again, the peak ratio stays well above the field-decrease branch.

From the $\omega-$scans the domain ripening can be investigated in details. The intensity of the diffuse scattering is proportional to the 'roughness', while the form of the function correlates with the in-plane magnetic structure. We will not analyse quantitatively the intensity of the off-specular scans as yet, no proper theory of the diffuse SMR is available and the geometrical uncertainties give too much error on the absolute yield.

The intensity of the off-specular scattering depends on the magnetic 'contrast', which contains not only the autocorrelation function of the in-plane magnetization, but also the angle difference between the neighbouring domains. At high external fields the angle difference and thus the magnetic diffuse scattering at the AF peak is small. To be able to compare the autocorrelation functions, we normalized the off-specular parts to the shoulder next to the specular peak.

In Fig. 8.8 the $\omega-$scans in decreasing field (after supersaturation) are collected down to 0.2 T. From earlier measurements[9] we already expected the ripening to occur in a small field range starting at 0.2 T, thus we took larger steps in the upper magnetization region. The normalized $\omega-$scans are identical, showing no change in the shape of the off-specular scattering. The curve at 0.2 T shows a small ripening, but we attribute it to systematic errors (integral of the off-specular peak is anomalously low, the previously taken $\theta - 2\theta$ scans with broad and narrow slit are the same, indicative of a badly aligned sample).

As expected from earlier easy- and hard-axis SMR measurements, the ripening is completed at $H = 0.125$ T (Fig. 8.9) and further decreasing the field does not change the shape of the off-specular scattering. The ripening is an irreversible process, as we discussed earlier and here the experimental evidence is shown. When the field was increased (Fig. 8.10) only the amplitude of the off-specular scattering decreased, but the shape of the scattering remained unchanged. Also scanning the field below saturation (for example 0 T $\rightarrow$ 0.3 T $\rightarrow -0.1$ T $\rightarrow$ 0 T) did not change the form of the off-specular scattering.

PNR measurements

The PNR experiments confirmed the existence of domain ripening. Due to the short available measurement time the spin analyzer was not used. This was possible because the sample alignment was such[10] that only spin-flip scattering was present in the AF Bragg sheet. This was confirmed by short-time, low-statistics measurements with spin analysis at 0, 0.15, 0.3 and

structural/AF peak ratios should give the same information. We found that due to geometrical effects, the usage of higher order pairs gave less instrumental errors (at lower angles the θ_0 and sample height uncertainty plays a bigger role). On the other hand, at too high angles the resonant count rate is not high enough for reliable comparison. For this sample the second Bragg and AF peak were the best choice.

[9] ESRF shift SI-735, August 2001.

[10] The layer magnetizations were perpendicular to the spin on the impinging neutron beam.

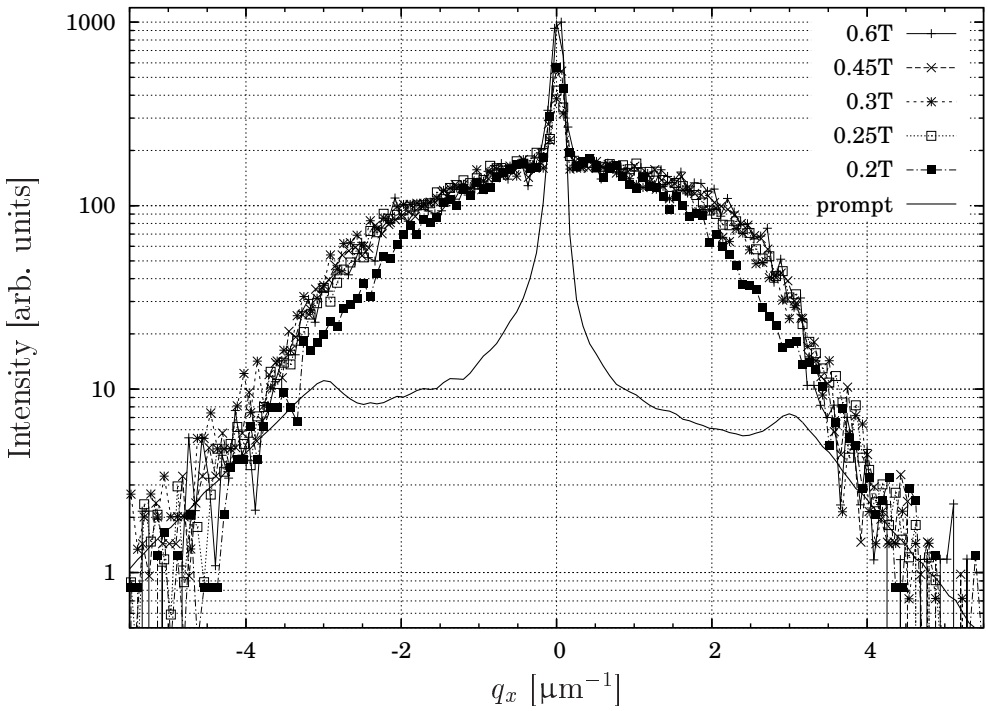

Figure 8.8: ω scans on the first AF peak in decreasing field after supersaturation. The measurements were normalized to the off-specular shoulder at the specular peak.

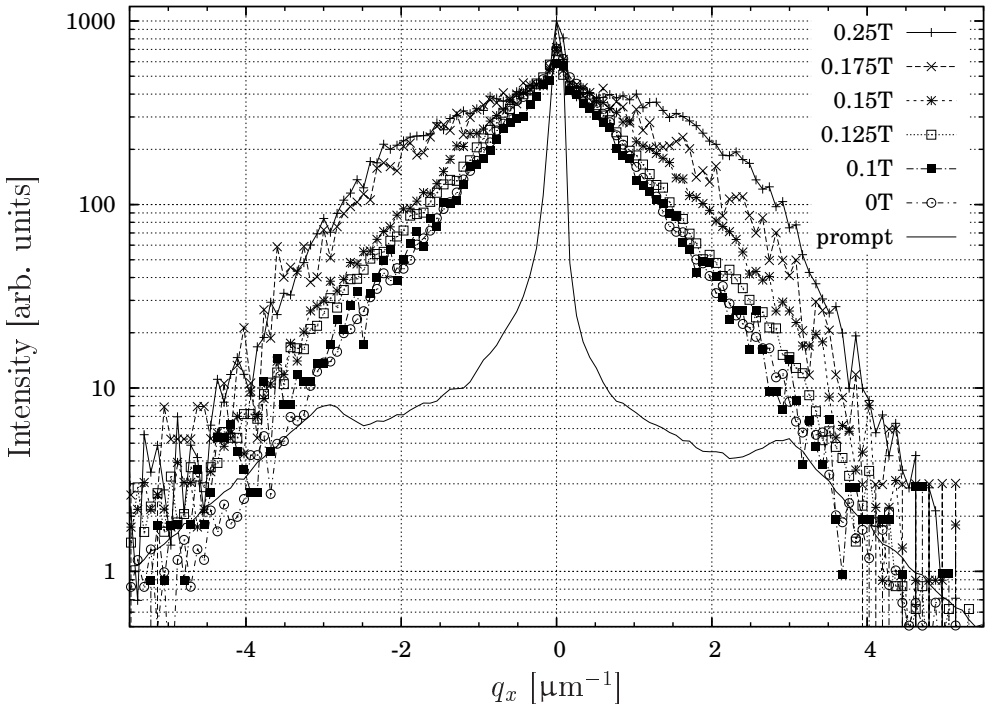

Figure 8.9: ω scans on the first AF peak in decreasing field. The measurements were normalized to the off-specular shoulder at the specular peak. We used the $H = 0.25$ T as first value, because the $H = 0.2$ T scan was taken with badly aligned sample.

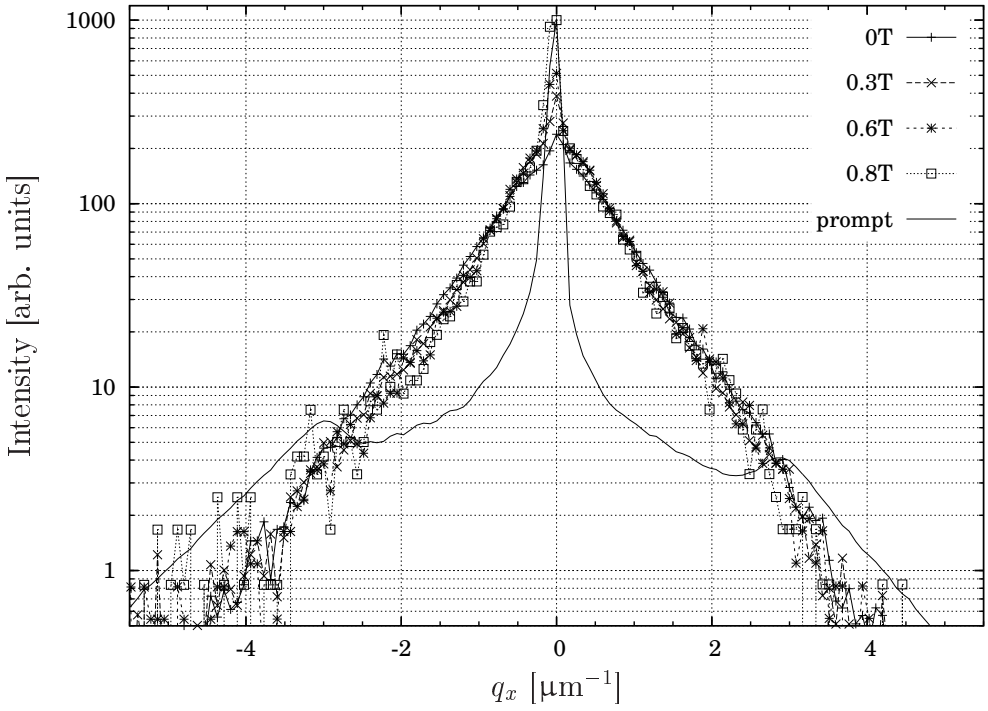

Figure 8.10: ω scans on the first AF peak in increasing field. The measurements were normalized to the off-specular shoulder at the specular peak.

0.45 T and was expected from previous BSF experiment [6]. In Fig. 8.11 the results with active spin flipper (the negative channel) are seen. They do not differ from the results obtained in the positive channel (flipper inactive).

For comparison with SMR $\theta - 2\theta$ and ω measurements, the two-dimensional neutron measurements were integrated along the q_x and q_z axes, respectively. In the specular scans (q_x integrated) (Fig. 8.12) we see that the AF peak grows with decreasing field to the maximal value in remanence. The largest jump is between 0.3 T and 0.15 T. If comparing the branches of decreasing field to those of increasing field, then we see that the peak is higher at increasing field. Reducing the field a second time to 9 mT gives identical scattering to the first maximum. The above behaviour is consistent with the domain ripening shown by the SMR. From the off-specular figure (Fig 8.13) the domain distribution can be mapped. We show the primary domains at 0.3 T and the domain state after ripening (9 mT). The domain fits will be described later.

Supersaturation

Ripening is an irreversible process. We call irreversibility the fact that in increasing external field the once ripened domains are not shrinking back. The only way to get back the primary domains is to supersaturate the sample. The supersaturation effect was investigated by SMR. The first evidence of supersaturation was gathered after the BSF transition (Fig. 8.14). At that time the ripening effect was unknown, thus the spectra were taken in remanence. A sharp

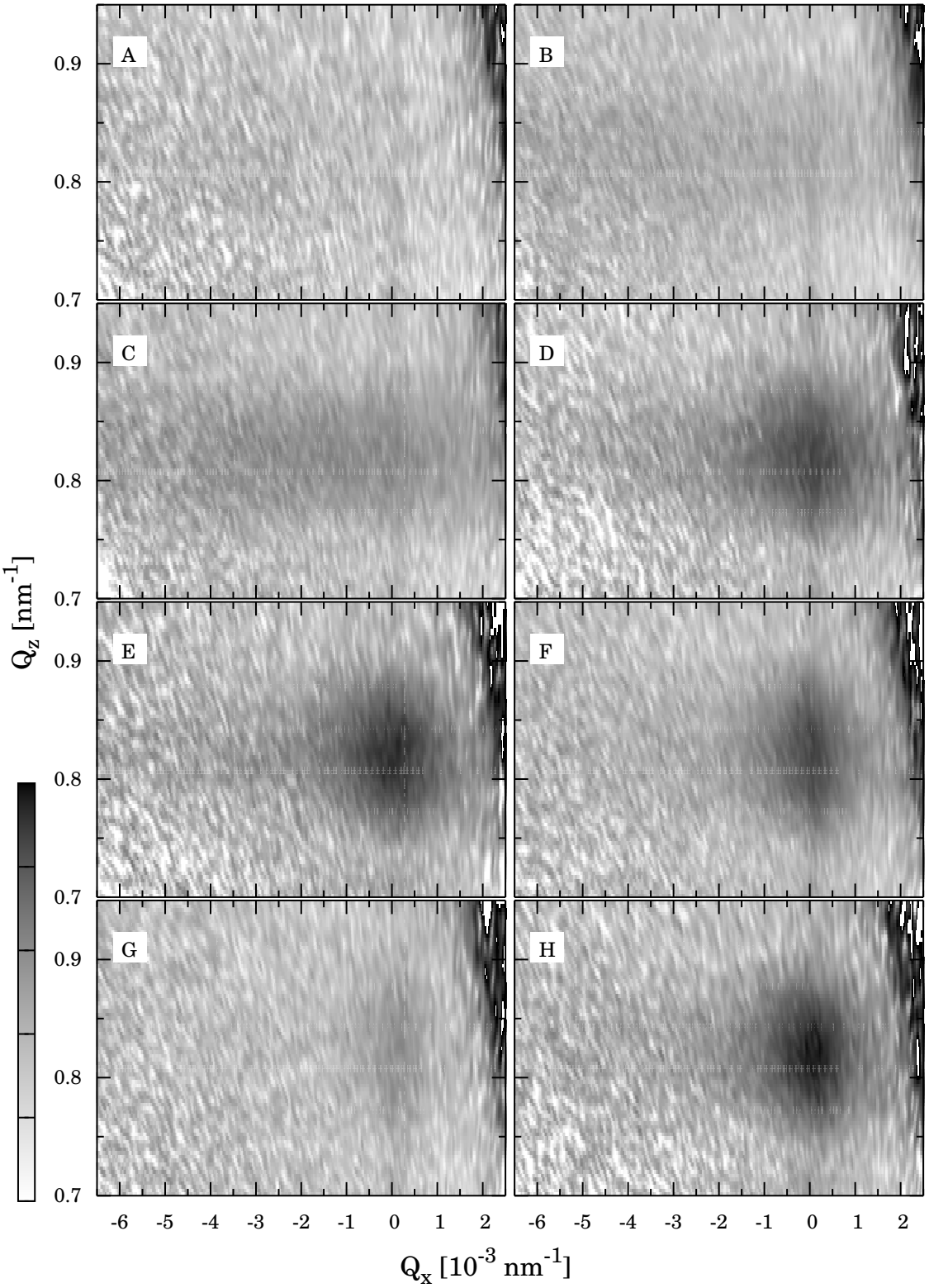

Figure 8.11: Polarized neutron measurements at the first AF peak with no spin analysis. Negative channel (first spin flipper active). After supersaturation the field was released to *A*: 0.6 T, *B*: 0.45 T, *C*: 0.3 T, *D*: 0.15 T and *E*: 9 mT. Increasing the field, *F*: 0.3 T, *G*: 0.6 T, and again to remanence: *H*: 9 mT. The 'grey' axis is logarithmic. The measurements were done on the reflectometer REMUR at IBR-2, Dubna in January, 2003.

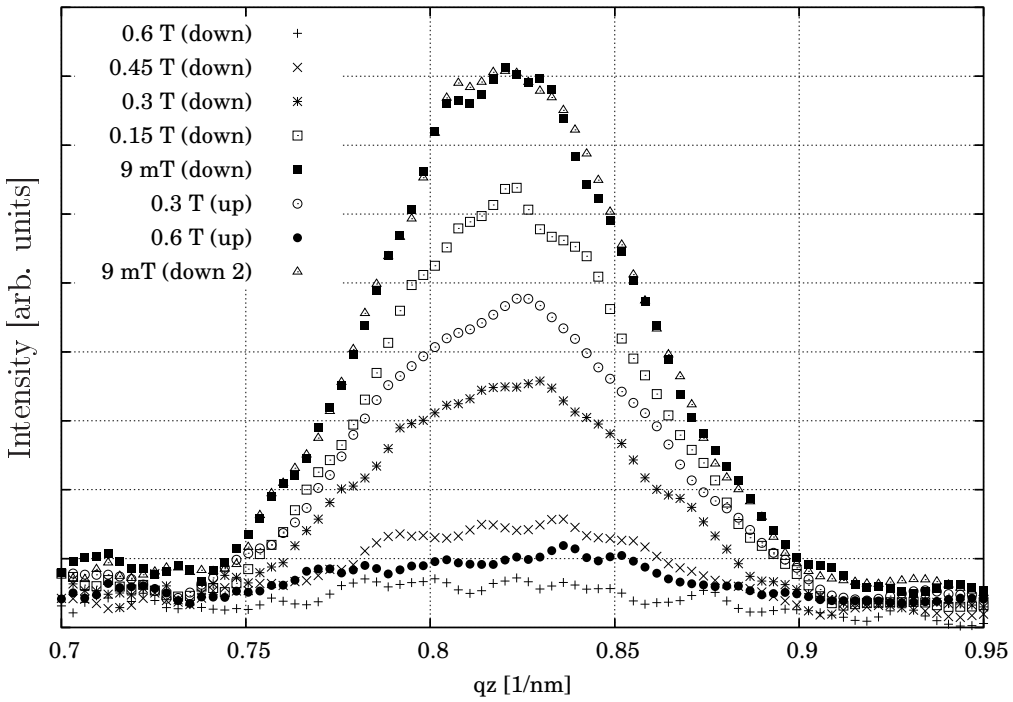

Figure 8.12: PNR measurement at the first AF peak integrated along q_x. The integration region was [-6:1.2] 1/µm.

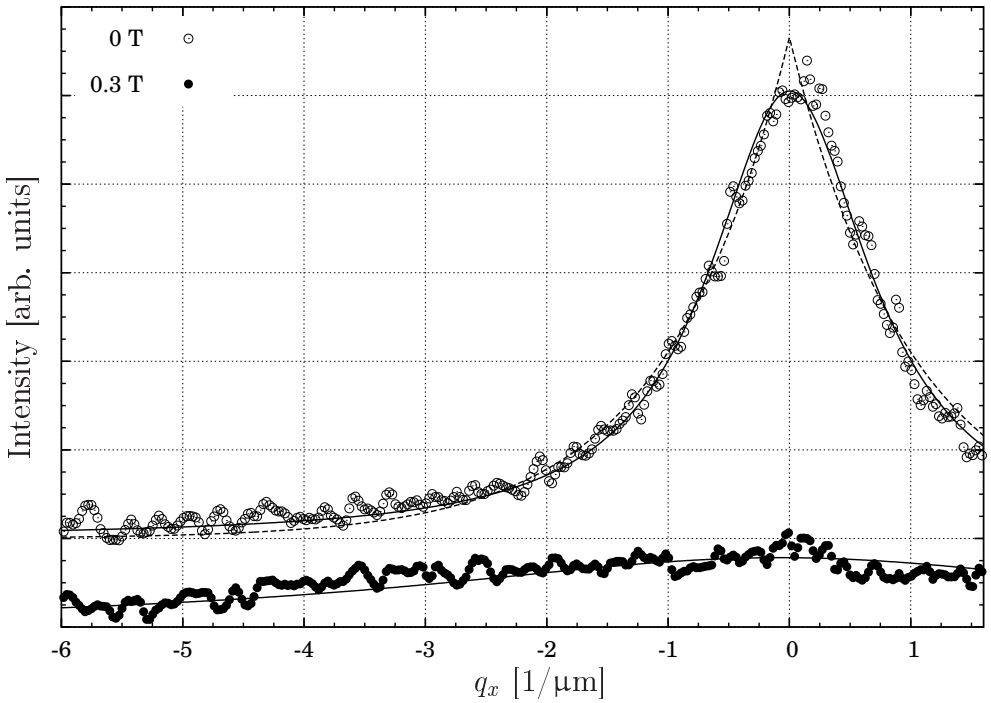

Figure 8.13: PNR measurement at the first AF peak integrated along q_z. The integration region was [7.5:9] nm^{-1}. The solid lines are Lorentzian fits with $\xi = 0.272 \pm 0.009$ µm (0.3 T) and $\xi = 1.23 \pm 0.01$ µm (0 T), respectively. The dashed line is an exponential fit with $\xi = 0.989 \pm 0.013$ µm. For definition of ξ see 8.3.

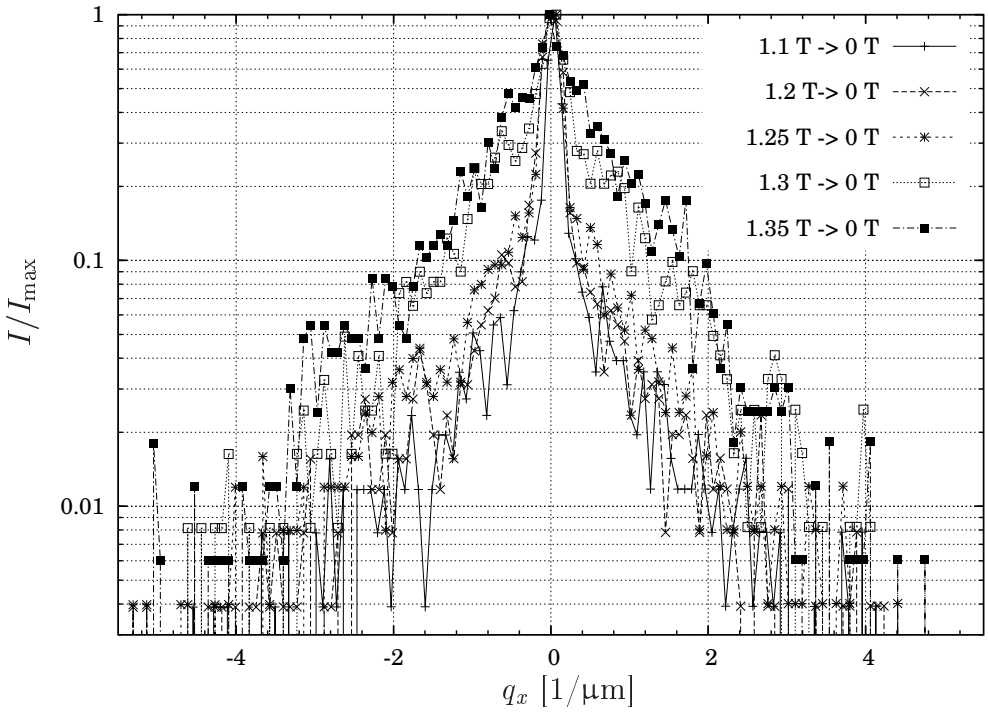

Figure 8.14: Easy direction supersaturation measured after domain coarsening (SI-618, December 2000). The $\omega-$scans were measured in zero external field. Change in the off-specular scattering at 1.3 T can be seen.

change between 1.25 T and 1.3 T is obvious from the $\omega-$scans.

In the following we will show that the domains are also not changing shape in the case of continuation of the magnetization loop, thus the supersaturation effect is not a 'minor loop' effect.[11] After decreasing the external field from supersaturation (actually from 4 T) to zero, the irreversibility of the domain shape was first shown in positive direction (up to 1.1 T), then at -1.1 T. The actual ω scans were taken at 0.5 T and -0.5 T, respectively. As can be seen in Fig. 8.15, the domain shape did not change. By decreasing the field to -1.2 T (curve e in Fig. 8.15), we reach the supersaturation region. This field is a bit lower, compared to previous results, but still higher than the sample's saturation field in easy direction.

8.2.2 Hard direction

In hard-axis setup the domain 'engineering' again stared from the supersaturated state. In this state all Fe moments are aligned parallel to the external field. Mapping the peak ratios in the $\theta - 2\theta$ scans helped to find the domain-ripening region. On Fig. 8.16 the linear combination of the maximal and minimal AF peak spectra is shown. This gives qualitatively the same

[11] Magnetization loops are traditionally taken from positive saturation to negative saturation and back. In the majority of SMR and PNR measurements we took the loop from supersaturation to remanence and back. As the domain ripening is connected with domain wall movement, which is a friction-like process, no domain breaking should occur when the magnitude of the external field is increasing, independently of its direction.

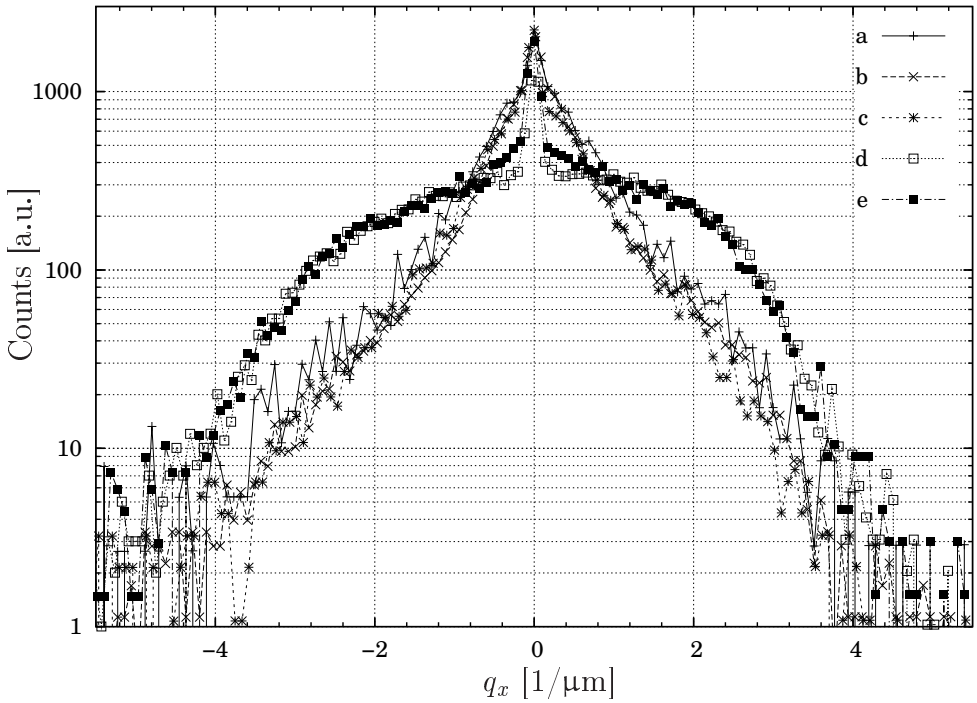

Figure 8.15: Easy-direction domain-ripening cycle. The sample was first supersaturated in 4 T, then the field was released to zero, then $H_{\text{ext}} = 1.1$ T was applied, afterwards reduced to $H_{\text{ext}} = 0.5$ T where the first $\omega-$scan was measured *(a)*. To check the direction-independence of the domain ripening, a negative field of $H_{\text{ext}} = -1.1$ T was applied, and the $\omega-$scan measured at $H_{\text{ext}} = -0.5$ T *(b)*. The previous two scans show the same domain properties as that, measured on the sample in $H_{\text{ext}} = 0.6$ T increasing field from remanence *(c)*. To compare the ripened domains with the small-domain state, the $\omega-$scan prior to ripening at $H_{\text{ext}} = 0.45$ T *(d)* (coming from supersaturation) is compared with the continuation of *(b)* by applying $H_{\text{ext}} = -1.2$ T, then measuring at $H_{\text{ext}} = -0.5$ T *(e)*.

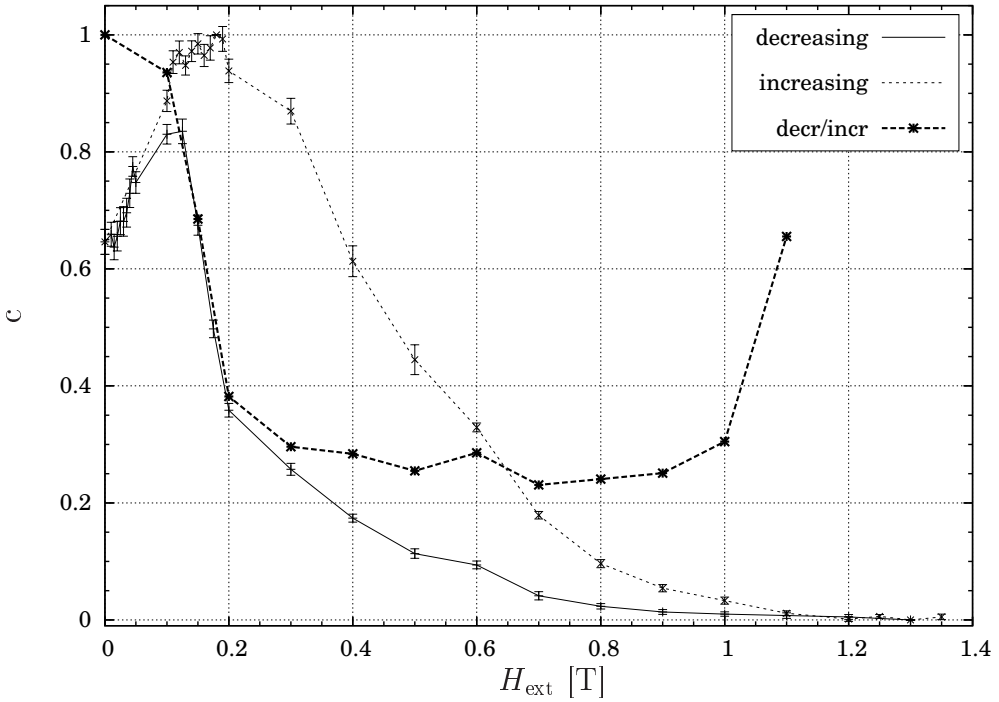

Figure 8.16: Linear combination of hard direction $\theta - 2\theta$ scans. After supersaturation in 4 T, the field was decreased to 0 T then increased to 1.35 T. The *decr/incr* curve show the decreasing c values divided by the increasing c values. The ponts above 1.1 T are not shown.

result as the peak ratio, but takes into account more data points.[12] The saturated spectra by definition will mean $c = 0$, while we found the maximal peak at increasing field of $H = 0.18$ T, defining it as $c = 1$. All other spectra are fitted as the linear combination of the previous two extrema. The linear combination method has the advantage of showing no 'residual shoulder' at saturation.[13]

We again see a sharp increase starting from 0.2 T and reaching maximal peak value at decreasing field of 0.125 T. In remanence the AF peak is smaller, because the magnetizations are aligned along the easy axes, which are located at $\pm 45°$ relative to the fields direction. When the field is increased, the domains are staying in the ripened state, resulting in maximal peak intensity at ≈ 0.18 T. The saturation is around 1.1 T. The constant decreasing/increasing branch ratio in the field range of $0.2 - 1.0$ T strongly suggests that the primary domains do not change shape down to 0.2 T. In accordance, investigation of the ω scans shows no change in line shape down to 0.2 T. As shown in Fig. 8.17 in saturation we see no difference in the prompt and delayed diffuse scattering around the specular part. When the field is lowered, only the intensity of the magnetic diffuse scattering changes, but not the line shape. We attribute this change to the changing domain angle.

Lowering the external field further in hard direction the domain ripening can be observed

[12] In the SI-847 experiment (Feb. 2003) the scanning range stopped at the second AF peak, thus the AF_2/BR_2 ratio could not be calculated.

[13] No field-dependent PNR measurements were made in hard-direction setup.

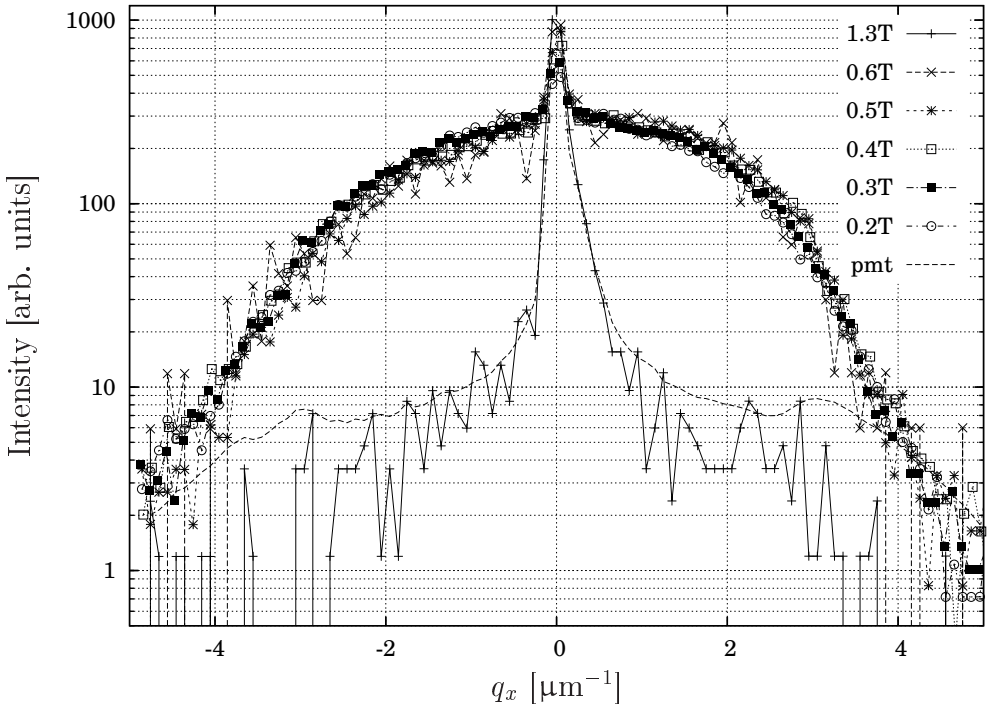

Figure 8.17: Hard-direction ω scans in decreasing field after supersaturation. The measurements were normalized to the off-specular shoulder at the specular peak. Above saturation the diffuse resonant scattering coincides with the prompt (labelled pmt), except for the Yoneda peaks.

between 0.2 T and 0.125 T (see Fig. 8.18). The ripened domains do not change when the field is lowered further to remanence from 0.1 T. At increasing fields the shape is not changing, just the diffuse intensity is getting lower.

Supersaturation

When the sample is in saturation ($H \geq H_s$) then the AF peak vanishes, thus no direct information can be obtained from it.[14] In order to detect the domain transformation around saturation the field was lowered prior to measurement to 0.5 T (to be above the critical field for domain ripening) where AF scattering is already measurable. The maximal field to be investigated was increased in small steps from measurement to measurement. This way, the supersaturation 'memory effect' was mapped. According to the measurements, in hard direction the domains are transformed back to the 'virgin' (small domain) state in a narrow field range between 1.20 and 1.25 T (Fig 8.19). This is the same field range, where the easy direction supersaturation was observed.

[14]The diffuse scattering, still present, is proportional to the prompt ω scan (see for example Fig. 8.17), giving only structural information.

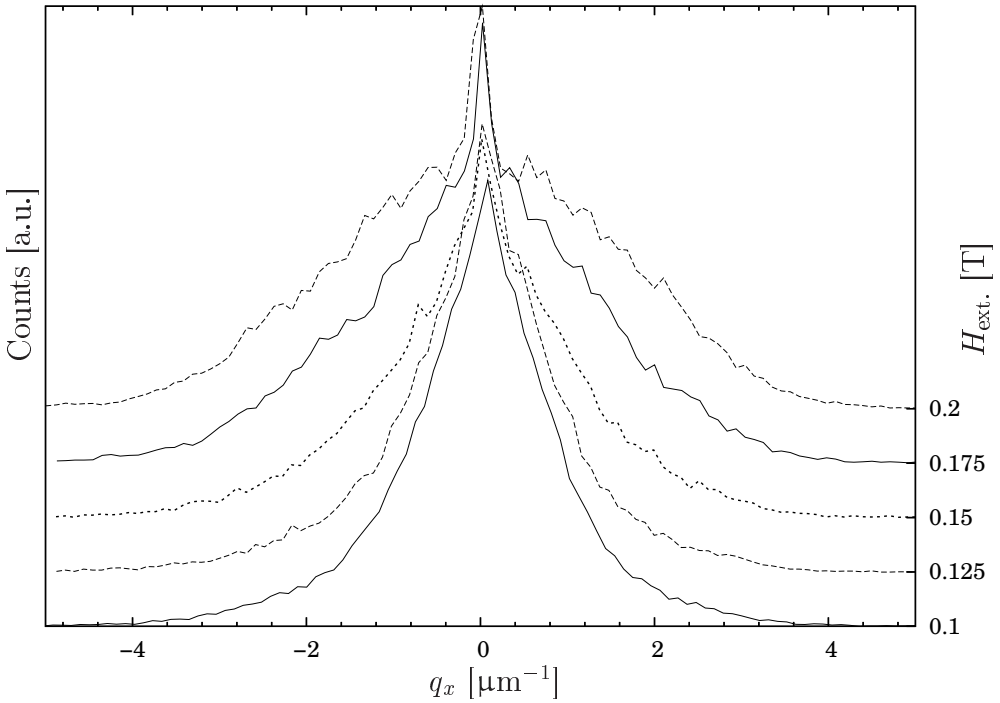

Figure 8.18: Domain ripening in hard direction. The curves are shifted for clarity. Below 0.1 T, the spectrum does not change.

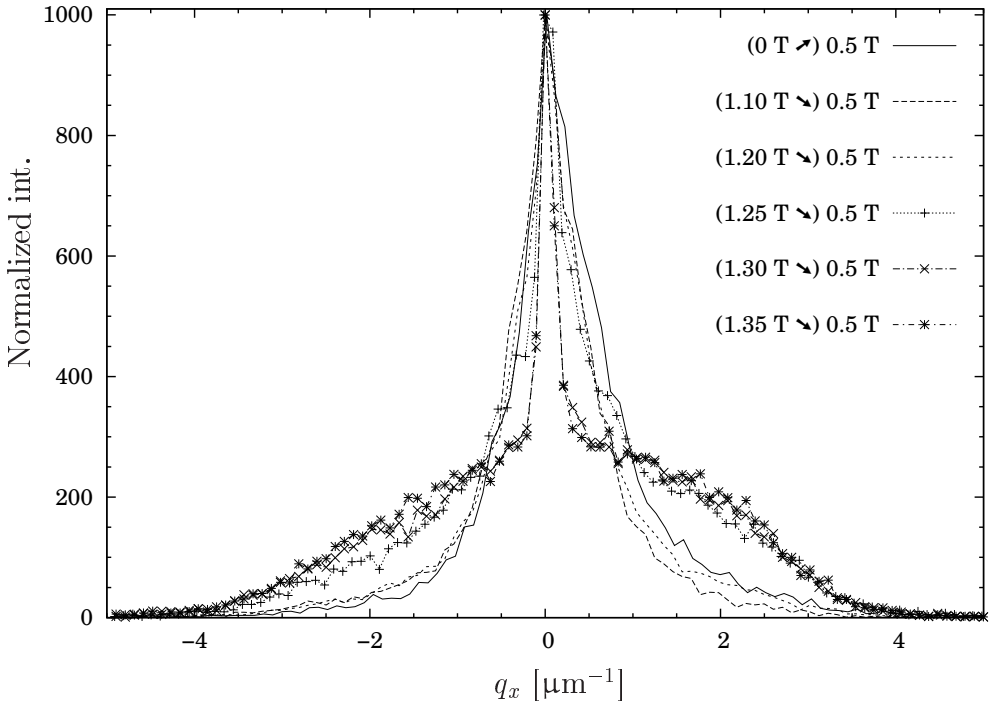

Figure 8.19: Detection of supersaturation in hard direction. The scans were measured in 0.5 T. The field value in brackets is the last field seen before the measurement.

8.3 Domain history at low temperature

The supersaturation effect was also demonstrated at low temperature, in easy direction (SI-962, December 2003). After two consecutive spin-flop transitions at room temperature, the sample was cooled to 15 K. By looping the external field step by step to higher and higher values and measuring $\theta - 2\theta$ scans in-field, and $\omega-$scans in zero field the saturation field was scanned and the supersaturation investigated.

Due to the spin-flop, in remanence the sample was in the 'large domain' state [6]. By increasing the external field the AF moments were forced to rotate towards a ferromagnetic alignment. The saturation field was ≈ 1.5 T (Fig. 8.20). To be sure to include all off-specular scattering, the vertical detector slits were wide open[15] (± 3 cm). After reaching saturation, $\theta - 2\theta$ and ω scans were taken in $H_{\text{ext}} = 0$ T. The shape of the ω scan suggests that at this temperature the sample did not go trough the ripening process even in remanence. Increasing the field loop up to 2.5 T no differences were detectable on the ω scans (Fig. 8.21). The field of 4 T was high enough to return the sample to the 'small-domain' state. Indeed, from the ω scan (Fig. 8.21) it seems that the sample returned to the 'virgin' state.

To obtain domain properties from integral (wide-slit) $\theta - 2\theta$ scans the peak ratios should be evaluated. As already discussed, integration of peak areas and linear-combination fitting of spectra are both yielding similar result. Here we will use the linea-combination fitting method. In saturation, the AF peak disappears while it is maximal in remanence. By defining the AF/BR ratio to be 0 in the forced FM alignment ($H_{\text{ext}} = 1.7$ T) and 1 in the AF alignment ($H_{\text{ext}} = 0$ T) and fitting the $\theta - 2\theta$ scans in between with a linear combination of the two extreme scans a good AF/BR ratio plot was obtained (Fig. 8.20). One can achieve an even better result, if only the higher-angle part of the scans is used. The cause for this may be the changing misalignment of the sample, which influences the spectra trough the geometrical effects[16]. The peak ratios could be also biased by not scanning exactly along the specular ridge. Those systematic errors are getting smaller at higher angles.[17] On Fig. 8.20 curve (a) shows the results obtained by fitting the spectra starting from the first structural peak (BR_1), while in case of (b) the fitting was done on the first AF peak (AF_1) to the first structural peak (BR_1) range. From the reduced χ^2 it is also evident that the model of linear combination is better for case (a). Note that in this case the intensity of the first AF peak can differ from the measured value.

[15] This slit setting is probably wider, than the whole active area of the detector.

[16] This is the reason why the total-reflection peak has never been included in the fit.

[17] The unexpected decrease at 0.4 T is also connected to sample alignment and it is missing in the higher-angle fit.

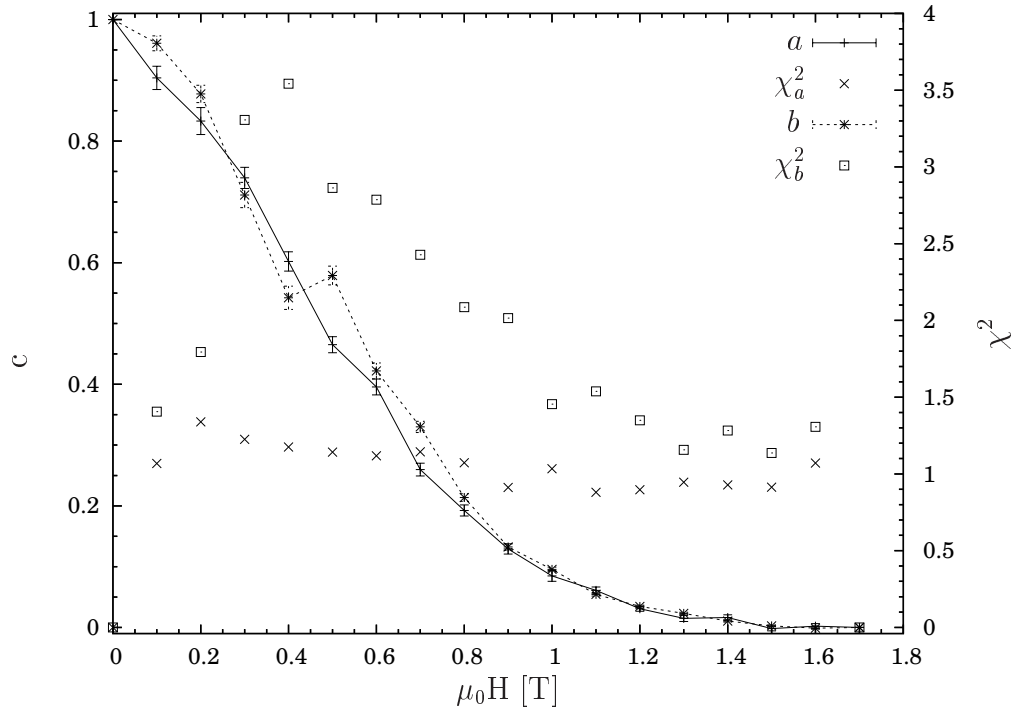

Figure 8.20: The AF/structural peak ratio of the low temperature (15 K) easy direction $\theta - 2\theta$ scans after domain ripening in increasing external field. In case (a) the fit was done in the [BR_1:BR_3] range ([0.6° : 2.1°]), while (b) was fitted only for [AF_1:BR_1] range ([0.3° : 0.9°]). The reduced χ^2 is also shown as χ^2_a and χ^2_b, respectively. For detailed analysis see text.

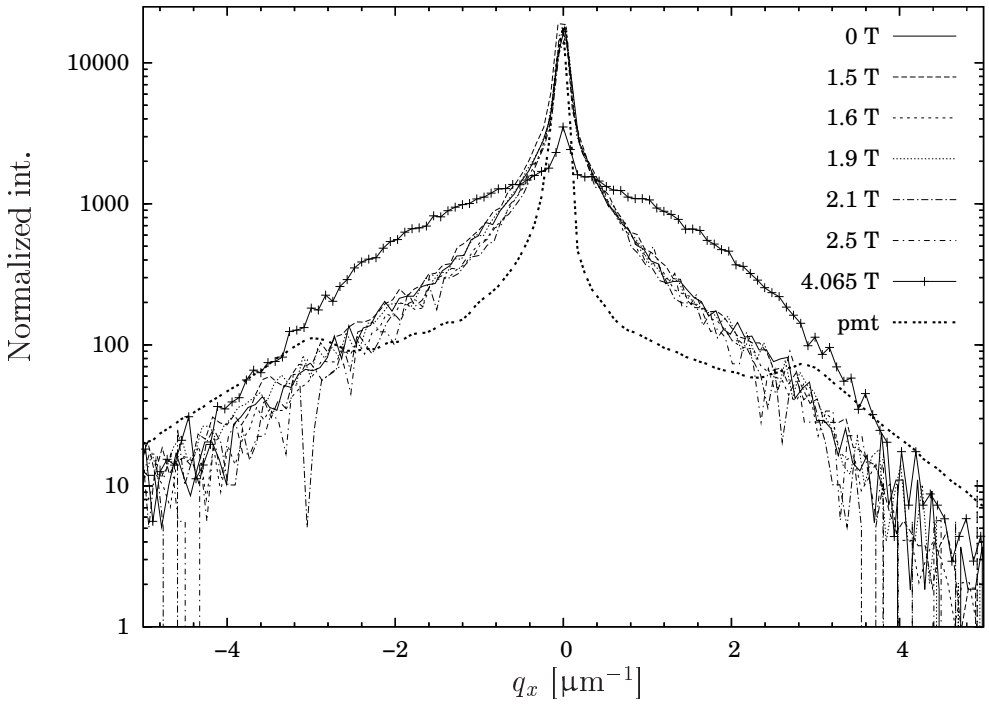

Figure 8.21: Low-temperature (15 K) supersaturation in easy direction. All curves are normalized to 10 s/ch prompt counts. No notable difference can be seen up to 2.5 T. Lacking beamtime, the supersaturation region was not searched further, thus only 2.5 T $< H_{\text{sup. sat.}} <$ 4.065 T could be established.

8.3.1 Discussion

The PNR and SMR measurements revealed us the details of the domain ripening in easy and hard direction. Domain ripening is not a continuous process but it is occurring in the narrow decreasing field range of $0.2 - 0.125$ T after supersaturation. Ripening is irreversible, the domains do not change on increasing the field up to supersaturation. The supersaturation region is again a narrow field region of $1.25 - 1.3$ T. Ripening and supersaturation occur in the same way for easy and hard direction loops (same field ranges, same $\omega-$scans), thus it seems that anisotropy plays no role in those phenomena. At 15 K the supersaturation is even more pronounced and no ripening occurs. Finally, the non-continuity of ripening is not an artefact of the SMR scans, as PNR scans confirm our findings.

Domain size

Now we would like to answer the following question: How big are the AF domains? We used reciprocal-space measurement methods, thus the results have to be interpreted according to suitable models. For the evaluation of PNR and SMR measurements we will use first Born approximation,[18] in which the domain size is the Fourier transform of the correlation length measured in the reciprocal space. As a first guess, we use exponential autocorrelation function in real space [86], leading to Lorentzian line-shape in reciprocal space. Also due to the slit setting we integrate with respect to q_y, reducing the problem to one dimension. For the autocorrelation function

$$C(x) = e^{-|x|/\xi} \tag{8.1}$$

where ξ is the 'average domain size' along the x-axis the function to be fitted will be

$$f(q_x) = \frac{A}{1 + (q_x\xi)^2}. \tag{8.2}$$

A is the intensity normalization factor. We start with fitting the PNR results. In Fig 8.13 the small and large domain state was fitted. The virgin domain size was $\xi = 0.272 \pm 0.009$ μm (measured in 0.3 T) and the ripened domain state had $\xi = 1.23 \pm 0.01$ μm (0 T), respectively. The ripening factor is 4.5. As we have seen exponential-like ω scans in the SMR measurements, the diffuse scattering peaks of the ripened domains were also fitted with an exponential (corresponding to Lorentzian autocorrelation function in direct space). The resulting correlation

[18] To obtain the average domain size and domain autocorrelation functions an off-specular fit would be necessary with properly selected model parameters (average roughness, correlation length, etc.). The starting parameters should be fed to the fitting algorithm, the results corrected with possible geometric effects and finally convolved with the instrumental resolution function. This is the way how Savage *et al.* proceeded in the case of prompt x-ray rocking curves [74]. The theory of off-specular Mössbauer reflectometry is being developed and will be available soon [98]. In the case of magnetic information not only domain structure, but also the magnetic roughness (originating from the structural roughness) may modify the results [86]. In this section a 'first-glance' description of the SMR and PNR ω scans is given.

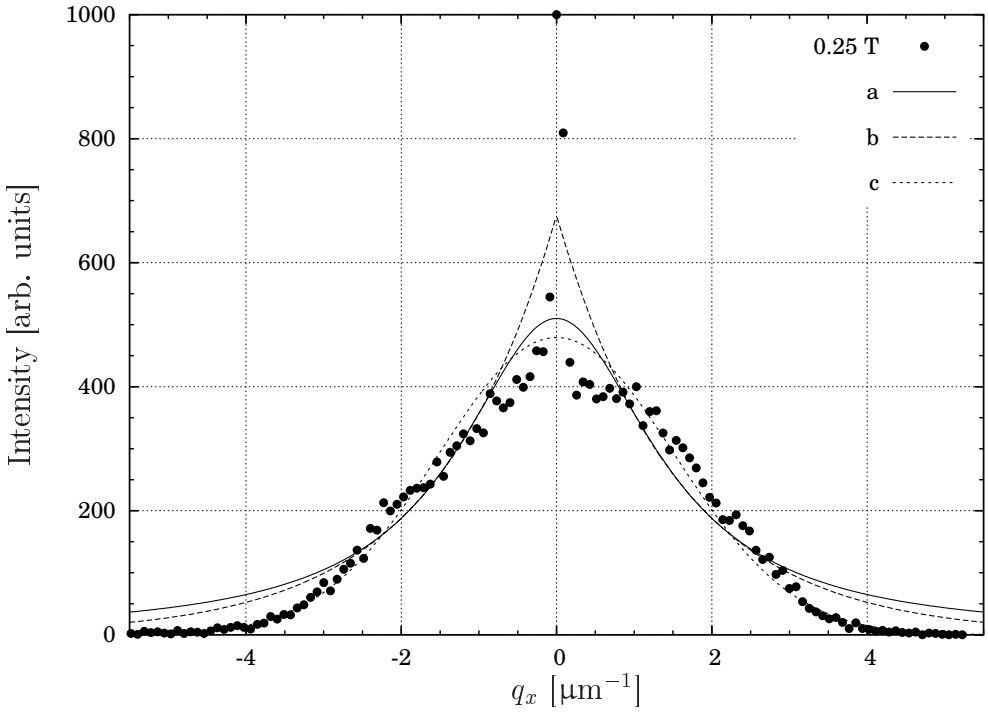

Figure 8.22: Off-specular scan showing the primary domain state. The lines are fits with the trial functions defined in the text. The best fitting function is c, the Gaussian. The scans were taken at ESRF shift SI-962 (December 2003).

length was $\xi = 0.989 \pm 0.013$ μm, which is in the same range as for the Lorentzian fit.

For the SMR scans we got different qualitative results. Even the function fitting best can be different. We used three trial functions:

$$a) \quad \frac{A}{1+(q_x\xi)^2} \tag{8.3a}$$

$$b) \quad Ae^{-|q_x\xi|} \tag{8.3b}$$

$$c) \quad Ae^{-\frac{1}{2}(q_x\xi)^2} \tag{8.3c}$$

For the small domain state there is no real good fit.[19] The best is the Gaussian fit (function c). Interestingly the obtained ξ values are almost identical independently of the model function used. The fitting results are summarized in Table 8.1.

The domain coarsening was also investigated in the hard direction by SMR. In the SI-847 shift (February 2003) the coarsening was thoroughly mapped. We have seen again the manifestation of the θ_0 instability leading to systematic errors, which make the proper data interpretation quite difficult. From the non-reproducibility and asymmetry of the shoulders of the prompt ω scans one can conclude that systematic errors can alter the measurements

[19]The specular peak was excluded (± 0.5 μm^{-1}) from the fit.

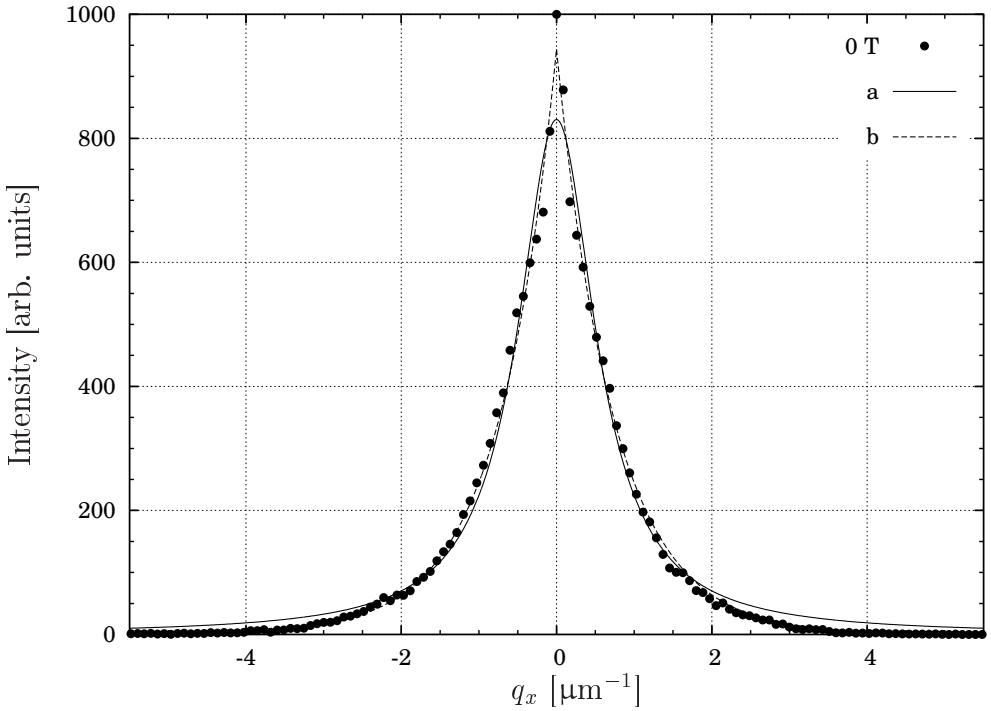

Figure 8.23: Off-specular scan showing the ripened domain state. The lines are fits with the trial functions defined in the text. Now the exponential function b gave the best result. The scans were taken at ESRF shift SI-962 (December 2003).

Field [T]	Fit type	ξ [μm]
0.25	Lorentzian (a)	0.66 ± 0.04
	Exponential (b)	0.64 ± 0.04
	Gaussian (c)	0.66 ± 0.01
0	Lorentzian (a)	1.64 ± 0.03
	Exponential (b)	1.35 ± 0.01

Table 8.1: Easy direction ξ fits with different autocorrelation trial functions of the SMR $\omega-$scans (SI-962, December 2003).

in different ways. The geometrical changes are not big but they are magnified due to the grazing-incidence setup. The resonant rocking curves are sometimes also asymmetric. The off-specular parts of the $\omega-$scans[20] could be described phenomenologically by sum of Gaussian and exponential functions. We do not detail the numerical results, as with no proper model the interpretation of the data is very difficult.[21] We would like only to summarize some general trends. On Figures 8.22 and 8.23 the domain state before and after ripening can be seen with different trial fitting functions (8.3).

When unsaturating the sample along a hard direction from supersaturation the ω scan can be described by a Gaussian function. The shape of the autocorrelation function changes with the ripening process to exponential in the range of $0.2 - 0.125$ T. The exponential nature stays when the field is increased from remanence. The correlation length seems to grow in *increasing* field (in the range of $0.5 - 0.8$ T) but we attribute this effect to the changing domain angles and not to the ripening of the domains.[22] In the easy-direction SMR ω scans no such effect was seen. The obtained ξ values are in good agreement with the easy direction SMR scans.

The ripening factor for SMR measurements is 2 (or 2.5 depending on the function), which is smaller than the 4.5 factor obtained from PNR measurements. We attribute this difference to the differences in methods, i.e. in our opinion the small virgin domains are simply too small to be resolved by SMR. The off-specular scattering amplitude is limited by geometrical effects and in our case this envelope is reached, which can be also noted from the shape change of the scattering. The same difficulties were not present on the PNR scan, where the cross section of the scattering is much smaller, and thus the penetration depth exceeds the sample volume even in grazing incidence setup.

In conclusion, we observed domain ripening in both easy and hard directions. The ripening process develops in the same way, independently of the orientation of the sample. This fact, and the direction independence of the supersaturation field suggests that domain ripening is not connected with crystalline anisotropy. The ripening occurs in a well-defined field range, enlarging the average domain size by roughly a factor of 5. The resulting large domains are in the order of μm. Both PNR and SMR measurements of the ripened domains can be fitted best by exponentials, indicating a Lorentzian autocorrelation function of the domains. This is in contradiction with the exponential shape, generally assumed in the literature [86].

[20] Excluding the $\pm 0.015^\circ$ region of the specular peak.

[21] The $\omega-$scans were evaluated but finally we decided not to include the detailed evaluation in this work for the previously mentioned reasons.

[22] The same 'extra' ripening could been deduced from PNR measurements, where in the easy direction the lowering peaks in increasing field showed an increasing autocorrelation length.

8.4 BSF and domain coarsening

Finally, after the domain ripening, we describe the domain coarsening connected to the BSF transition [6, 47, 79]. As discussed in Sections 3.3 and 6 when a sample with fourfold in-plane crystalline anisotropy is saturated along an easy direction and then the field is reduced to remanence, the layer magnetizations will be perpendicular to the direction of the vanishing field. The BSF is induced by the application of a perpendicular in-plane magnetic field. The BSF results in the coarsening of the AF domains [6].

During BSF, the magnetizations turn by $\pm 90°$. In the case of SMR measurements two perpendicular set-ups are necessary to see the different domains. Conversely, with PNR measurement a single scan is enough, because here the orthogonal domains separate to the spin-flip and non spin-flip channels, respectively.

In the following we cite parts from the work of our group [6]. The domain coarsening can be monitored by polarized neutron diffuse scattering, without rotating the sample. Prior to the PNR experiment the sample was ex-situ saturated in 2.1 T, i.e., well above H_s and even the supersaturation field. The sample layer magnetizations were parallel/antiparallel in zero field to the incident neutron polarization. PNR maps taken in increasing external field are shown in Fig. 8.24. Left and right columns in Fig.8.24 represent non-spin-flip and spin-flip reflectivities (here R^{--} and R^{-+}), corresponding to magnetization components parallel/antiparallel and perpendicular to the neutron spin, respectively. In a field below H_{SF} (Fig. 8.24A) the AF reflection appears only in the non-spin-flip channels and consists of a broad diffuse sheet. In contrast, in Fig. 8.24C, in a field above the transition, the AF reflection is only observed in the spin-flip channels. While the non-spin-flip channels consist only of off-specular diffuse sheets, the spin-flip channels show mainly specular scattering.[23] Midway the transition (Fig. 8.24B), the AF reflection shows up in both channels, in full accordance with the SMR results, detailed below.

In the SMR experiment (SI-618, December 2000), the sample was first saturated along the Fe[100] easy direction in 4.07 T, a field well above H_s and $H_{\text{sup. sat.}}$. In Fig. 8.25, ω scans are shown as a function of the longitudinal in-plane component q_x of the scattering vector [6]. When the field was released, the layer magnetizations lay in the perpendicular Fe[010] easy direction, parallel or antiparallel to $\mathbf{k}$, the photon wave vector (inset of Fig. 8.25B). While a sharp specular reflection was observed in the prompt reflectivity (Fig. 8.25A), only a broad diffuse shoulder appeared in the (delayed) SMR ω scan (Fig. 8.25B). On rotating the sample by 90°, the magnetizations turned perpendicular to $\mathbf{k}$, and the AF reflections disappeared since for $\mathbf{k}$-perpendicular hyperfine field no AF reflections are expected in time-integral $\theta - 2\theta$ SMR scans [62]. The intensity of the AF reflections recovered, when a field of 12 to 16 mT was applied along the Fe[010] direction perpendicular to the photon wave vector $\mathbf{k}$ and the ML

[23] The intensity of the PNR curves did not allow us to quantitatively describe the evolution of the domain structure.

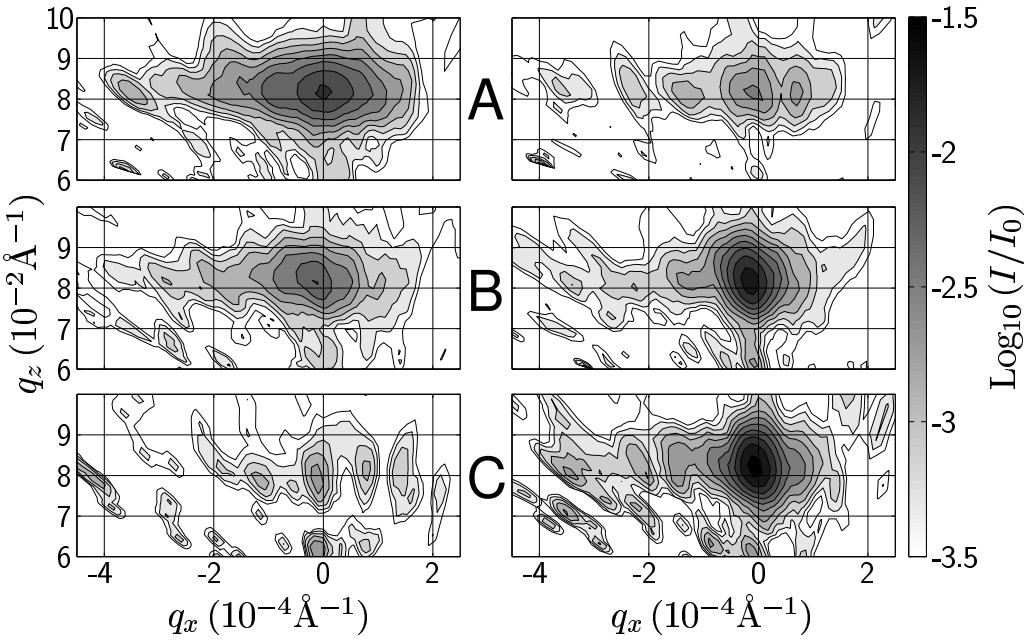

Figure 8.24: "Normalized neutron reflectivity maps. Polarized neutron intensity scattered specularly and off-specularly by a MgO(001)/$\left[^{57}\text{Fe}\ (26\ \text{Å})\ /\text{Cr}\ (13\ \text{Å})\right]_{20}$ multilayer in a magnetic field of A) 7 mT, B) 14.2 mT and C) 35 mT in R^{--} (left side) and in R^{-+} (right side) channels as a function of the scattering vector components q_x and q_z." [6]

passed the BSF [47]. Fig. 8.25C shows two ω scans of considerably different width, taken in two mutually perpendicular orientations of the sample relative to **k** following an exposure of the ML to 13 mT, half way in the BSF transition. At this point, the flipped regions of the ML (left inset of Fig. 8.25C) mainly give rise to a narrow specular peak, whereas the not-yet-flipped regions (right inset of Fig. 8.25C) stay to show a broad diffuse shoulder in the delayed intensity. By exposing the sample to 35 mT, the BSF transition is completely passed (inset of Fig. 8.25D) and the ω scan is dominated by a specular peak (Fig. 8.25D). No further change in the shape of the ω scan could be induced by any field cycle including repeated generation of BSF transitions, until the system was fully saturated. However, exposing the sample to 4.07 T field again, the ω scans became identical with that shown in Fig.8.25B, i.e., the specular peak disappeared from the SMR ω scan.

8.4.1 Experimental results

The interpretation of the coarsened domain state is not an easy task. As it can be seen from Fig 8.25D, the scattering from the large (coarsened) domains is almost specular, but there is still a small magnetic shoulder. This shoulder is better seen[24] in Fig. 8.21.

In Fig. 8.26 the domain coarsening during the BSF transition is shown. The first interesting point is that even before the BSF transition we do see off-specular scattering (left side, 0 T),

[24]The scans in Fig. 8.21 were collected at low temperature (15 K). The coarsened state is the same, as was seen in the earlier shift, but the statistics is much better here.

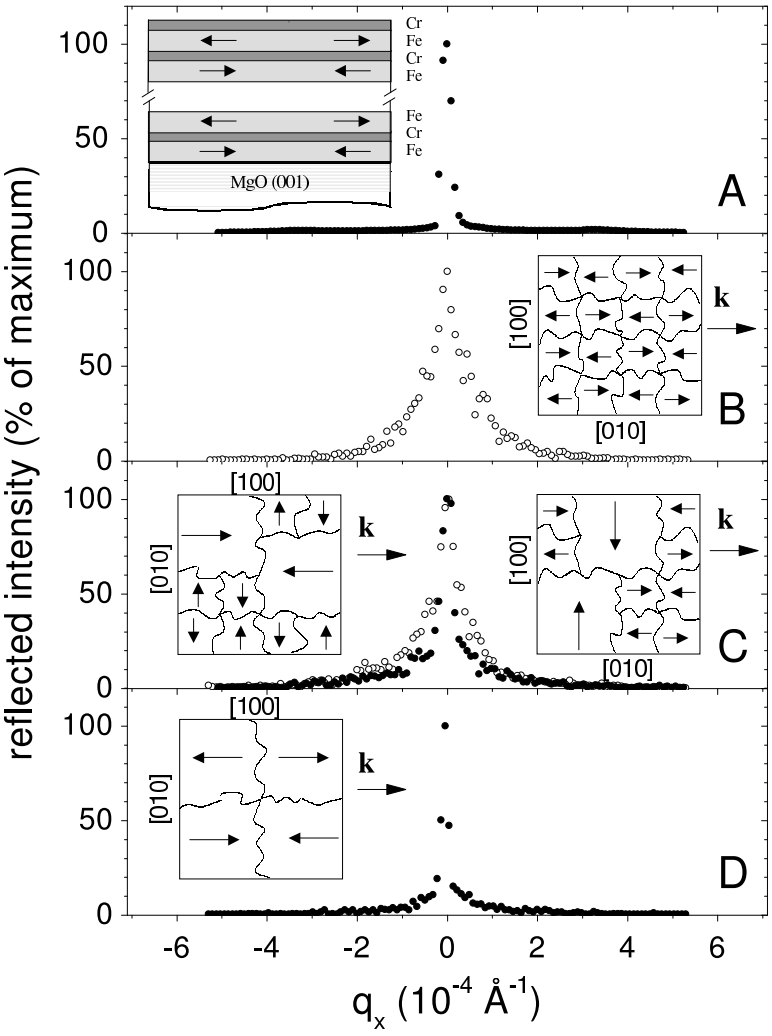

Figure 8.25: "Off-specular prompt X-ray and SMR ω-scans. Reflected intensity vs. scattering vector component q_x of a MgO(001)/$\left[^{57}\mathrm{Fe}\left(26\ \text{Å}\right)/\mathrm{Cr}\left(13\ \text{Å}\right)\right]_{20}$ multilayer at the AF Bragg-reflection measured in zero external magnetic field: A) prompt reflectivity, not being dependent on magnetic field prehistory, B–D) delayed reflectivity, B) following saturation in 4.07 T, C) following exposure to 13 mT parallel to the magnetizations (open circles: non-flipped domains, full circles: flipped domains), D) following exposure to a field of 35 mT. Inset A is a schematic side view of the chemical and magnetic structure of the sample in the vicinity of a domain wall (dotted line). Insets B–D are schematic top views of the orientation of the crystallographic axes and of the top-layer magnetizations (short and long arrows represent small and large domains, respectively) relative to the photon wave vector **k**." [6]

when no AF magnetic scattering is present. Secondly, during the spin flop the shape of the off-specular scattering narrows (right side) as the ripened domains are turning perpendicular, but we see no change in the line shape on the left side (where the domains should give contribution after the flop). The latter observation suggests that the coarsened domains are larger, than the resolution of our experiment. From the first statement it follows that not only AF domains, but also correlated magnetic interface roughness can contribute to the off-specular scattering at the AF position.[25] The experiment with the best statistics was SI-962 (2003 December). We were able to fit the off-specular spectra of Fig. 8.21 with the sum of two exponentials. The ξ values obtained are: $\xi_1 = 1.5 \pm 0.3$ μm, $\xi_2 = 14 \pm 0.9$ μm. The contribution of subspectra was 11% and 89% for ξ_1 and ξ_2, respectively. ξ_2 gives a lower size estimation of the coarsened domains, while the interpretation of the part with ξ_1 is not so straightforward. As was noted before, if they originated fully from AF-domain scattering, then we would not see this contribution before the spin flop (at 7 mT) and we would see an increasing shoulder with increasing field at the spin-flop region (Fig 8.26 left side). It is not easy to say if such increase wwas observed, as the statistics was low in those measurements. On the other hand the good agreement of ξ_1 with the coarsened domains suggest that this contribution originates from AF domain 'islands', which retain their ripened state. A final decisive statement could be given only based on measurements with better statistics, and perhaps at a higher-order AF peak.

The supersaturation effect was first investigated after the domain coarsening. In Fig. 8.27 the q_z and q_x scans are seen during the first test of supersaturation. At that time the effects of ripening were not known, thus all spectra were taken in remanence. The q_z scans show a widening of the AF peak, while the q_x scans show the reappearance of small domain after saturation in 1.3 T. As now we know, those domains are already ripened domains.

Latter measurements with much better statistics did confirm the details of the supersaturation. Here we only would like to note that the already coarsened domains also does not 'shrink' back prior to supersaturation.

8.4.2 Discussion

We found domain coarsening related to the BSF transition. The resulting domains were larger, than our instrumental resolution. The coarsened domains are thus at least by an order of magnitude larger, than the ripened ones, or in other words the 'coarsening factor' is greater than 10. If we take a look at the mechanism of the coarsening, then even domains, comparable with the size of the sample cannot be excluded [6].

In contrast to domain ripening, which involves domain wall movement, and thus limited by coercivity [6], at the spin flop the domain walls can annihilate by the ±90 degree rotation of the magnetizations, thus coarsening is not limited by coercivity. Furthermore at the BSF the

[25] In saturation this contribution is the same as the prompt scattering (Fig 8.5), while in zero field extra shoulders can be seen.

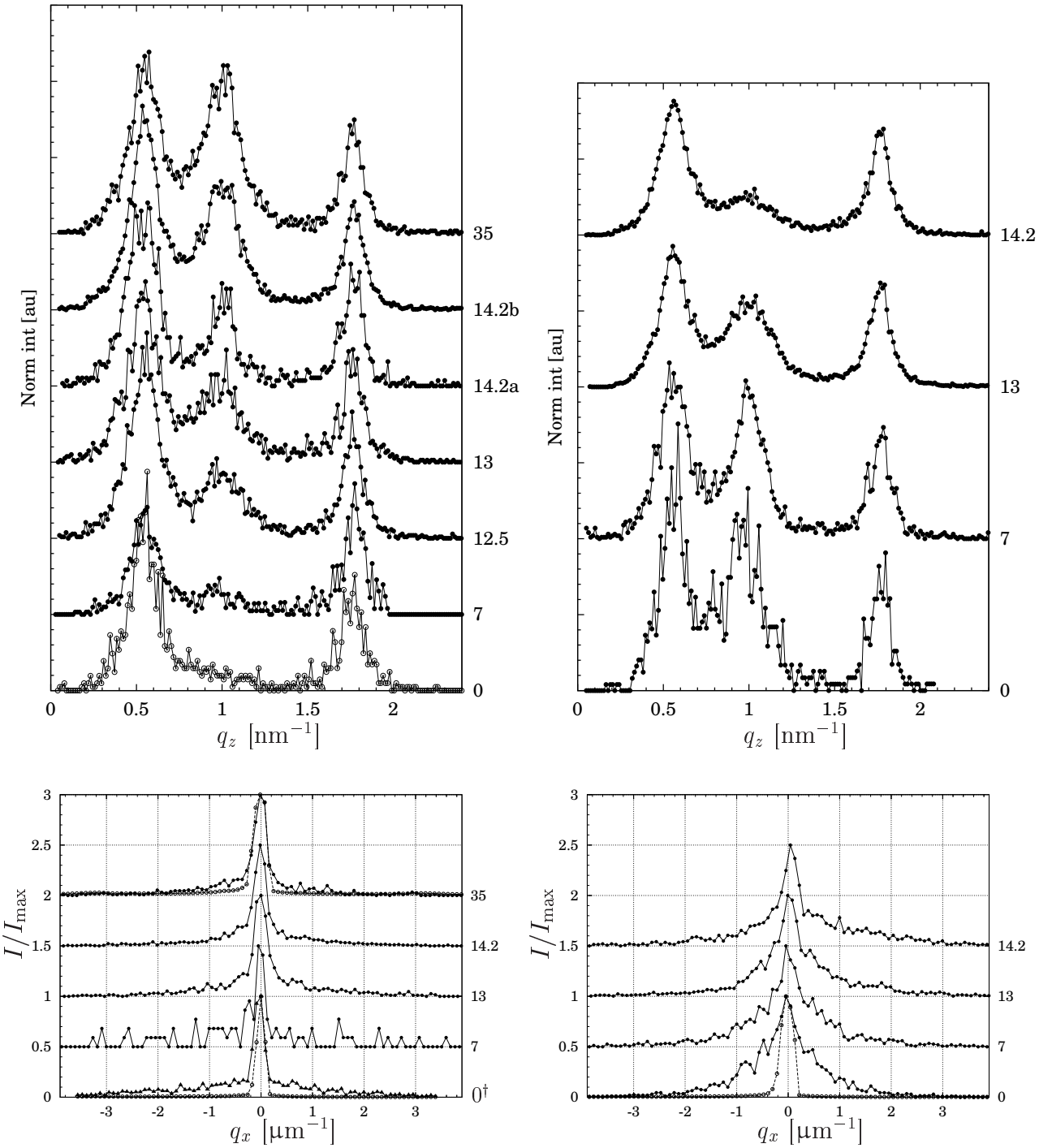

Figure 8.26: The BSF transition in momentum space portrayed by SMR (SI-618, December 2000‡). The AF state is perpendicular to **k** in the left scans, while parallel/antiparallel in the right scans. As the BSF occurs, the moments turn perpendicular, decreasing the original AF scattering, and giving rise to the perpendicular one. All measurements were carried out in zero field. The labels show the last seen highest field value. The open symbols show the prompt curves in the off-specular scans, while the closed ones are the resonant ones. (‡ All measurements were taken at SI-618, except for the 0 T ω scan, marked with †. This scan was taken in shift SI-735, August 2001. We included it, as no scan with such conditions was taken in SI-618.)

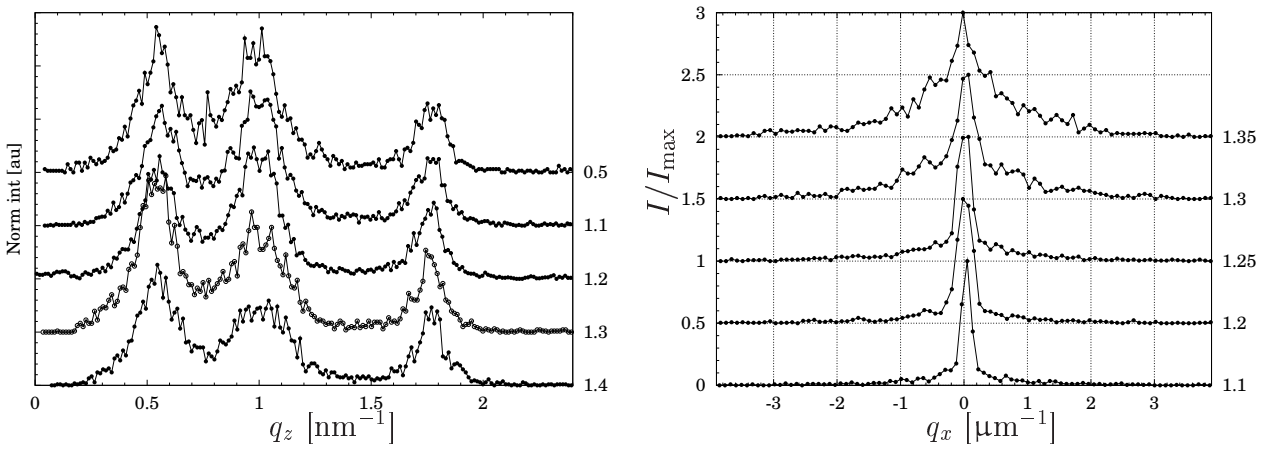

Figure 8.27: Easy direction supersaturation measured after domain coarsening (SI-618, December 2000). The scans were measured in zero external field. Change in the off-specular scattering at 1.3 T can be seen. The $\omega-$scans are the same as in Fig. 8.14.

system is in energy maximum, thus the domain growth is explosion like. If one part decided, the neighbors will follow to avoid the creation of new domain walls.

In conclusion, we found two processes related do domain wall energy, viz. domain ripening and coarsening. Both processes are irreversible in the sense that the sample has to be supersaturated to recover the 'virgin' domain state. From the comparison of easy and hard direction hysteresis loops we concluded that domain ripening is not connected with the anisotropy of the sample.For detailed evaluation of the process micromagnetic simulations will be necessary, which are beyond the scope of this work.

Chapter 9

Appendix

9.1 Inversion of the magnetization curve

We show, that with certain limitations, energy curves can be calculated from the magnetization loops ('inverse problem'). The reversed approach is trivial and it is practiced by all fitting routines: take the energy function, then minimize the energy at each external field value and calculate the magnetization loop. To solve the inverse problem, one have to make some assumptions. For a first approach we take a trilayer, with configurations symmetrical to the external field only. In this case the angle between the two layers describes the trilayer unambiguously. For convenience, we define this angle as 2ϑ. In this case the energy of the trilayer will be

$$\varrho_E(\vartheta, H) = \varrho_E^0(\vartheta) - H M \cos\vartheta. \tag{9.1}$$

When displaying the magnetization measurements as reduced[1] magnetization loop $m(H)$, we 'measure' the angle[2] $m(H) = \cos\vartheta$. The inversion is straightforward: $\vartheta = \arccos m(H)$.

In each point of the magnetization cycle the system is in equilibrium, $\partial\varrho_E/\partial\vartheta = 0$. If we assume that the coupling, anisotropy and other terms do not depend on the external magnetic field, then from (9.1):

$$\frac{\partial\varrho_E^0}{\partial\vartheta} = -H M \sin\vartheta. \tag{9.2}$$

We only have to substitute ϑ to get the derivative function:

$$\frac{\partial\varrho_E^0}{\partial\vartheta} = -H M \sin(\arccos m(H)) = -H M\sqrt{1 - m^2(H)}. \tag{9.3}$$

By plotting $-H M\sqrt{1-m^2}$ versus $\vartheta = \arccos m$ (not shown) we obtain the derivative curve. Note that the integration is done most easily numerically as the base points are not equally

[1] We plot the data in units of saturation moment.

[2] This is exact result for the trilayer case and a good approximation for MLs with finite stacking.

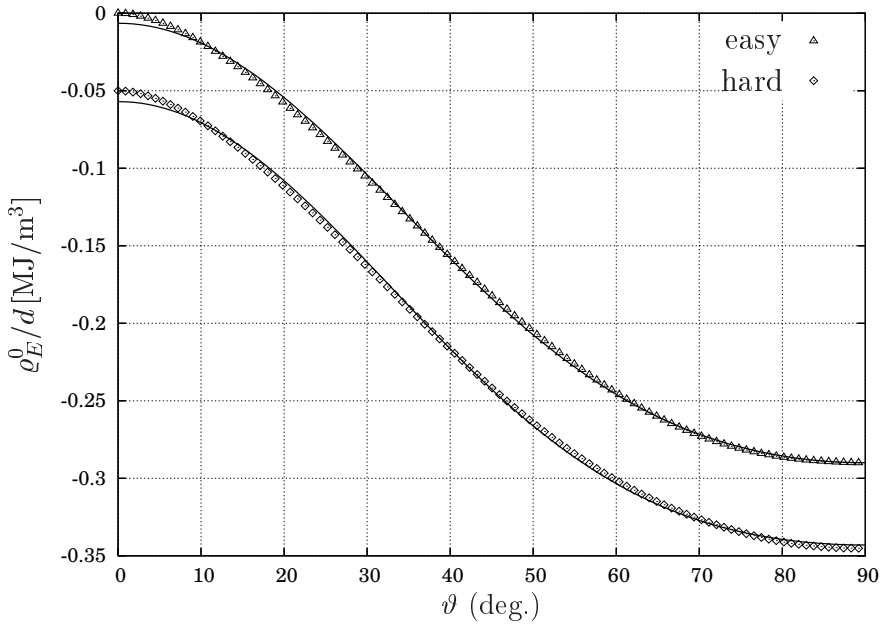

Figure 9.1: Inversion of the SQUID magnetization curves of sample 990608 (Fig. 3.2) to energy versus angle in the two-sublayer model. The easy and hard direction loops are shifted for clarity. The lines are fits by the two-sublayer bilinear-biquadratic model with fourfold crystal anisotropy.

distributed.

$$\varrho_E^0(\vartheta) = \int_0^{\vartheta} \frac{\partial \varrho_E^0}{\partial \vartheta'} d\vartheta'. \tag{9.4}$$

We neglected the integration constant as it does not count in the minimum calculations. The absolute value of the energy density is proportional to M. The above derivation is also valid for 'infinite stacked' MLs in the two-sublattice approximation. As an example, the SQUID measurements of sample 990608 are transformed. The fits in Fig. 9.1 are according to the bilinear-biquadratic formalism with fourfold anisotropy. In this model the field-independent energy density per unit area[3] is:

$$\varrho_E^0 = J\cos 2\vartheta + \frac{B}{2}\cos 4\vartheta \mp \frac{K}{8} t_{\mathrm{Fe}} \cos 4\vartheta. \tag{9.5}$$

An appropriate fitting function for the above equation is: $f(\vartheta) = a_0 + a_1 * \cos 2\vartheta + a_2 * \cos 4\vartheta$. From the fits the easy and hard direction parameters (a_1^e, a_2^e, a_1^h, a_2^h) may be obtained. As only the first term of the right-hand side of equation (9.5) is a function of $\cos 2\vartheta$, we map it to a_1. Also we found that $a_1^e \approx a_2^h$, as it should be. From the combination of the a_2 terms one may get the biquadratic and anisotropy terms too: $a_2^h - a_2^e = K/4, \quad a_2^h + a_2^e = B/d$. As shown in in Fig. 9.1 the fit is worse at the low-angle region, which is the closest to saturation part of the magnetization cycle. By applying new fitting functions, the energy curves could be fitted better.

[3] $-K$: easy direction, $+K$: hard direction.

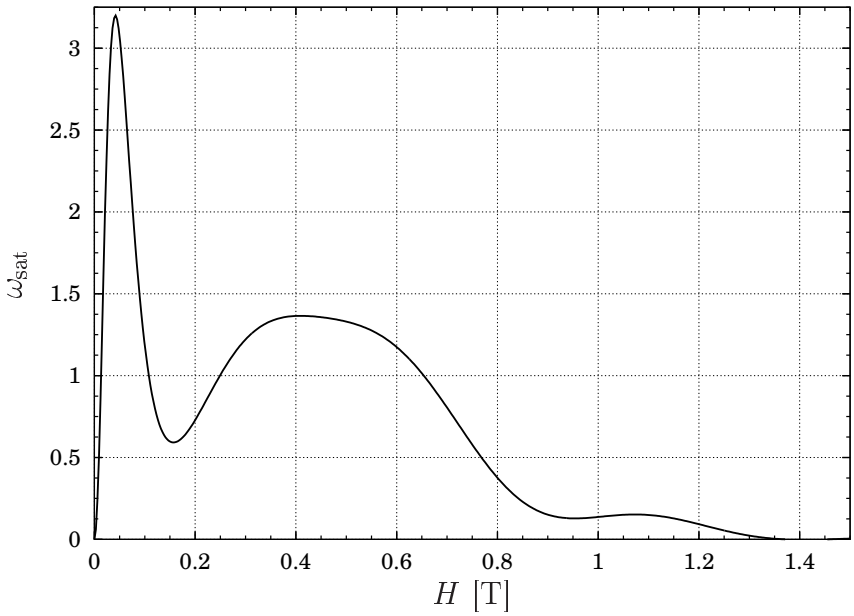

Figure 9.2: The supposed $\omega_{\rm sat}$ distribution of sample 990608 in case of pure bilinear AF coupling model.

9.2 Distribution inversion

If a ML has only broadly distributed bilinear AF coupling then it is possible to deduce the distribution of saturation field $\omega_{\rm sat}\,(H)$ from the magnetization loop by the following formula:

$$\omega_{\rm sat}\,(H) = -H\,M''\,(H)\,. \tag{9.6}$$

Interpolating the measured magnetization data by analytical functions the distribution ω will be also smoother. To check the process of inversion one can integrate ω. The easy-direction VSM loop of sample 990608 was fitted as an example. In our particular case the fitting function was composed of two parts:

$$f_1(x) = a_0 \tanh(b_0 x) + a_1 \tanh(b_1 x) + a_2 \tanh(b_2 x) + a_3 \tanh(b_3 x), \tag{9.7}$$

$$f_2(x) = h \sin(nx) \exp(-n_2 x^2). \tag{9.8}$$

The constants were fitted with gnuplot[4] first fitting with f_1 then the remaining error was minimized by introducing f_2 and fitting it. The derivatives and second derivatives were calculated by maple[5] and introduced into gnuplot to produce the distribution plot (Fig. 9.2). We used octave[6] to integrate the result. The resulting distribution is shown in Fig. 9.2. Note that the above calculation works strictly in the case when only bilinear AF coupling is present. If other coupling terms, anisotropies are also present then the transformation will lead wrong result.

[4] http://www.gnuplot.info/
[5] http://www.maplesoft.com/products/maple/
[6] http://www.octave.org/

Bibliography

[1] M. N. Baibich, J. M. Broto, A. Fert, F. Nguyen Van Dau, F. Petroff, P. Eitenne, G. Creuzet, A. Friederich, and J. Chazelas. Giant magnetoresistance of (001)Fe/(001)Cr magnetic superlattices. *Phys. Rev. Lett.*, 61:2472–2475, 1988.

[2] E. Hirota, H. Sakakima, and K. Inomata. *Giant Magnetoresistance Devices*, volume 40 of *Surface Sciences*. Springer, 2002.

[3] P. Grünberg, R. Schreiber, Y. Pang, M. B. Brodsky, and H. Sowers. Layered magnetic structures: Evidence for antiferromagnetic coupling of Fe layers across Cr interlayers. *Phys. Rev. Lett.*, 57:2442, January 1986.

[4] Alex Hubert and Rudolf Schäfer. *Magnetic Domains*. Springer, 2000.

[5] J. Meersschaut, C. L'abbé, F. M. Almeida, J. S. Jiang, J. Pearson, U. Welp, M. Gierlings, H. Maletta, and S. D. Bader. Hard-axis magnetization behavior and the surface spin-flop transition in antiferromagnetic fe/cr(100) superlattices. *Phys. Rev. B*, 2006. accepted for publication.

[6] D. L. Nagy, L. Bottyán, B. Croonenborghs, L. Deák, B. Degroote, J. Dekoster, H. J. Lauter, V. Lauter-Pasyuk, O. Leupold, M. Major, J. Meersschaut, O. Nikonov, A. Petrenko, R. Rüffer, H. Spiering, and E. Szilágyi. Coarsening of antiferromagnetic domains in multilayers: The key role of magnetocrystalline anisotropy. *Phys. Rev. Lett.*, 88:157202, 2002.

[7] D. T. Pierce, J. Unguris, R. J. Celotta, and M. D. Stiles. Effect of roughness, frustration, and antiferromagnetic order on magnetic coupling of Fe/Cr multilayers. *J. Magn. Magn. Mater.*, 200:290–321, 1999.

[8] U. K. Rößler and A. N. Bogdanov. Magnetic phases and reorientation transitions in antiferromagnetically coupled multilayers. *Phys. Rev. B*, 69:184420–(1–15), 2004.

[9] W. H. Press, S. A. Teukolsky, W. T. Vetterling, and B. P. Flannery. *Numerical Recipes in C: the Art of Scientific Computing*. Cambridge University Press, Cambridge, 2 edition, 1997.

[10] F. C. Nörtemann, R. L. Stamps, A. S. Carriço, and R. E. Camley. Finite-size effects on spin configurations in antiferromagnetically coupled multilayers. *Phys. Rev. B*, 46:10847, 1992.

[11] M. Major. *Véges multirétegek mágneses szerkezete (Magnetic structure of finite stacked multilayers)*. Diploma theses, ELTE, 1999.

[12] S. S. P. Parkin, A. Mansour, and G. P. Felcher. Antiferromagnetic interlayer exchange coupling in sputtered Fe/Cr multilayers: Dependence on number of Fe layers. *Appl. Phys. Lett.*, 58:1473–1475, 1991.

[13] V. Lauter-Pasyuk, H. J. Lauter, B. P. Toperverg, L. Romashev, and V. Ustinov. Transverse and lateral structure of the spin-flop phase in Fe/Cr antiferromagnetic superlattices. *Phys. Rev. Lett.*, 89(16):167203, 2002.

[14] E. E. Fullerton, M. J. Conover, J. E. Mattson, C. H. Sowers, and S. D. Bader. Oscillatory interlayer coupling and giant magnetoresistance in epitaxial Fe/Cr(211) and (100) superlattices. *Phys. Rev. B*, 48:15755–15763, 1993.

[15] S. T. Purcell, W. Folkerts, M. T. Johnson, N. W. E. McGee, K. Jager, J. aan de Stegge, W. B. Zeper, and W. Hoving. Oscillations with a period of two Cr monolayers in the antiferromagnetic exchange coupling in a (001) Fe/Cr/Fe sandwich structure. *Phys. Rev. Lett.*, 67:903–906, 1991.

[16] B. Heinrich, J. F. Cochran, T. Monchesky, and R. Urban. Exchange coupling through spin-density waves in Cr(001) structures: Fe-whisker/Cr/Fe(001) studies. *Phys. Rev. B*, 59:14520–14532, 1999.

[17] M. Rührig, R. Schäfer, A. Hubert, R. Mosler, J. A. Wolf, S. Demokritov, and P. Grünberg. Domain observations on Fe–Cr–Fe layered structures (evidence for a biquadratic coupling effect). *Phys. Status Solidi A*, 125:635, 1991.

[18] J. C. Slonczewski. Overview of interlayer exchange theory. *J. Magn. Magn. Mater.*, 150:13–24, 1995.

[19] J. Barnaś and P. Grünberg. On the biquadratic interlayer coupling in layered magnetic structures. *J. Magn. Magn. Mater.*, 121:326–329, 1993.

[20] J. Barnaś. Intrinsic biquadratic contribution to interlayer coupling in magnetic layered structures. *J. Magn. Magn. Mater.*, 123:L21–L24, 1993.

[21] S. M. Rezende, C. Chesman, M. A. Lucena, M. C. de Moura, A. Azevedo, F. M. de Aguiar, and S. S. P. Parkin. Biquadratic coupling in sputtered Fe/Cr/Fe still in need of a new mechanism. *J. Appl. Phys.*, 85(8):5892–5894, 1999.

[22] S. O. Demokritov. Biquadratic interlayer coupling in layered magnetic systems. *J. Phys. D: Appl. Phys.*, 31:925–941, 1998.

[23] S. M. Rezende, C. Chesman, M. A. Lucena, M. C. de Moura, A. Azevedo, and F. M. de Aguiar. Magnetic multilayers: Interlayer coupling in Fe/Cr/Fe. *Materials Science Forum*, 302-303:64–75, 1999.

[24] J. Meersschaut, C. L'abbé, M. Rots, and S. D. Bader. Origin of biquadratic coupling in Fe/Cr(100) superlattices. *Phys. Rev. Lett.*, 87:107201, 2001.

[25] R. S. Fishman. Spin-density waves in Fe/Cr trilayers and multilayers. *Journal of Physics: Condensed Matter*, 13(13):R235–R269, 2001.

[26] C. L'abbé, J. Meersschaut, M. Rots, and S. D. Bader. Fluctuating spin density waves revealed by perturbed angular correlation spectroscopy. *J. Appl. Phys.*, 93(10):8250–8252, 2003.

[27] J. C. Slonczewski. Fluctuation mechanism for biquadratic exchange coupling in magnetic multilayers. *Phys. Rev. Lett.*, 67:3172–3175, 1991.

[28] D. B. Fulghum and R. E. Camley. Magnetic behavior of antiferromagnetically coupled layers connected by ferromagnetic pinholes. *Phys. Rev. B*, 52:13436–13443, 1995.

[29] S. O. Demokritov, C. Bayer, S. Poppe, M. Rickart, J. Fassbender, B. Hillebrands, D. I. Kholin, N. M. Kreines, and O. M. Liedke. Control of interlayer exchange coupling in Fe/Cr/Fe trilayers by ion beam irradiation. *Phys. Rev. Lett.*, 90:097201, 2003.

[30] F. Stobiecki, M. Kopcewicz, J. Jagielski, B. Szymański, M. Urbaniak, J. Dubowik, M. Schmidt, and J. Kalinowska. Mössbauer spectroscopy, interlayer coupling and magnetoresistance of irradiated Fe/Cr multilayers. *Journal of Alloys and Compounds*, 382:174–178, 2004.

[31] F. Stobiecki, B. Szymański, M. Urbaniak, T. Luciński, J. Dubowik, M. Kopcewicz, J. Jagielski, and Y. P. Lee. Influence of ion irradiation on the magnetic properties of Fe/Cr multilayers. *Journal of the Korean Physical Society*, 45(1):1–5, 2004.

[32] M. Kopcewicz, F. Stobiecki, J. Jagielski, B. Szymanski, M. Urbaniak, and T. Luciński. Modification of microstructure and magnetic properties of Fe/Cr multilayers caused by ion irradiation. *J. Magn. Magn. Mater.*, 2005.

[33] M. Kopcewicz, F. Stobiecki, J. Jagielski, B. Szymanński, M. Schmidt, J. Dubowik, and J. Kalinowska. Influence of the Ar-ion irradiation on the giant magnetoresistance in Fe/Cr multilayers. *J. Appl. Phys.*, 93:5514–5518, 2003.

[34] V. N. Men'shov and V. V. Tugushev. Short-range magnetic order in a spin density wave in Cr-based multilayers. *J. Exp. Theor. Phys.*, 93:786–795, 2001.

[35] V. N. Men'shov and V. V. Tugushev. The effect of proximity-induced spin density wave order and interface roughness on magnetic coupling in Fe/Cr multilayers. *J. Magn. Magn. Mater.*, 272-276:1242–1243, 2004.

[36] V. N. Men'shov and V. V. Tugushev. The mechanism of interlayer exchange coupling in iron-chromium type nanostructures. *J. Exp. Theor. Phys.*, 98(1):123–134, 2004.

[37] N. M. Kreines, D. I. Kholin, S. O. Demokritov, and M. Rikart. Noncollinear interlayer exchange in Fe/Cr/Fe magnetic structures with different interface roughnesses. *JETP Letters*, 78:627–630, 2003.

[38] V. N. Men'shov and V. V. Tugushev. Noncollinear magnetic states in iron-chromium-type multilayers. *J. Exp. Theor. Phys.*, 95(5):901–911, 2002.

[39] E. W. Hill, S. L. Tomlinson, and J. P. Li. The role of dipole coupling in multilayers. *J. Appl. Phys.*, 73(10):5978–5980, 1993.

[40] B. Dieny, J. P. Gavigan, and J. P. Rebouillat. Magnetisation processes, hysteresis and finite-size effects in model multilayer systems of cubic or uniaxial anisotropy with antiferromagnetic coupling between adjacent ferromagnetic layers. *Journal of Physics: Condensed Matter*, 2(1):159–185, 1990.

[41] B. Dieny and J. P. Gavigan. Minimum energy versus metastable magnetisation processes in antiferromagnetically coupled ferromagnetic multilayers. *Journal of Physics: Condensed Matter*, 2(1):187–194, 1990.

[42] Simon Foner. Antiferromagnetic and ferrimagnetic resonance. In George T. Rado and Harry Suhl, editors, *Magnetism*, volume I, pages 383–448. Academic Press, 1963.

[43] K. Temst, E. Kunnen, V. V. Moshchalkov, H. Maletta, H. Fritzsche, and Y. Bruynseraede. Magnetic order and the spin-flop transition in Fe/Cr superlattices. *Physica B*, 276-278:684–685, 2000.

[44] Juniro Kanamori. Anisotropy and magnetostriction of ferromagnetic and antiferromagnetic materials. In George T. Rado and Harry Suhl, editors, *Magnetism*, volume I, pages 127–203. Academic Press, 1963.

[45] A. L. Dantas and A. S. Carriço. Surface-induced low-field instability of antiferromagnetic multilayers. *Phys. Rev. B*, 59(2):1223–1231, 1999.

[46] R. W. Wang, D. L. Mills, E. E. Fullerton, J. E. Mattson, and S. D. Bader. Surface spin-flop transition in Fe/Cr(211) superlattices: Experiment and theory. *Phys. Rev. Lett.*, 72(6):920–923, 1994.

[47] L. Bottyán, L. Deák, J. Dekoster, E. Kunnen, G. Langouche, J. Meersschaut, M. Major, D. L. Nagy, H. D. Rüter, E. Szilágyi, and K. Temst. Observation of the bulk spin-flop in an Fe/Cr superlattice. *J. Magn. Magn. Mater.*, 240:514–516, 2002.

[48] R. Schad, D. Bahr, J. Falta, P. Beliën, and Y. Bruynseraede. Structural analysis of Fe/Cr superlattices and their components. *Journal of Physics: Condensed Matter*, 10(1):61–66, 1998.

[49] K.-H. Hellwege and O. Madelung, editors. *Landolt-Börnstein, Numerical Data and Functional Relationships in Science and Technology*, volume 19A. Springer-Verlag, 1986.

[50] F. G. Aliev, R. Guerrero, J. L. Martinez, V. V. Moshchalkov, Y. Bruynseraede, and R. Villar. Low-frequency response in antiferromagnetically coupled Fe/Cr multilayers. *J. Magn. Magn. Mater.*, 226-230:1806–1807, 2001.

[51] A. I. Chumakov, L. Niesen, D. L. Nagy, and E. E. Alp. Nuclear resonant scattering of synchrotron radiation by multilayer structures. *Hyp. Int.*, 123(1-8):427–454, 1999.

[52] D. L. Nagy, L. Bottyán, L. Deák, E. Szilágyi, H. Spiering, J. Dekoster, and G. Langouche. Synchrotron Mössbauer reflectometry. *Hyp. Int.*, 126:353–361, 2000.

[53] A. H. Compton. The total reflexion of X-rays. *Philos. Mag.*, 45:1121, 1923.

[54] H. Kiessig. Untersuchungen zur totalreflexion von röntgenstrahlen (investigations into the total reflexion of x-ray). *Ann. Phys. (Berlin)*, 10:715, 1931.

[55] E. Fermi and W. Zinn. *Phys. Rev.*, 70:103, 1946.

[56] M. Born and E. Wolf. *Principles of Optics*. Pergamon Press, 1970.

[57] M. Lax. Multiple scattering of waves. *Rev. Mod. Phys.*, 23(4):287–310, 1951.

[58] L. Deák, L. Bottyán, D. L. Nagy, and H. Spiering. A common optical algorithm for the evaluation of specular spin polarized neutron and Mössbauer reflectivities. *Physica B*, 297:113–117, 2001.

[59] S. M. Irkaev, M. A. Andreeva, V. G. Semenov, G. N. Belozerskii, and O. V. Grishin. Grazing-incidence Mössbauer-spectroscopy - new method for surface-layers analysis, 1. instrumentation. *Nucl. Instrum. Meth. B*, 74:545–553, 1993.

[60] E. Gerdau, R. Rüffer, H. Winkler, W. Tolksdorf, C. P. Klages, and J. P. Hannon. Nuclear Bragg diffraction of synchrotron radiation in yttrium iron garnet. *Phys. Rev. Lett.*, 54:835–838, 1985.

[61] G. V. Smirnov. Nuclear resonant scattering of synchrotron radiation. *Hyp. Int.*, 97-98:551–588, 1996.

[62] D. L. Nagy, L. Bottyán, L. Deák, E. Szilágyi, H. Spiering, J. Dekoster, and G. Langouche. Synchrotron Mössbauer reflectometry. *Hyp. Int.*, 126:353–361, 2000.

[63] D. L. Nagy, L. Bottyán, L. Deák, and M. Major. Synchrotron Mössbauer reflectometry – recent applications in multilayer magnetism. *Acta Physica Polonica A*, 100:669–678, 2001.

[64] G. V. Smirnov. General properties of nuclear resonant scattering. *Hyp. Int.*, 123-124:31–77, 1999.

[65] T. S. Toellner, W. Sturhahn, R. Röhlsberger, E. E. Alp, C. H. Sowers, and E. E. Fullerton. Observation of pure nuclear diffraction from a Fe/Cr antiferromagnetic multilayer. *Phys. Rev. Lett.*, 74(17):3475–3478, 1995.

[66] H. Zabel and K. Theis-Bröhl. Polarized neutron reflectivity and scattering studies of magnetic heterostructures. *Journal of Physics: Condensed Matter*, 15(5):S505–S517, 2003.

[67] G. P. Felcher and S. G. E. te Velthuis. Perspectives of polarized-neutron reflectometry: magnetic domains and off-specular scattering. *Applied Surface Science*, 182:209–215, 2001.

[68] G. P. Felcher. Neutron reflectometry as a tool to study magnetism. *J. Appl. Phys.*, 87:5431–5436, 2000.

[69] J. F. Ankner and G. P. Felcher. Polarized-neutron reflectometry. *J. Magn. Magn. Mater.*, 200:741–754, 1999.

[70] C. F. Majkrzak. Neutron scattering studies of magnetic thin films and multilayers. *Physica B*, 221:342–356, 1996.

[71] V. L. Aksenov, K. N. Jernenkov, S. V. Kozhevnikov, H. Lauter, V. Lauter-Pasyuk, Yu. V. Nikitenko, and A. V. Petrenko. The polarized neutron spectrometer REMUR at the pulsed reactor IBR-2. In *Communication of the Joint Institute of Nuclear Research*, number D13-2004-47, pages 1–31, Dubna, 2004.

[72] V. Lauter-Pasyuk, H. J. Lauter, B. Toperverg, O. Nikonov, E. Kravtsov, M. A. Milyaev, L. Romashev, and V. Ustinov. Magnetic off-specular neutron scattering from Fe/Cr multilayers. *Phys. B*, 283:194–198, 2000.

[73] D. E. Savage, N. Schimke, Y.-H. Phang, and M. G. Lagally. Interfacial roughness correlation in multilayer films: Influence of total film and individual layer thicknesses. *J. Appl. Phys.*, 71(7):3283–3293, 1992.

[74] D. E. Savage, J. Kleiner, N. Schimke, Y.-H. Phang, T. Jankowski, J. Jacobs, R. Kariotis, and M. G. Lagally. Determination of roughness correlations in multilayer films for x-ray mirrors. *J. Appl. Phys.*, 69(3):1411–1424, 1991.

[75] W. Hahn, M. Loewenhaupt, G. P. Felcher, Y. Y. Huang, and S. S. P. Parkin. Fe/Cr multilayers: Effect of annealing on the spin structure and magnetoresistance. *J. Appl. Phys.*, 75(7):3564–3570, 1994.

[76] S. Langridge, J. Schmalian, C. H. Marrows, D. T. Dekadjevi, B. J. Hickey, and E. C. Stoner. Quantification of magnetic domain disorder and correlations in antiferromagnetically coupled multilayers by neutron reflectometry. *Phys. Rev. Lett.*, 85:4964–4967, 2000.

[77] Sven A. E. Johansson, John L. Campbell, and Klas G. Malmqvist, editors. *Particle Induced X-ray Emission Spectrometry (PIXE)*. Wiley & Sons, New York, 1995.

[78] D. L. Windt. IMD—software for modelling the optical properties of multilayer films. *Computers in Physics*, 12:360–370, 1998.

[79] L. Bottyán, J. Dekoster, L. Deák, B. Degroote, E. Kunnen, C. L'abbé, G. Langouche, O. Leupold, M. Major, J. Meersschaut, D. L. Nagy, and R. Rüffer. Bulk spin transition in a magnetic superlattice. *ESRF Highlights*, page 62, 1999.

[80] H. T. Hardner, M. B. Weissman, and S. S. P. Parkin. History dependent domain structures in giant-magnetoresistive multilayers. *Appl. Phys. Lett.*, 67(13):1938–1940, 1995.

[81] D. L. Nagy, L. Bottyán, L. Deák, B. Degroote, O. Leupold, M. Major, J. Meersschaut, R. Rüffer, E. Szilágyi, J. Swerts, K. Temst, and A. Vantomme. Specular and off-specular synchrotron Mössbauer reflectometry: Applications to thin film magnetism. *Phys. Status Solidi A*, 189(2):591–598, 2002.

[82] M. Major, L. Bottyán, and D. L. Nagy. Simulation of domain formation and domain coarsening in antiferromagnetic multilayers. *J. Magn. Magn. Mater.*, 240:469–471, 2002.

[83] J. Unguris, R. J. Celotta, and D. T. Pierce. Observation of two different oscillation periods in the exchange coupling of Fe/Cr/Fe(100). *Phys. Rev. Lett.*, 67:140–143, 1991.

[84] M. Major, L. Bottyán, and D. L. Nagy. Simulation of unsaturation domain formation in antiferromagnetic multilayers. *Acta Physica Polonica A*, 101:301–305, 2002.

[85] M. Major, L. Bottyán, and D. L. Nagy. Simulation of antiferromagnetic domain formation history in magnetic multilayers. *Phys. Status Solidi A*, 189:995–999, 2002.

[86] D. R. Lee, S. K. Sinha, C. S. Nelson, J. C. Lang, C. T. Venkataraman, G. Srajer, and R. M. Osgood III. X-ray resonant magnetic scattering from structurally and magnetically rough interfaces in multilayered systems. ii. diffuse scattering. *Phys. Rev. B*, 68:224410, 2003.

[87] J. A. C. Bland, R. D. Bateson, N. F. Johnson, S. J. Blundell, V. S. Speriosu, S. Metin, B. A. Gurney, and J. Penfold. Magnetic coupling in Fe/Cr/Fe sandwich structures directly observed by polarised neutron reflection. *J. Magn. Magn. Mater.*, 123:320–324, 1993.

[88] A. Nefedov, J. Grabis, and H.Zabel. X-ray resonant magnetic scattering on noncollinearly coupled Fe/Cr superlattices. *Physica B*, 357:22–26, 2005.

[89] A. Nefedov, J. Grabis, A. Bergmann, F. Radu, and H. Zabel. X-ray resonant magnetic scattering by Fe/Cr superlattices. *Superlattices and Microstructures*, 37:99–106, 2005.

[90] S. K. Sinha, E. B. Sirota, S. Garoff, and H. B. Stanley. X-ray and neutron scattering from rough surfaces. *Phys. Rev. B*, 38:2297–2311, 1988.

[91] V. Holý and T. Baumbach. Nonspecular x-ray reflection from rough multilayers. *Phys. Rev. B*, 49(15):10668–10676, 1994.

[92] E. Chason and T. M. Mayer. Thin film and surface characterization by specular x-ray reflectivity. *Critical reviews in solid state and materials sciences*, 22(1):1–67, 1997.

[93] D. R. Lee, S. K. Sinha, D. Haskel, Y. Choi, J. C. Lang, S. A. Stepanov, and G. Srajer. X-ray resonant magnetic scattering from structurally and magnetically rough interfaces in multilayered systems. i. Specular reflectivity. *Phys. Rev. B*, 68:224409, 2003.

[94] D. G. Stearns. X-ray scattering from interfacial roughness in multilayer structures. *J. Appl. Phys.*, 71(9):4286–4298, 1992.

[95] E. E. Fullerton, J. Pearson, C. H. Showers, S. D. Bader, X. Z. Wu, and S. K. Sinha. Interfacial roughness of sputtered multilayers: Nb/Si. *Phys. Rev. B*, 48(23):17432–17444, 1993.

[96] M. Takeda, Y. Endoh, A. Kamijo, and J. Mizuki. Surface and interfacial magnetic diffuse scattering. *Physica B*, 248:14–24, 1998.

[97] J. A. Borchers, J. A. Dura, J. Unguris, D. Tulchinsky, M. H. Kelley, and C. F. Majkrzak. Observation of antiparallel magnetic order in weakly coupled Co/Cu multilayers. *Phys. Rev. Lett.*, 82(13):2796–2799, 1999.

[98] L. Deák, L. Bottyán, D. L. Nagy, H. Spiering, and Yu. N. Khaidukov. Perturbative theory of off-specular synchrotron Mössbauer reflectometry. *to be published*, 2006.